UNIVERSITÀ DEGLI STUDI DI CAGLIARI

Facoltà di Scienze Matematiche, Fisiche e Naturali

Corso di Laurea Specialistica in Fisica

Study of Low Mass Dimuon Production in 400 GeV Proton-Nucleus Collisions at the CERN-SPS with the NA60 Apparatus

Tesi di Laurea Specialistica

Relatore: Prof. Gianluca USAI
Correlatore: DI Dr. Hermine K. WÖHRI

Candidato: Antonio URAS

Anno Accademico 2006-2007

Nel ringraziare tutte le persone che mi hanno aiutato nella stesura di questa Tesi, rivolgo un pensiero speciale a Gianluca e Hermine, che mi hanno seguito in tutte le fasi del lavoro. Hermine, in particolare, è stata una guida infaticabile e premurosa, la cui costante disponibilità non è mai venuta meno in tutti questi mesi. I also would like to thank Ruben for always being available for discussion, almost in real time! Saluto con simpatia tutti i membri della collaborazione NA60 e tutto il Gruppo III della sezione di Cagliari dell'INFN. Ringrazio in particolare il Prof. Sergio Serci, che a suo tempo mi propose di «fare una tesi sul Quark Gluon Plasma», e Alessandro e Michele che mi hanno seguito nella preparazione della Tesi Triennale.

La discussione di questa Tesi Specialistica chiude anche un intero e intenso ciclo di studi. Vorrei allora cogliere l'occasione per salutare tutti coloro che mi sono stati vicini in questi anni: i colleghi dell'Università e in particolare i colleghi dei corsi di laboratorio; i colleghi del Conservatorio e i compagni del Liceo con i quali siamo riusciti a rimanere in contatto. Con affetto e riconoscenza, infine, saluto Giorgia e tutta la mia famiglia: senza di loro, sarei difficilmente arrivato fin qui.

Cagliari, 8 Dicembre 2007

Contents

1

Physics Motivation

The present work was performed within NA60, which is a fixed target experiment at the CERN SPS accelerator. NA60 studies proton-nucleus and nucleus-nucleus collisions in the dimuonic channel; data were taken between 2002 and 2004, and the analyses are currently still in progress. The current chapter gives a short overview of the physics topics explored within NA60, with emphasis on the topics related to this thesis.

Several experiments at the CERN SPS have measured lepton pair production in nuclear collisions over more than 15 years. The absence of significant reinteractions with the hadronic environment makes dileptons very attractive to study the early stages of the collision, when thermal dileptons from a deconfined phase are possibly emitted. Furthermore, the pseudoscalar and vector mesons produced in the collisions (η, ρ, ω, η', ϕ, J/ψ, χ_c, ...) can be detected in a clean way through their leptonic decay.

While a number of relevant results were obtained by the experiments which preceeded NA60, several points deserved a more detailed investigation. NA60 has been specifically designed with the idea to perform further high precision measurements on (i) the properties of the ρ meson in the strongly interacting dense medium created in a heavy ion collision, (ii) the unambiguous determination of the open charm yield and the quantitative assessment of the production of thermal radiation in the intermediate mass region (approximately between the ϕ and J/ψ resonances), and (iii) the study of the J/ψ suppression in a collision system other than Pb-Pb in an attempt to shed light on the mechanisms driving the suppression. These three issues are briefly summarised in the following paragraphs.

1.1 Main Results found by NA60 in In-In Collisions

Low Mass Region

The NA60 experiment has accumulated in the dimuon low mass region (below ~ 1.2 GeV/c^2) a statistics ~ 1000 times larger than the one collected by the experiment CERES having measured di-electrons. This allowed, for the first time, a very accurate study of the properties of the ρ meson in nuclear collisions. Two main models were developed in the 90s, predicting the behaviour of the ρ in the hot and dense matter produced in heavy-ion collisions. The first model directly links the mass of the ρ to the restoring of chiral symmetry, predicting a lowering of the mass pole by more than 100 MeV in the hot and dense medium [Bro91]. The second was a hadronic inspired model which predicted a strong broadening due to the coupling of the ρ to baryons and due to in-medium modifications of pions, but essentially no mass shift [Rap00]. The NA60 data clearly ruled out the scaling scenario [NA60].

Intermediate Mass Region

The dimuon mass spectrum between the ϕ and J/ψ resonances is dominated by Drell-Yan and simultaneous semi-leptonic decays of D mesons. The superposition of these two sources describes the measurements done in proton-nucleus collisions, while in nucleus-nucleus collisions the dimuon mass spectrum shows an excess which increases with the number of nucleons participating in the interaction [NA50]. Two interpretations of this excess have been considered: it can be due to an unexpected enhancement of open charm production or to thermal dimuons emitted from the deconfined phase. The NA60 In-In data clearly showed that open charm is not enhanced. The observed excess, whose yield is compatible with the NA50 measurement, is prompt in nature [Sha06]. Further analysis of the p_{T} spectra has shown that the excess could be the first direct evidence of thermal radiation produced by a partonic phase [NA60].

High Mass Region

The NA38 and NA50 experiments studied J/ψ suppression, as a signature of the formation of a deconfined state. In Pb-Pb collisions the J/ψ production pattern, as a function of the collision centrality, shows that above a certain centrality threshold the J/ψ yield is considerably lower than expected from the "nuclear absorption" curve, derived from proton-nucleus and light-ion collisions [NA50]. One of the current interpretations of this result is that the dense and hot medium formed in the collisions dissolves the χ_c resonance, leading to the disappearance of the fraction ($\sim 30\,\%$) of J/ψ mesons that would otherwise originate from χ_c decays. The NA60 data have shown that the J/ψ is suppressed also in In-In collisions with a pattern

compatible with the NA50 observations. Furthermore, the accuracy of the measurement allowed to falsify several models which were tuned on the NA50 Pb-Pb data [NA60].

1.2 Motivations and Expectations for the NA60 Proton-Nucleus Data

Besides In-In data, NA60 also collected a large data sample in proton-nucleus collisions. One important motivation is the need to establish a robust reference baseline for measurements in heavy ion collisions by studying systems where no new physics is expected. Several examples can be provided; before claiming that J/ψ suppression is linked to new physics, for instance, one should make sure that other conventional mechanisms, at work also in light systems, are accounted for.

Nevertheless, there is also an independent physics interest in in proton-nucleus collisions. In the low mass region, measurements performed in p-A interactions claimed that the properties of the ρ meson cold be modified also in "cold" nuclear matter [Oza01]. Other experiments found no evidence of such effects; it is hence important to accurately determine the line-shape in this environment. Another interesting effect involving the ρ meson is the ρ-ω interference, observed, for instance, in e^+e^- collisions [Lan85].

Another key study is the production of strangeness. In heavy ion collisions an enhancement of strangeness production was considered for long time a signature for the production of a deconfined state. For this reason, it is important to assess whether strangeness is enhanced already in proton-nucleus collisions.

This thesis reports on the data collected during three days within the 2004 proton run (amounting to $\sim 3.8 \times 10^6$ dimuon triggers), with a 400 GeV proton beam incident on several nuclear targets. From the physics point of view, the work was focused on the production of the ϕ meson, and, in particular, on its transverse momentum distribution.

The document is organized in the following way. After a description of the NA60 apparatus (Chapter 2), the run and burst selection will be considered (Chapter 3), followed by a detailed description of the event analysis (Chapter 4) which allowed us to get a "final sample" on which the physics studies could be based. After presenting a short description of the expected dimuon sources in the low mass region (Chapter 5) we will study the nuclear dependence of the p_{T} spectrum of the ϕ meson, combining the real data measured by the experiment with the results of the MC simulations.

2

The NA60 Apparatus

2.1 General Overview

The purpose of the NA60 apparatus is to accurately study dimuon production in proton-nucleus and heavy ion collisions. The produced dimuons are identified by the muon spectrometer, composed of a hadron absorber that lets only muons pass. The stopping of hadrons (provided by more than 20 interactions lengths) allows us to select the highly rare dimuon events. In this way, and by implementing a high selective trigger, we can run at very high luminosities (roughly speaking, only one out of 100 thousand collisions are recorded). On the other hand, the material which stops the hadrons also induces multiple scattering and energy loss on the muons, degrading the mass resolution of the measurement made in the spectrometer. To overcome this problem, NA60 already measures the muons *before* the absorber. This requires that the muon tracks are found among the many other charged particle tracks, by a correct matching with the reconstructed tracks in the muon spectrometer. For this reason, the angles and momenta of charged particles must be known in the vertex region with sufficient accuracy, requiring a magnetic field in the target region. The particle tracking in the vertex region is performed using a tracking telescope, made essentially of pixel and a few microstrip silicon detectors.

Figure 2.1 shows an overall representation of the NA60 apparatus. Note that the term "muon spectrometer" designates the detector system *after* the hadron absorber, including the trigger hodoscopes, while we speak of the "vertex tracking telescope" when we mean the tracking elements in the vertex region. In the following we will use the expressions "Jura" and "Salève" sides, referring to the left and the right sides of the experiment with respect to the central vertical plane, when seen from the beam line looking downstream.

The following sections describe the motivation, the design and performance of the detector components which are important for the analysis presented in this thesis. After a short overview of the beam, we will start with the muon spectrometer, the most important detector in this experiment. The subsequent sections then describe each detector in the sequence in which they are assembled along the beam direction.

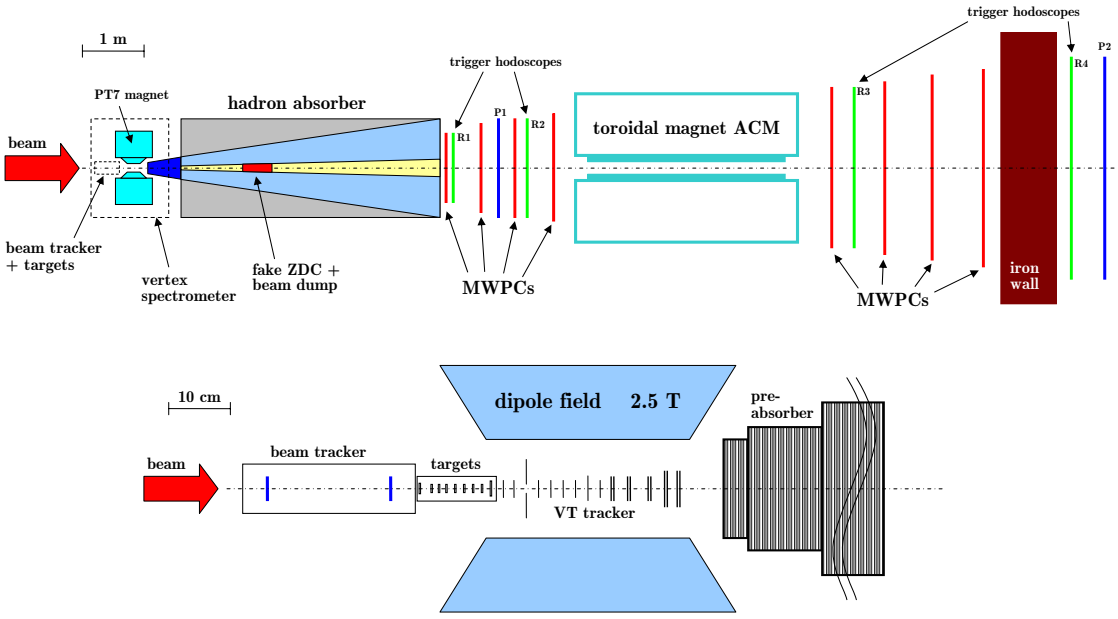

Figure 2.1: *Overall representation of the NA60 apparatus (top) and detail of the vertex region (bottom).*

2.2 The Beam

NA60 collected data with proton and ion beams provided by the CERN SPS accelerator. Ion beams were used in 2002 (test run with a Pb beam of 30 GeV per nucleon followed by 5 days with 20 GeV per nucleon) and in 2003 (In beam of 158 GeV per nucleon incident on In targets), while a 400 GeV proton beam was used both in 2002 (incident on Be, In and Pb targets) and − together with a 158 GeV proton beam − in 2004 (incident on Be, Al, Cu, In, W, Pb and U targets).

At the CERN SPS particles do not circulate in continuous mode, but rather they are delivered during well defined time intervals called "bursts", separated by "interburts". In the 2002 and 2004 proton runs, the bursts were $\sim$ 4.8 s long, separated by interburts lasting $\sim$ 12 s [Mem05]. The intensity of the proton beam was different in 2002 and 2004 proton runs: in the former the beam intensity was

$\simeq 2 \cdot 10^8$ protons per burst, while in the latter the beam intensity was approximately ten times higher, amounting to $\simeq 2 \cdot 10^9$ protons per burst, in order to gain as much statistics as possible to allow a study of the rare χ_c meson.

2.3 The Muon Spectrometer and Trigger System

The purpose of the muon spectrometer is to identify, trigger on, and reconstruct the muon pairs produced as a result of the beam-target interactions. In order to achieve this, it consists of four main elements [And84]: the hadron absorber, eight tracking multi-wire proportional chambers (MWPC), four trigger scintillator hodoscopes (R1-R4), the last one placed behind a 120 cm thick iron wall, and an Air Core toroidal Magnet (ACM) for the momentum measurement of the muons.

These components can be moved along the z-axis to ease maintenance and to keep the angular muon acceptance around mid-rapidity, in spite of changes in the beam energy. In the current setup, the angular muon acceptance lies approximately in the range 35–120 mrad (from 2° to 7°), as imposed by the magnet aperture. For beam energies of 400 GeV this corresponds roughly to one unit of rapidity at mid-rapidity, where particle production is most copious. The muon's acceptance also depends on the magnetic field settings and on the effective number of interaction lengths of the absorber; it is also affected by the trigger conditions.

2.3.1 The Hadron Absorber

The muons are filtered out among the many other produced particles by the hadron absorber. This is a simple, but effective, "particle identification" system: particles that hit the R4 trigger hodoscope (see Figure 2.1), by definition, are muons. Indeed, apart from neutrinos, only muons are penetrating enough to cross all the matter of which the absorber is made up:

- the pre-absorber, made of 41 cm BeO and 25.4 cm Al_2O_3
- the main absorber, made of 400 cm of graphite followed by 80 cm of iron[1]
- the 120 cm thick iron wall, placed after the muon chambers so as to not degrade the tracking accuracy through multiple scattering, while ensuring a very clean muon trigger

The hadron absorber starts as close as possible to the target region, immediately after the vertex telescope, in order to stop a large fraction of pions and kaons from decaying into muons and becoming a source of background.

[1] The composition of the main absorber sligthly changed during the 2004 proton run, see Chapter 3; here, we refer to the composition in the period of interest for this thesis.

The main absorber, placed between the target and the muon chambers, is made of materials with a low atomic number Z, in order to minimize the multiple scattering induced on the traversing muons, and with the highest available densities, so as to stop the hadrons in a relatively small thickness. The non-interacting protons are stopped in an "Uranium Plug", placed inside the absorber, aligned with the beam axis outside of the muon's acceptance window. The carbon blocks are surrounded by cast iron and concrete. Table 2.1 gives an overview of the position and thicknesses of the elements of the absorber for the data taking period relevant for this thesis (see Chapter 3).

Placing the last part of the absorber − the 120 cm thick iron wall − after the tracking stations and before the last trigger hodoscope, ensures that no energetic punch-through hadrons give rise to a fake trigger, without contributing to the degradation of the tracks measured in the chambers.

Material	ρ [g/cm^3]	z_{in} [cm]	Δz [cm]	λ_I [cm]	$\Delta z/\lambda_I$
BeO	2.81	43.6	41.0	35.85	1.14
Al_2O_3	3.52	84.6	25.4	32.65	0.78
C	1.93	110.0	400.0	44.70	8.95
Fe	7.87	510.0	80.0	16.76	4.77
Total number of interaction lengths in main absorber					15.64
Fe (iron wall)	7.87	1676.3	120.0	16.76	7.16
Total number of interaction lengths					22.8

Table 2.1: *Composition of the hadron absorber for the data taking period relevant for this thesis (see Chapter 3) during the 2004 proton run. λ_I is the nuclear interaction length.*

2.3.2 The Multi-Wire Proportional Chambers

The muons which have crossed the main absorber are tracked in eight multi-wire proportional chambers, separated into two sets of 4 chambers by the toroidal magnet ACM (Air Core Magnet).

Each muon chamber consists of three independent tracking planes, interspaced by 2.2 cm, rotated by 60° with respect to each other, to allow a good measurement of one space point (see Figure 2.2).

The sensing elements of these chambers are gold-plated tungsten anode wires with a diameter of $\sim$ 20 μm, inter-spaced by 3 mm and sandwiched between two graphited Mylar cathode planes, 6 mm far away. The overall read-out gate is $\sim$ 80 ns

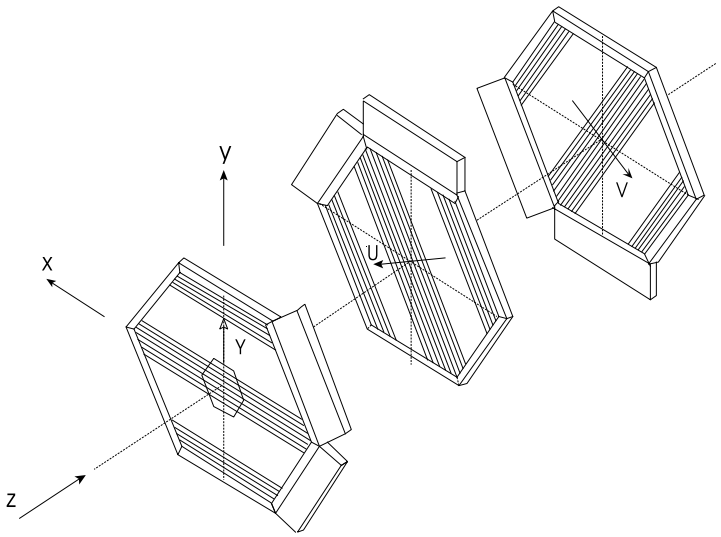

Figure 2.2: *Each MWPC consists of three independent tracking planes. For visibility purposes the individual planes are shown well separated from one another.*

[And84]. The chambers have hexagonal shape and their transverse size increases with increasing distance from the target to cover the angular acceptance, defined by the aperture of the ACM magnet. The z-positions with respect to the target and the transverse size of all components of the muon spectrometer can be found in Table 2.2.

The tracking volume of the chambers is filled with a gas mixture, consisting of $\sim$ 80 % of Argon (of which 50 % is flushed through 0.8% of Isopropyl alcohol), of 18 % Isobutane iC_4H_{10} used as a quencher, and of 2 % Tetrafluorethane used as a "cleaning" gas. A gas mixer rack measures and controls the flow of the gas components. Due to the fact that the gas mixture had to be changed in 2002 with respect to the previously used "magic gas", the chambers showed visible "ageing effects"; in particular, 5 planes out of 24 were not working during the data taking period relevant to this thesis [Mem05], see Chapter 3: the track reconstruction could still be performed using the remaining working planes, with a sligthly degraded efficiency. It is worth noting that − apart from chamber 1, which was completely rebuilt in 1994 − all MWPCs work since 1980, when NA10 (the predecessor experiment of NA38, NA50 and NA60) began to operate.

2.3.3 The Trigger Hodoscopes

The trigger system consists of four "R" hodoscopes, two before and two after the ACM magnet, made of scintillator slabs. Like all other components of the muon spectrometer, the hodoscopes have hexagonal shape, given by the geometry of the

ACM magnet. All R-hodoscopes are designed in a similar way. The scintillator slabs of each sextant, oriented parallel to the outer edges, become longer with increasing distance from the beam axis (see Figure 2.3).

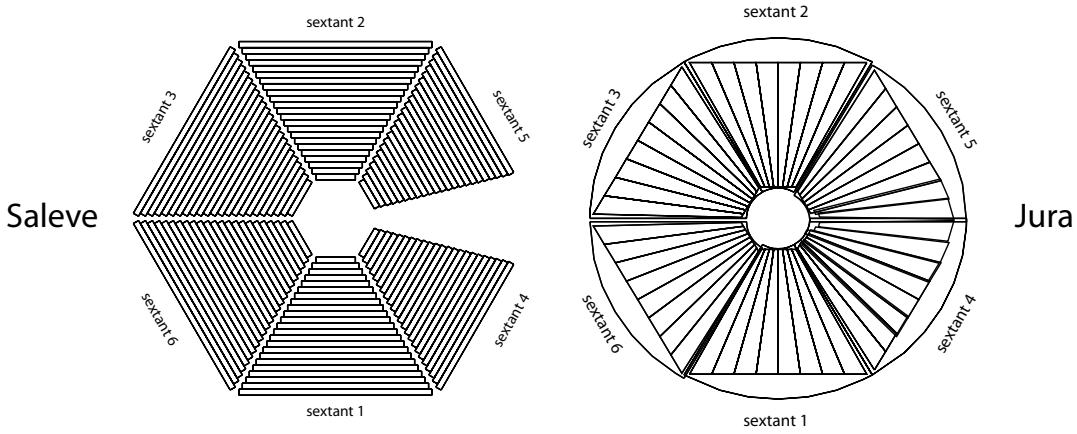

Figure 2.3: *The segmented slabs of the R3 (left) and P (right) hodoscopes.*

The width of the slabs of the R1 and R2 hodoscopes increases with the distance from the beam line so that a muon produced in the target which passes through slab i in R1 will also hit slab i in R2. In order to accomodate the longitudinal spatial extent of the target region (of the order of ~ 1 m in the NA10 experiment, which designated the trigger logic) and to allow for multiple scattering for low energetic muons, the combination of hitting slab i in R1 and $i-1$ in R2 is also allowed. This "R1-R2 coincidence" for each muon is combined with the information from R3 and R4. The last trigger hodoscope, R4, is placed behind the 120 cm thick iron wall, which absorbs remaining hadrons thereby ensuring a clean (di)muon trigger; however, this implies that the muons must have a minimal momentum of ~ 7 GeV/c to give a signal in R4. The dimuon trigger also requires that the two muons pass through two different sextants: this requirement reduces the fraction of low mass muon pairs that give rise to a trigger, in order to not saturate the bandwidth of the data acquisition system. The overall read-out gate of the R-hodoscopes is 20 ns.

The R3 hodoscope has a small inactive zone on the "Jura" side, called "Beam-Killer", as can be seen in Figure 2.3. Although the other trigger hodoscopes have no such dead areas, the muon acceptance is affected by this cut in sextants 4 and 5, since the trigger requires a hit in *all* trigger stations.

The P-hodoscopes

Furthermore, NA60 uses two so-called "P-hodoscopes", P1 and P2. The former is placed before the ACM magnet, the latter after the iron wall. They are used in special runs to measure the efficiency of the R1-R4 system. Their geometry is different from the R-hodoscopes; the scintillator slabs of each sextant are oriented

radially, so that their width increases with increasing distance from the beam axis (see Figure 2.3).

In the 2004 proton run an additional feature was implemented: the measure of the arrival time of each muon at the P2 hodoscope; this (see Chapter 4) improves our ability of rejecting trigger coincidences of 2 muons that were produced in *different* events. This possibility improves significantly our event selection, needed because of the very high luminosities.

Element	z [cm]	**Main Characteristics**
MWPC 1	615.8	448 wires per plane, $\varnothing = 134$ cm
Hod. R1	629.6	6×30 scintillator slabs of 1.05–3.45 cm width
MWPC 2	684.1	512 wires per plane, $\varnothing = 153$ cm
Hod. P1	712.0	6×8 scintillator elements; width: 2.73–13.65 cm
MWPC 3	748.7	576 wires per plane, $\varnothing = 172$ cm
Hod. R2	761.0	6×30 scintillator slabs of 1.25–3.35 cm width
MWPC 4	818.2	640 wires per plane, $\varnothing = 192$ cm
ACM	828.7 – 1311.7	
MWPC 5	1347.2	1024 wires per plane, $\varnothing = 306$ cm
Hod. R3	1390.2	6×23 scintillator slabs of 5.5 cm width
MWPC 6	1445.6	1088 wires per plane, $\varnothing = 326$ cm
MWPC 7	1544.1	1152 wires per plane, $\varnothing = 345$ cm
MWPC 8	1642.1	1216 wires per plane, $\varnothing = 364$ cm
Iron wall	1676.3 – 1796.3	
Hod. R4	1800.7	6×32 scintillator slabs of 5.5 cm width
Hod. P2	1820.7	6×8 scintillator elements; width: 8.10–47.50 cm

Table 2.2: *Detector components of the muon spectrometer. Except for the ACM and iron wall, the z values given refer to the centre of the respective device.*

2.3.4 The Toroidal Magnet ACM

The magnetic field of the toroidal magnet ACM is produced between 6 radial iron poles, which are 4 m long and cover 18° in azimuth. The magnet's air gap starts at a radius of 29.5 cm, while the outer radius is 154 cm. These two values are the ones determining the detector's rapidity acceptance. Events with muons which cross one

of the iron pieces are rejected from the physics analysis, since they have degraded momentum resolution, compared to the ones which traverse the air core between them. The toroidal magnetic field is $1/r$ dependent, according to the relation:

$$\vec{B}(r) = B_0/r \cdot \vec{e}_\phi \ .$$

In Figure 2.4 we can see the magnitude of the magnetic field in the air sectors for different distances from the beam-axis. The proportionality constant between the magnitude of the magnetic field and the radius is $B_0 = 0.219$ T·m for a current of 4000 A, as used for the data taking period relevant for this thesis. The ACM current is pulsed, synchronised with the SPS cycle, and is recorded burst by burst.

The bending power depends on the radial distance from the beam. Since the axis of the magnet is aligned along the beam axis, the muons keep their azimuthal angle while changing their polar angle. The ACM magnet was designed such that the deflection angle, $\Delta\theta$, is inversely proportional to the particle's p_T, as explained in [Lou95].

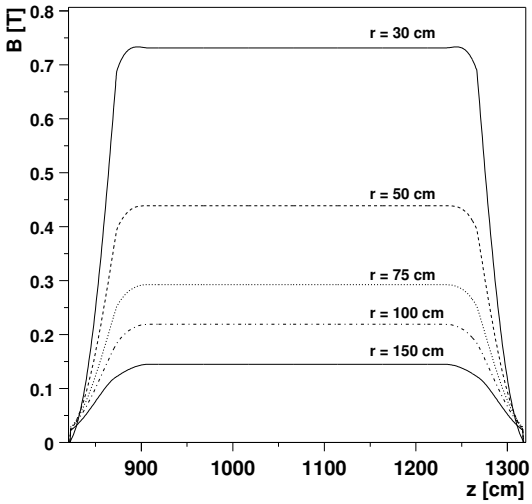

Figure 2.4: *Magnitude of the toroidal field for various distances from the beam axis.*

2.4 The Target System

The NA60 experiment used different target systems in proton and ion runs. In ion runs, in order to have a symmetric collision system, indium targets were used with the indium beam, and lead targets with the lead beam.

In the proton runs, one of the physics topics of interest is the study of the nuclear dependence of the production cross-section of various particles, hence different target materials were used. In the 2002 proton run, targets of beryllium, indium and lead were used; in 2004 aluminium, copper, tungsten and uranium targets were used additionally.

Placing these different targets simultaneously into the beam allows to minimise systematic errors coming from luminosity calculations, which will affect all the targets in the same way. In order to distinguish the particular sub-target from which the muons originate, the various sub-targets are well separated along the beamline.

The target system used in the 2004 proton run, composed of 9 disk-shaped sub-targets, is represented in Figure 2.5. The position, thickness and diameter for each sub-target are reported in Table 2.3. The need of forcing the conversion $\gamma \to e^+e^-$ in the study of the process $\chi_c \to J/\psi + \gamma$ justifies the use of a Pb target having an exceptionally large diameter, 2 cm, placed downstream of all other targets, such that a sizeble fraction of the photons produced in the upstream targets (as well as those produced in the Pb target itself) are converted into electron-positron pairs when going through the disk, which can be tracked in the vertex telescope.

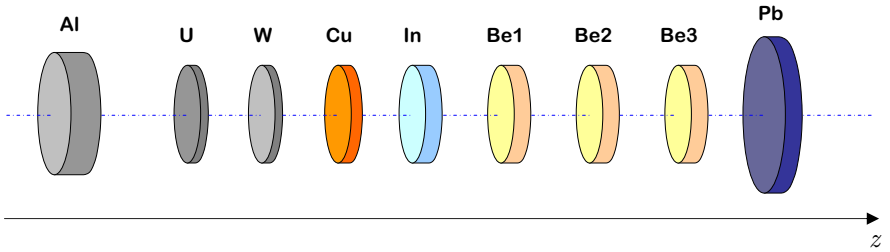

Figure 2.5: *Target system used in the 2004 proton run.*

Tgt. ID	Material	A	z [cm]	Δz [cm]	$\varnothing$ [cm]	λ_I [cm]	$\Delta z/\lambda_I$
0 (Al)	Aluminium	27	−8.15	0.40	1.5	39.4	0.0101
1 (U)	Uranium	238	−6.65	0.10	1.2	10.5	0.0095
2 (W)	Tungsten	184	−5.85	0.10	1.2	9.59	0.0104
3 (Cu)	Copper	64	−5.05	0.15	1.2	15.1	0.0100
4 (In)	Indium	115	−4.25	0.20	1.2	23.0	0.0087
5 (Be1)	Beryllium	9	−3.25	0.20	1.2	40.7	0.0049
6 (Be2)	Beryllium	9	−2.25	0.20	1.2	40.7	0.0049
7 (Be3)	Beryllium	9	−1.25	0.20	1.2	40.7	0.0049
8 (Pb)	Lead	208	−0.25	0.20	2.0	17.1	0.0117
					Total number of interaction lengths		0.0751

Table 2.3: *Sub-targets forming the target system in 2004 proton run. The z values given refer to the centre of the respective target.*

2.5 The PT7 Dipole Magnet

To measure the particles' momenta in the vertex region, the silicon tracking telescope is placed in the gap of a dipole magnet, called PT7. Its dimensions can be seen in Figure 2.6. When operated at 900 A, close to its maximum value, the PT7 magnet allows to obtain a magnetic field of 2.5 T.

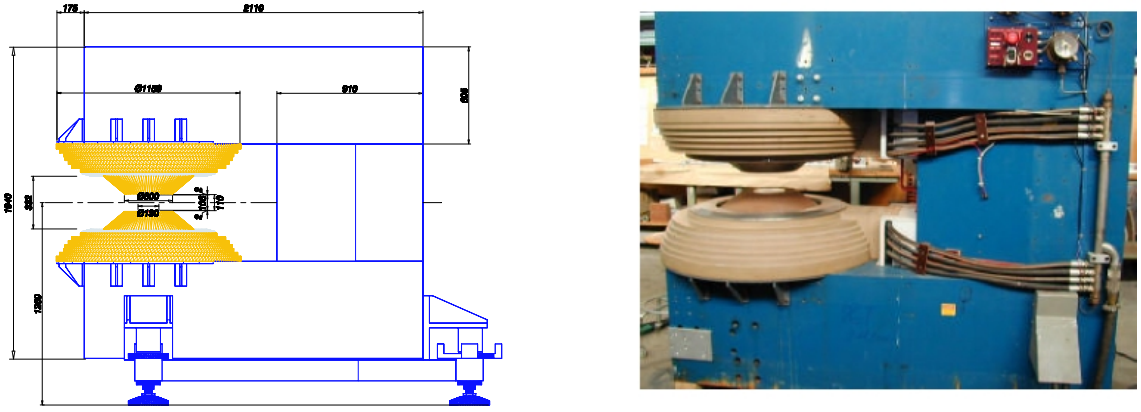

Figure 2.6: *Front view of the PT7 magnet, as seen from the incoming beam.*

Special care was taken in the design of the surface of the pole shoes, by means of specially designed "shims", to ensure that the magnetic field is highly homogeneous. Figure 2.7 shows the magnitude of the magnetic field in the $x-z$ plane, measured at the centre of the vertical gap: the rotational symmetry around the y axis is clearly visible, together with the plateau of the field in the centre of the magnet.

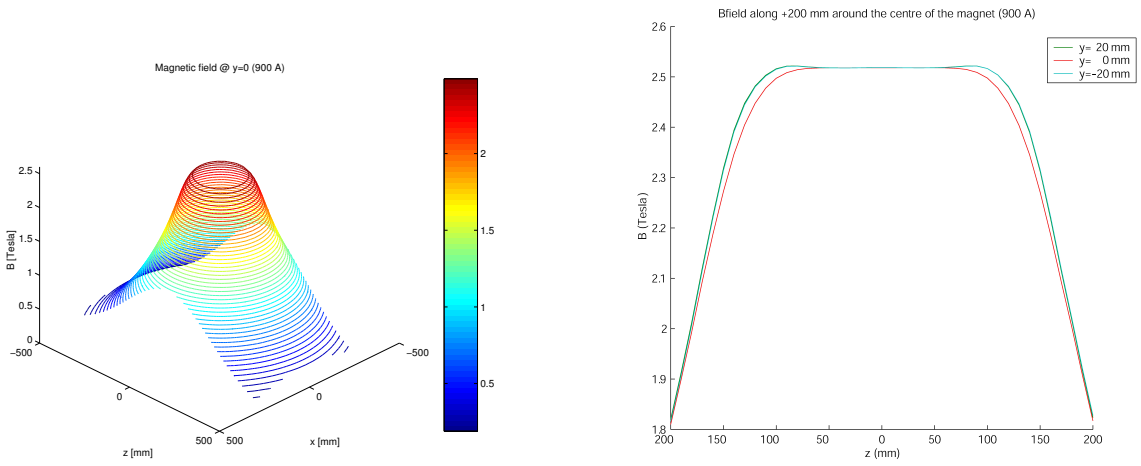

Figure 2.7: *PT7 magnetic field measured in the centre of the gap, with a current of 900 A.*

The magnetic field was carefully measured with a Hall probe in steps of 1 cm in each of the three axes. These measurements were parameterised and inserted into the NA60 detector simulation package, NA60root. Due to the dipole symmetry, it suffices to consider two components: the vertical component B_y and the radial component B_r in the $x - z$ plane. A simple bilinear interpolation of the measured values was used to describe the field.

To reduce systematic uncertainties, the polarity of the magnet is reversed every few runs. During the field mapping, it was verified that reversing the polarity leads to deviations of the magnetic field, if any, of smaller than 0.2 %.

2.6 The Vertex Tracking Telescope

The purpose of the vertex tracking telescope is to track the secondary particles, including muons, produced as a result of an interaction in the target, before they enter in the hadron absorber. Out of the many uninteresting particles, the muons have to be unambiguously identified by matching with the tracks reconstructed in the spectrometer.

Apart from improving the mass resolution of the reconstructed dimuons, the tracking telescope in the vertex region allows us to "identify" the sub-target where the interaction took place, by finding the common origin of the reconstructed tracks.

NA60 uses both silicon microstrip and silicon pixel technology for the tracking elements in the target region. In the 2002 proton run, the low charged particle multiplicities allowed the use of microstrip detectors, while the much higher particle densities reached in heavy ion collisions imposed in 2003 the exclusive use of silicon pixel detectors. The microstrip and pixel planes were designed to fit in the gap of the PT7 magnet and to match the muon spectrometer's angular acceptance.

Unlike in 2002, in 2004 the vertex telescope (VT) was composed mainly of silicon pixel planes. The reason is due to the intensity of the proton beam used in 2004, which was chosen to be 10 times higher than the intensity in 2002: the increased intensity involves an increase of the occupancy in the vertex telescope, and demands the use of pixel sensors having a higher granularity than the microstrips. Furthermore, the analysis conducted on the 2002 and 2003 data has shown [Wöh04, Kei05] that pixel chips offer a sligthly higher efficiency than the microstrip sensors. The use of *analog* microstrips, however, allows to have a much higher time resolution, of the order of 5 ns to be compared with the 2×100 ns and 2×25 ns read-out windows of the ALICE and ATLAS pixels, see below. For this reason, even in the 2004 high-intensity proton run the vertex telescope contained 4 microstrip sensors placed at the very end, where smaller granularity is needed.

The Setup

As will be outlined in the next chapter, the p-A data collected during the 2004 run consist of six parts, all relative to the same system of Be, Al, Cu, In, W, Pb and U sub-targets. The data taking conditions for these six periods differ from each other due to the following changes in experimental setup:

- the energy of the proton beam
- the composition of the first two tracking stations of the vertex telescope
- the thickness of the iron block sitting at the end of the main absorber, just before the multi-wire proportional chambers

As the present work is devoted to the analysis of p-A data collected during the fifth period (400 GeV proton beam, runs 11580–11804), we will only describe the corresponding setup of the vertex telescope; this setup is represented in Figure 2.8, from which 14 tracking stations can be distinguished:

- 7 stations composed of 1 small ALICE pixel plane (small ALICE stations)
- 2 stations composed of 2 ATLAS pixel planes (ATLAS stations)
- 3 stations composed of 2 large ALICE pixel planes (large ALICE stations)
- 2 stations composed of 2 BNL microstrips planes (BNL stations)

Each type of station is described in the following. The setup of the tracking stations forming the vertex telescope is summarized in Table 2.4.

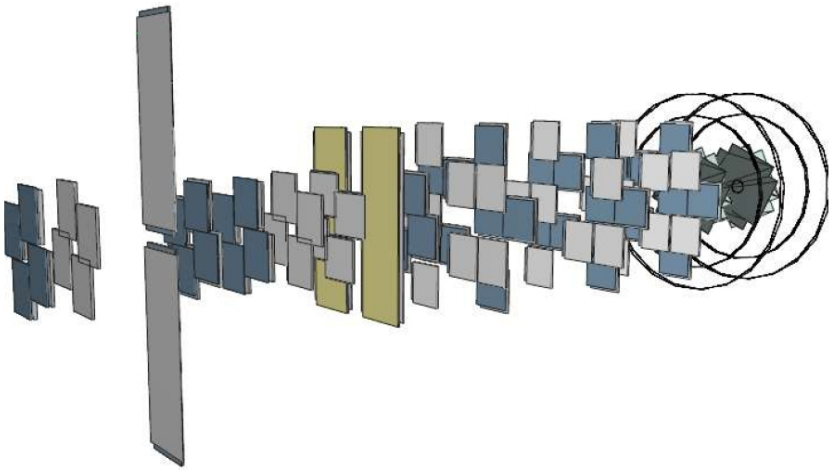

Figure 2.8: *Vertex telescope used in the run period relevant to this thesis (runs 11580–11804), see Chapter 3.*

The vertex telescope was cooled by means of a closed-circuit system with a fluorcarbon (C_6F_{14}) coolant circulating in the detector planes' cooling pipes, in order to reduce radiation damage and minimise leackage current of the silicon detectors. A custom-built, high performance refrigerator cooled and pumped the fluorcarbon through the circuit; temperatures as low as $-10°$ C were measured on the hybrids supporting the pixel chips, with no appreciable fluctuations. To avoid condensation, the whole vertex telescope was enclosed in a proctective bag, permanently flushed with nitrogen, tailored *in situ* to fit the tight and convoluted geometry of the vertex region.

The ALICE Pixel Planes

The small ALICE tracking planes, forming the small tracking stations, consist of 4 rectangular chips placed around a beam hole. Because of their small transverse dimensions they are used only in the first section of the vertex telescope, closer to the target region, where they still cover the muon spectrometer geometrical acceptance. The large tracking stations are composed of two large ALICE planes, each made of 8 chips. To improve the muon acceptance coverage, a small pixel plane is placed close to the first large station, to cover its beam hole; as will be discussed in Chapter 3, during the data taking period relavant to this thesis, this plane never provided any signal, although physically having been present and, hence, contributing to multiple scattering and energy loss to the particles traversing it.

Both small and large tracking planes use the same type of chip. Each chip has 8 192 pixels with an area of 425×50 μm^2, arranged in a matrix of 32 columns and 256 rows, giving a total active area of 13.6×12.8 mm^2. Within a given plane, all chips are mounted with the same orientation, defining the plane as X or Y, depending on the orientation of the 50 μm side. To cover the full angular acceptance, some planes are inverted upside-down, having their back side facing the beam [Ban04].

A pixel chip assembly is a 750 μm thick ALICE1LHCB pixel read-out chip [Wyl99] bump-bonded to the 300 μm pixel sensor chip. These chips operate at a frequency of 10 MHz; however, since the dimuon trigger is asynchronous with respect to the chip's clock (i.e. the dimuon trigger can come at any moment with respect to the clock), we must record two clock cycles whenever there is a trigger, to ensure fully efficient tracking. Hence, the total read-out gate is 2×100 ns.

Such pixel chip assemblies are glued on BeO or Al_2O_3 hybrids, which are placed on printed circuit boards (PCBs) to route the electrical lines out of the magnet's gap. A zoomed view of a 4-chip plane and a fully assembled 8-chip plane can be seen in Figure 2.9. The PCBs are mounted on aluminium frames for mechanical support, and placed in the slots of a support box that slides in the magnet gap.

It is worth noting that most of these planes were already used in the 5-weeks long 2003 run, where they accumulated considerable radiation doses from being exposed to the secondary particles produced in the indium-indium collisions. It has been estimated that, by the end of that run, the innermost detector regions, closest to

the beam axis, integrated a radiation dose equivalent to a total fluence of more than 10^{13} 1 MeV neutrons per cm^2 [BHK04] (an order of magnitude higher than the doses these pixels are expected to accumulate after 10 years of operation in the ALICE experiment at the LHC). At the end of 2003, the most exposed planes reached depletion voltages of 150 V compared to the 40 V needed before type inversion. In order to use these planes again in the 2004 run, expected to provide a total fluence at least as high as that of 2003, it was clearly crucial to operate them at low temperatures, to decrease their leakage current and their needed depletion voltage. This implied the development of a new cooling system, a highly non-trivial operation [Mem05].

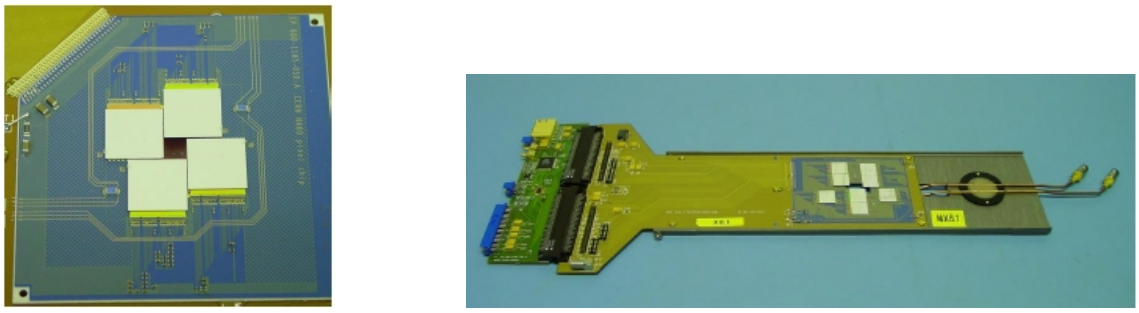

Figure 2.9: *Zoomed view of a 4-chip plane, showing the sensor and read-out chips mounted on the ceramic hybrid (left) and a fully assembled 8-chip plane (right).*

The ATLAS Pixel Planes

The four ATLAS pixel sensors [Ala01] were arranged in two physical tracking planes to maximise their angular acceptance. The downstream plane is shown in Figure 2.10.

From a technical point of view, each ATLAS pixel module contains a single sensor chip with an active area of 16.4×60.8 mm^2, connected to 16 read-out chips. The sensor area is divided into 328×144 pixels with a size of 50×400 μm^2 (16 of 144 colums are 600 μm wide to bridge the gap between neighboring front-end chips). The modules were glued on a 500 μm thick carbon fiber plate and mounted on a support frame similar to those of the ALICE pixel planes.

The ATLAS pixel read-out chips operate at 40 MHz. The 2-clock-cycle window, giving a total read-out gate of 2×25 ns, is imposed by the asynchronous trigger, as was already discussed for the ALICE pixel planes. It is worth to note that the total read-out gate of the ATLAS pixel planes is four time smaller than the read-out gate of the ALICE pixel planes: the existence of the ATLAS tracking planes effectively plays a crucial role, because it allowed the experiment to run at four times higher beam intensities than with only ALICE pixel planes; thus, we could

collect more statistics for the same amount of beam time. In particular, taking into account the ATLAS pixel read-out and assuming a Poissonian distributed arrival of beam protons, it can be shown [Lou07] that only at beam intensities around $2 \cdot 10^9$ protons per 4.8 s burst we reach the limit of two pile-up collisions on top of the one which gave the trigger, given the $\sim 10\,\%$ λ_{int} thickness of the target system; at such collision rate, the ALICE pixel detector integrate, on average, tracks from 9 different proton-nucleus collisions in their 2×100 ns read-out window (a detailed calculation of the expected pile-up in 2004 proton run is presented in Chapter 4). During the data reconstruction we, hence, must require that a track leaves a hit in the ATLAS pixel planes, in order to reject tracks produced in pile-up interactions outside of the ATLAS planes' 2×25 ns read-out gate; on the other hand, this effectively limits the vertex telescope's geometrical acceptance to the one given by the ATLAS pixel planes.

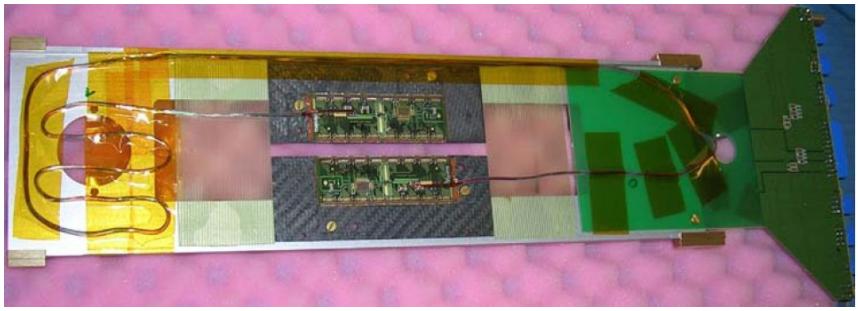

Figure 2.10: *The downstream ATLAS pixel plane. The two modules, mounted on a carbon fiber plate, are visible at the centre of the picture, above and below a gap left free to let the non-interacting beam pass through.*

The BNL Microstrip Sensors

The BNL microstrip detector planes were already successfully operated during the 2002 proton run [Wöh04]. Each sensor provides the positions of the hits in one dimension. In order to obtain one space points, each microstrip tracking station consists of two microstrip sensor planes assembled back to back, which have an inclination angle of $\pm\,25°$ with respect to the vertical axis y. This inclination optimizes the particle tracking in the magnetic field of the PT7, oriented in the y direction.

The BNL microstrip planes are built from 4-inch silicon sensors, with 12×128 strips arranged such as to keep the occupancy below $3\,\%$ for p-Pb collisions in case of single interactions without pile-up. The BNL sensors were designed with the strips arranged in two regions, the inner one, surrounding the beam hole, and the outer one, of longer strips and only used for the planes placed far from the target. The inner region is sufficient to cover the angular acceptance of the muon spectrometer

in the planes closer to the target and, in fact, only the strips in that region, for those planes, were used in the track reconstruction of the 2002 data. Contrary to the other silicon detectors used in the 2004 proton run, the BNL microstrip planes do not have any inactive area − apart from the beam hole.

The transverse dimensions of the active area of the BNL microstrip sensors still cover the angular acceptance at ~ 40 cm from the target, allowing to profit the full range of the magnetic field over which it is roughly constant. In this way we can increase the vertex telescope's lever arm for momentum determination. Furthermore, at these large distances from the target the coarser granularity of the sensors' outer region is highly sufficient for particle tracking.

The BNL microstrip detectors are sampled at 40 MHz (i.e. every 25 ns) and four analog samples are read out when a trigger arrives. With respect to 2002, a new feature was added at the the read-out level, namely a TDC, leading to an improved timing accuracy of $\lesssim 5$ ns if correctly calibrated. Although the BNL microstrip sensors have an efficiency lower than the one of the pixels (95 % versus 90 % on average) they should further help to improve the validation of "in time" tracks, i.e. those tracks which are produced "in time" with the collision that gave rise to the trigger.

Station ID	**Sensing elements**	***z* Pos.** [cm]	**Read-out gate**
0	4 ALICE pixel chips	5.68	2×100 ns
1	4 ALICE pixel chips	6.91	2×100 ns
2	2 ATLAS pixel chips	9.37	2×25 ns
3	4 ALICE pixel chips	10.60	2×100 ns
4	4 ALICE pixel chips	12.22	2×100 ns
5	4 ALICE pixel chips	13.90	2×100 ns
6	4 ALICE pixel chips	15.47	2×100 ns
7	2 ATLAS pixel chips	16.73	2×25 ns
8	4 ALICE pixel chips	18.76	2×100 ns
9	8 + 8 ALICE pixel chips	20.39 ; 22.01	2×100 ns
10	8 + 8 ALICE pixel chips	22.67 ; 28.28	2×100 ns
11	8 + 8 ALICE pixel chips	31.75 ; 33.28	2×100 ns
12	2 BNL microstrip sensors	35.92 ; 36.09	4×25 ns
13	2 BNL microstrip sensors	39.92 ; 40.09	4×25 ns

Table 2.4: *Tracking stations forming the vertex telescope used in the run period relevant to this thesis (runs 11580–11804), see Chapter 3.*

3

Data Reconstruction and Selection

3.1 Overview of the Six Data Taking Sub-Periods

As mentioned in the previous Chapter, the p-A data collected during the 2004 proton run consist of six sub-periods. The data taking conditions for these sub-periods differ from each other due to the following changes in experimental setup:

- the energy of the proton beam
- the composition of the first two tracking stations of the vertex telescope
- the thickness of the iron block at the end of the main absorber, just before the multi-wire proportional chambers

The data are collected in several independent "runs", each taken under the same experimental conditions; each run contains several bursts, and each burst consists of several triggers.

In the following we will give an overview of the characteristics of the data taking sub-periods, summarising them in Table 3.1. In the next section we will instead focus on sub-period 5, on which this work is based. Most of the other sub-periods are not yet reconstructed and, hence, not yet available for physics data analysis; their description only serves for reference purposes, and may be peacefully skipped if not specifically interested to it.

The First Sub-Period: Runs 10015–10116

The first sub-period useful for data analysis lasted from 2004/09/17 to 2004/09/20, giving 102 runs, corresponding to $\sim 4\,600$ bursts and $\sim 6.3 \times 10^6$ triggers.

In this sub-period a 400 GeV proton beam was used. The corresponding setup of the vertex telescope is shown in Figure 3.1; the first two tracking stations were composed of an ATLAS and a BNL microstrip station, respectively. The iron block at the end of the main absorber was 40 cm thick.

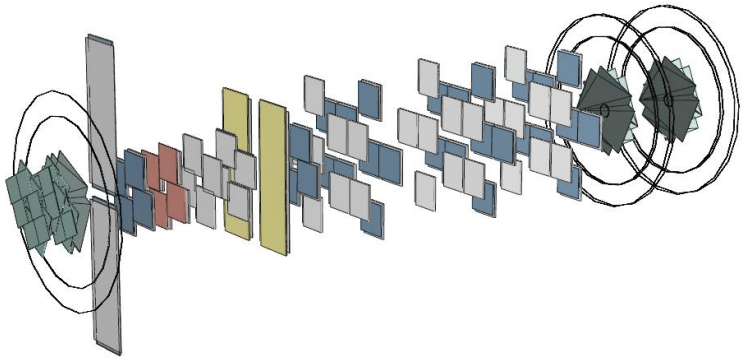

Figure 3.1: *Setup of the vertex telescope used in the first sub-period (runs 10015–10116).*

The Second and Third Sub-Periods: Runs 10117–10361 and Runs 10380–11187

The second sub-period lasted from 2004/09/20 to 2004/09/24, giving 245 runs corresponding to $\sim$ 9 900 bursts and $\sim 5.2 \times 10^6$ triggers. Also in this sub-period a 400 GeV proton beam was used. The corresponding setup of the vertex telescope is shown in Figure 3.2; the first two tracking stations were composed of an ATLAS microstrip station and a small ALICE pixel station, respectively. The iron block at the end of the main absorber was still 40 cm thick, as in the first sub-period.

The third sub-period lasted from 2004/09/24 to 2004/10/13, giving 808 runs corresponding to $\sim$ 30 700 bursts and $\sim 24.7 \times 10^6$ triggers. This sub-period shares with the second one the setup of the vertex telescope, as well as the beam energy; the only difference is the thickness of the iron block at the end of the main absorber, which on the 24$^{\text{th}}$ of September was increased from 40 to 80 cm, in order to reduce the occupancy in the muon spectrometer. The thickness of the iron block was not further changed in the subsequent data taking sub-periods. This increased absorber thickness was needed because of another wire broken in one of the planes of a MWPC placed between the absorber and the ACM magnet (the section in the muon spectrometer where the occupancies are higher), which forced to switch off the plane for further data taking. During the same sub-period, another plane stopped working in a MWPC placed *after* the ACM magnet, but this accident did not involve any change in the setup of the apparatus. No further planes had problems in the rest of the run, but it is worth mentioning that three planes were already switched off at the beginning of the first sub-period. We, thus, had three dead planes out of 24

in sub-periods 1–2; four and then five in the sub-period 3; five in sub-periods 4–6 [Mem05].

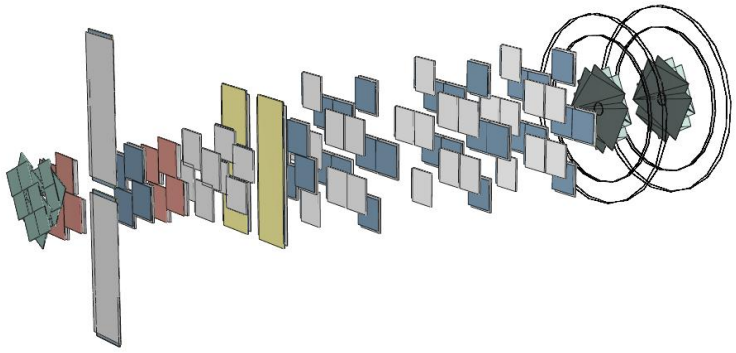

Figure 3.2: *Setup of the vertex telescope used in the second (runs 10117–10361) and the third (runs 10380–11187) sub-periods.*

The Fourth and Fifth Sub-Periods: Runs 11234–11559 and Runs 11580–11804

The fourth sub-period lasted from 2004/10/13 to 2004/10/18, giving 326 runs corresponding to $\sim$ 14 000 bursts and $\sim 11.3 \times 10^6$ triggers. This sub-period is the only one in which a 158 GeV proton beam was used, in order to extract the normal nuclear absorption cross-section of the J/ψ at 158 GeV; this allows a *direct* comparison with the heavy-ion data (Pb-Pb and In-In) collected at 158 GeV per nucleon without a rescaling to the lower energy. The setup of the vertex telescope used in this sub-period was also used in data taking sub-period number 5, the one of interest for this thesis. It was described in detail in Chapter 2, see Table 2.4. From Figure 2.8 we see that the first two tracking stations were now both composed by small ALICE pixel stations.

The fifth sub-period lasted from 2004/10/19 to 2004/10/21; the only difference with respect to sub-period 4 is the use of a 400 GeV proton beam. Since it is the only sub-period of interest to the present work, its run and burst selection will be extensively discussed in the following sections; the corresponding statistics is based on 225 runs, corresponding to $\sim$ 10 600 bursts and $\sim 12.9 \times 10^6$ triggers, representing $\sim 1/10$ of the full statistics collected at 400 GeV.

It is due to the fact that the ATLAS microstrip sensors were not used, that these two sub-periods are the only ones whose data are already reconstructed.

The Sixth Sub-Period: Runs 11805–12888

The sixth sub-period lasted from 2004/10/22 to 2004/11/15, giving 1084 runs, corresponding to $\sim$ 55 600 bursts and $\sim 49.0 \times 10^6$ triggers. This sub-period represents

the largest statistics, but its data are not yet reconstructed.

The vertex telescope setup used in the sixth sub-period is the one originally foreseen for the whole 2004 proton run, and is shown in Figure 3.3. In this setup the first two tracking stations are both composed of ATLAS microstrip modules, choosen because they are more adapted in detecting the e^+e^- tracks, resulting from the conversion of the photon produced in the process $\chi_c \rightarrow J/\psi+\gamma$, whose study was intended to be one of the main topics of the 2004 proton run; their material budget, much smaller than that of the ALICE pixel modules, induces as little multiple scattering as possible when the electrons traverse the first tracking stations.

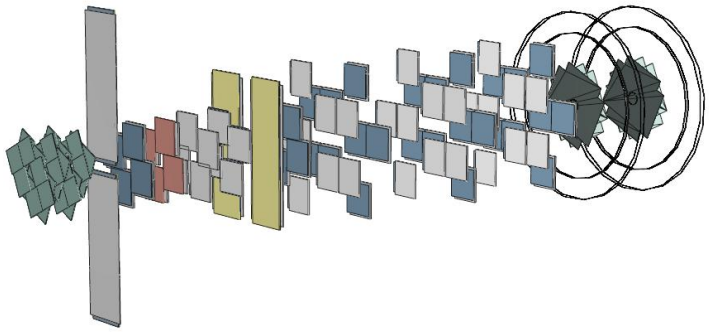

Figure 3.3: *Setup of the vertex telescope used in the last (sixth) sub-period (runs 11805–12888).*

3.2 Data Reconstruction for the Runs 11580–11804

The data reconstruction procedure begins by decoding the recorded raw data (analog or digital detector signals) into a hit map of the individual sub-detector elements (strip planes, trigger hodoscopes, multi-wire proportional chambers, ...). The data reconstruction of the digitised and clusterised data is then performed in several steps. Since the number of tracks after the hadron absorber is significantly smaller than in the vertex region, the tracks in the muon spectrometer are reconstructed first. Only if at least two muons were found, whose origin is in the target region, the track reconstruction in the vertex telescope is performed.

If at least two tracks in the vertex telescope were found, the event reconstruction proceeds via fitting the vertices of the found tracks. The matching of the muons coming from the muon spectrometer, to candidate tracks in the vertex telescope, proceeds by taking into account the multiple scattering and energy loss of the muons in the hadron absorber.

In the following, several abbreviations will be used, which are explained here. The Vertex Telescope is often referred to as VT. We also use the expression VT

Per.	Beam En.	Start – Stop	Triggers	Remarks
1	400 GeV	2004/09/17 2004/09/20 runs 10015 – 10116	6.3×10^6	Absorber: 40 cm Fe VT 0: ATLAS miscrostrip VT 1: BNL miscrostrip 3 MWPC planes switched off
2	400 GeV	2004/09/20 2004/09/24 runs 10117 – 10361	5.2×10^6	Absorber: 40 cm Fe VT 0: ATLAS miscrostrip VT 1: ALICE pixel 3 MWPC planes switched off
3	400 GeV	2004/09/24 2004/10/13 runs 10380 – 11187	24.7×10^6	Absorber: 80 cm Fe VT 0: ATLAS microstrip VT 1: ALICE pixel 4/5 MWPC planes switch. off
4	158 GeV	2004/10/13 2004/10/18 runs 11234 – 11559	11.3×10^6	Absorber: 80 cm Fe VT 0: ALICE pixel VT 1: ALICE pixel 5 MWPC planes switched off
5	400 GeV	2004/10/19 2004/10/21 runs 11580 – 11804	12.9×10^6	Absorber: 80 cm Fe VT 0: ALICE pixel VT 1: ALICE pixel 5 MWPC planes switched off
6	400 GeV	2004/10/22 2004/11/15 runs 11805 – 12888	49.0×10^6	Absorber: 80 cm Fe VT 0: ATLAS microstrip VT 1: ATLAS microstrip 5 MWPC planes switched off

Table 3.1: *Characterization of the six data taking sub-periods.*

tracks to refer to tracks reconstructed in the VT telescope. The muon spectrometer is named shortly PC telescope, PC standing for Proportional Chambers. PC muons and PC dimuons are those muons and dimuons which are reconstructed using the PC telescope's information only. On the other hand, VT muons and VT dimuons are fully reconstructed muons and dimuons, which are first reconstructed in the PC telescope and then matched to reconstructed tracks in the vertex telescope. Furthermore, OS dimuon stands for Opposite-Sign ($+-$) and LS for Like-Sign ($++$ and $--$) muon pairs.

3.2.1 Track Reconstruction

Track Reconstruction in the Muon Spectrometer

The data of the muon spectrometer are the first to be reconstructed, when processing the dimuon sample, because after the hadron absorber the charged particle multiplicity is much lower. As seen in Chapter 2, the spectrometer consists of two sets of 4 stations, which are called the "forward" and the "backward" PC telescopes. The toroidal magnetic field bends charged particle tracks only within the magnet itself, so that in the telescopes the reconstructed tracks are straight lines. The reconstruction is done independently in the two sub-telescopes, and the results are matched in a second step. The toroidal magnet only changes the polar angle of the tracks, leaving the azimuthal angle unchanged: the matching of tracks in the forward and backward telescopes relies on this feature.

Tracks in the backward spectrometer are reconstructed first: in the MWPCs after the ACM magnet the multiplicity is lower, as the contribution from residual hadronic showers is suppressed by the applied magnetic field. Tracks that would cross the iron poles of the magnet are discarded in order to have a sample of muons which all suffered the same minimum amount of multiple scattering and energy loss. Tracks that would miss to leave a hit in the R3 and R4 trigger hodoscopes are also discarded, since they cannot be the real trigger muons. The same procedure is then applied to tracks in the forward telescope (including the cross-check on the trigger hodoscopes), which are finally matched to backward tracks, on the basis of their distance at the centre of the magnet and on the difference between their azimuthal angles.

After the two PC muons kinematics are fully reconstructed, it is checked if the formed pair produces a dimuon trigger (the NA60 trigger logic requires that the two trigger muons must be in different sextants); should that not be the case, the event is rejected. This cut not only select candidates satisfying the trigger logic, but also ensures that the two tracks are formed within the 20 ns wide read-out gate of the hodoscopes, being sufficiently smaller than the one of the MWPCs (~ 80 ns).

Track Reconstruction in the Vertex Telescope

The algorithm used to reconstruct tracks in the vertex detector is a *brute force* algorithm, which tries to build tracks out of all clusters in the telescope. In order to reduce the combinatorics the algorithm is applied in several steps, as described below.

Detector stations are organized in mandatory groups, such that at least one station from each of these groups must contribute to each track; with the BNL microstrip stations not yet aligned, we are left with tracking stations 0–11 (see Table 2.4). Four mandatory groups are defined as follows:

- stations 1, 3, 5 and 8
- stations 0, 4 and 6
- stations 2 and 7
- stations 9, 10 and 11

The first two groups contain the seven small ALICE pixel stations. The third group is composed of the two ATLAS pixel stations: the request of a hit coming from at least one of these two stations ensures that only tracks formed within the 2×25 ns read-out gate of the ATLAS planes are reconstruted (for a demonstration of cleaning up the event by tracks reconstructed from clusters "out of time", see Figure 3.4). Finally, the fourth group is composed of the three large ALICE pixel stations. The composition of the mandatory groups is tuned such that only tracks are reconstructed whose hits are distributed over a reasonably long distance. Moreover, the reconstruction algorithm requires a track to consist of at least 6 hits.

The reconstruction algorithm takes into account the magnetic field of the dipole magnet PT7: at least 3 space points are required in order to reconstruct a track without ambiguity. The reconstruction algorithm, hence, starts by defining a "track seed", composed of three clusters:

- a cluster from one of the stations in the upstream group is paired with a cluster from one of the downstream stations. They are connected with a straight line in the non-bending plane and a relaxed cut is applied on whether this track points to the target region or not;
- the algorithm defines a coarse "road width" by assuming a maximum positive and negative curvature, as given by a 1 GeV particle: a new cluster is then searched inside this path. If it is found, the first "track seed" is formed and a first fit is performed: very loose cuts on the χ^2 and on the vertex position are applied to this fit.

If this first "track seed" passed the preliminary cuts, new clusters from the other stations are added, looking for the ones which fall inside the road width defined by

the track seed. A new cluster is added to a track seed only if: (i) its χ^2-distance from the track seed is reasonably low ($\chi^2 < 4.0$); (ii) if the χ^2 of the new track is good enough ($\chi^2_{\text{track}} < 2.2$); (iii) if the extrapolation of the new track to the vertex region is close enough to one of the targets.

The final track, fitted using a "Kalman filter" algorithm, is accepted if it has a cluster in all the mandatory groups of stations and if its length is above the predefined minimum of 6 hits. Moreover, the algorithm checks how many clusters it shares with already accepted tracks; at most, one shared cluster is allowed: in case of conflict, the tracks with the largest number of cluster or with the best χ^2 is kept.

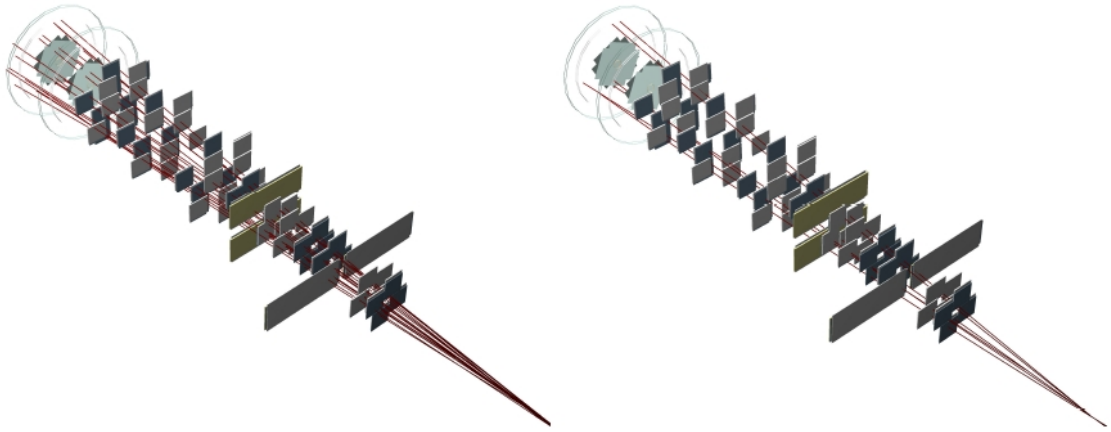

Figure 3.4: *Pile-up rejection in the vertex telescope using the ATLAS pixel as mandatory tracking planes in the track reconstruction. For the same event we plot all tracks (left) and tracks which have a hit in (at least) one of the two ATLAS pixel panes (right).*

3.2.2 Dimuon Track Matching

The matching of a reconstructed dimuon from the muon spectrometer to two track candidates in the vertex telescope proceeds in the following way. For each PC muon the algorithm looks for the matching VT track, among VT tracks with the same charge as the PC muon. In addition, only VT tracks with roughly the same kinematics of the PC muon are considered as matching candidates; this requirement implies that the slopes (k_x and k_y) and the curvatures (C) of the candidate VT track and of the PC muon − corrected for multiple scattering and energy loss in the hadron absorber − should be similar: that is, the comparison is done both in angular and momentum space. Technically, this comparison is performed applying a cut on the χ^2 of the match, defined as:

$$\chi^2_{\text{match}} = \left(\frac{\Delta k_x}{\sigma_{k_x}}\right)^2 + \left(\frac{\Delta k_y}{\sigma_{k_y}}\right)^2 + \left(\frac{\Delta C}{\sigma_C}\right)^2 . \tag{3.1}$$

The σs in the above equation are the sum in quadrature of the corresponding errors for the PC muon and the candidate VT track:

$$\sigma_i^2 = \left(\sigma_i^{\mathrm{PC}}\right)^2 + \left(\sigma_i^{\mathrm{VT}}\right)^2 \ , \qquad i = k_x, k_y, C. \tag{3.2}$$

Our reconstruction settings consider a match only for candidates with $\chi^2_{\mathrm{match}} < 5.0$ (see Chapter 4); for a given PC muon up to 10 VT candidates can be stored for further processing. Selected candidates are refitted loosely constrained by the momentum (curvature) of the PC muon. Finally, if both muons of the PC dimuon have at least one match candidate in the vertex telescope, a joint fit of the two muons is performed, using a common vertex, with an algorithm implementing a "Kalman filter". Each pair of VT tracks, being matched with two different PC muons, is referred to as "VT dimuon", as well as "matched dimuon".

3.2.3 Vertex Finding

The vertex finding algorithm is based on a robust fitting method, which assigns a weight to each of the contributing tracks. Only tracks which have a good fit quality ($\chi^2_{\mathrm{fit}} < 1.5$) and a momentum above 2 GeV/c are selected to contribute to the vertex finding.

The vertex reconstruction is an iterative process which stops when the new vertex z-position and the old one differ by less than 100 μm. Only tracks whose weighted distance from the vertex is reasonably small are attached.

As long as the number of the remaining qualified VT tracks is larger than 1, the search for a new vertex is started. In the final step of the vertex finding − after all vertices have been identified − also the tracks which did not qualify for the vertex finding are attached, if possible, to one of the found vertices. The number of reconstructed vertices per event can be larger than 1, due to:

- pile-up interactions occuring during the read-out time of the vertex telescope, given by the 2×25 ns read-out time of ATLAS pixel planes (by requiring that each track must leave a hit in at least one of the ATLAS pixel planes), as explained in Chapter 2 (the pile-up contribution will be studied in detail in Chapter 4)
- reinteractions of high-energetic secondary particles in downstream targets
- "fake" reconstructed vertices (possibly deriving from "fake" reconstructed VT tracks, but also due to having relaxed cuts on the vertexing algorithm in order not to loose any real vertex)

Regarding the last point, we note that the vertexing algorithm was tuned to detect all possible *distinct* vertices, even if they are relatively close. It happens, however, that in a few cases one real vertex is artificially splitted into two; moreover, fake vertices can occur as a consequence of fakely reconstructed VT tracks, in particular if the multiplicity of hits deposited in the VT tracker is rather high.

3.3 Run and Burst Selection for Runs 11580–11804

3.3.1 Overview and Statistics

In the data taking sub-period corresponding to the 225 runs 11580–11804, $\sim 10\,600$ bursts were collected, corresponding to $\sim 12.9 \times 10^6$ triggers. The collected triggers per burst were $\sim 1\,500$, and represent mainly dimuon ($\sim$ 60–80 %) and "P1–P2" triggers, the latter type being used to measure the trigger efficiency for each run. For simplicity purpose, in the following we will use "period" to indicate the fifth sub-period, without risk of ambiguity.

The two spectrometer magnets, PT7 and ACM, were operated with a current of $\pm$ 900 A and $\pm$ 4000 A, respectively. Runs to be used for the data analysis were taken with all possible combinations of the PT7 and ACM's magnetic field polarities, in order to study any (possible) systematic effects; approximately the same statistics was collected in each of the four possible combinations of the PT7 and ACM's polarities. Apart from collecting dimuons of opposite sign, like-sign muon pairs were also collected, in order to derive the so-called "combinatorial background" [Sha04].

Out of the 225 runs, 123 runs were pre-selected and reconstructed, so far without using the information of the 2 BNL microstrip tracking stations (not yet aligned for the data reconstruction). The other 102 runs were not reconstructed because:

- most of them were too small (immediately aborted after having been started)
- a few runs could not be aligned (they might nevertheless be reconstructed in a future reconstruction step)
- a few runs had problems at the reconstruction stage (often due to the decoding of the BNL microstrips)

In total, 7 725 bursts were successfully reconstructed, corresponding to $\sim 6.0 \times 10^6$ triggers. The statistics of this run period is roughly 7 times larger than that in 2002, but the 10 times higher intensity of the proton beam might require stricter conditions and cuts to obtain a clean data sample for the final physics analysis. Moreover, due to the stringent requirement to select only those tracks passing through the ATLAS pixel planes, the geometrical acceptance will be visibily smaller than in 2002, where the acceptance was only limited by the beam-hole of the BNL microstrip sensors.

Next, the 7 725 reconstructed bursts were scanned. In the following, the distributions are shown for a sample of the most significant variables ensuring a proper quality of the detector performance; a detailed study of the full sample of variables, which will not be discussed in the present work, allows to identify runs and bursts to be discarded from the physics data analysis. In the following we show figures whose contents represent either a variable that is available only as an integral over the whole burst, or the mean of a given variable calculated as the average over all

events in a given burst; the average value over the whole period was also calculated, and is shown as a red "guide line" in some of the plots; the runs' boundaries are furthermore shown by the vertical dashed lines.

Beam Intensity as given by the Argonia Counters

The beam intensity is monitored for each burst by the three argonia counters placed along the beam line (see Chapter 2). The counters give a signal proportional to the charge deposited within each burst, such that they provide a measure of the integrated beam intensity burst by burst, without any information on the beam time profile. During the whole run period, the signals coming from the argonia counters 1 and 2 showed the same behaviour as a function of burst. The top panel of Figure 3.5 shows the behaviour of the signal coming from the counter 1 as a function of burst: as can be seen, a low beam intensity is found only for one run, namely run 11648, which was discarded in order to have the same data taking conditions for the full period to be analysed.

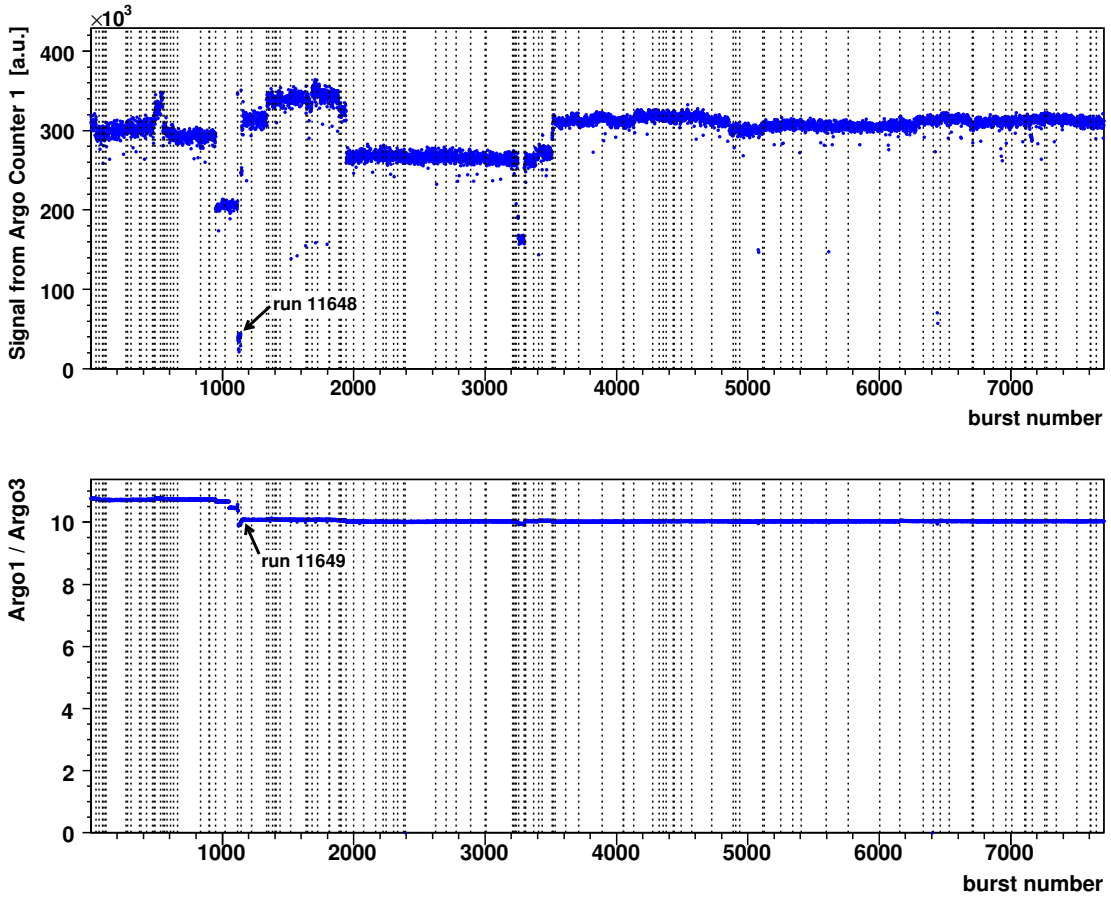

Figure 3.5: *Top panel: signal given by the argo counter 1, proportional to the number of incoming protons, as a function of burst. Bottom panel: ratio between the signals given by the argo counters 1 and 3.*

The ratio between the signals provided by the counters 1 and 3 (or, equivalently, 2 and 3) shows a sligthly different value (the variation being limited to $\sim 8\,\%$) within runs 11598–11648, respect to the remaining period given by the runs 11649–11804, see the bottom panel of Figure 3.5.

Beam Position as given by the VT Vertices' Transverse Coordinates

Figure 3.6 shows the distributions of the average transverse coordinates x and y, respectively, of the VT vertices reconstructed in each burst. In a given burst, the average values of the transverse coordinates of the recontructed VT vertices represent a good estimate of the transverse position of the incoming beam; in this way, Figure 3.6 provides information about the transverse position of the beam during the whole period, burst by burst.

As one can see, the beam position along the y direction (top panel) is roughly constant in the whole period – within small, smooth variations – except possibly for run 11732. On the contrary, the beam position along the x direction (bottom panel) shows marked variations expecially in the first half of the period.

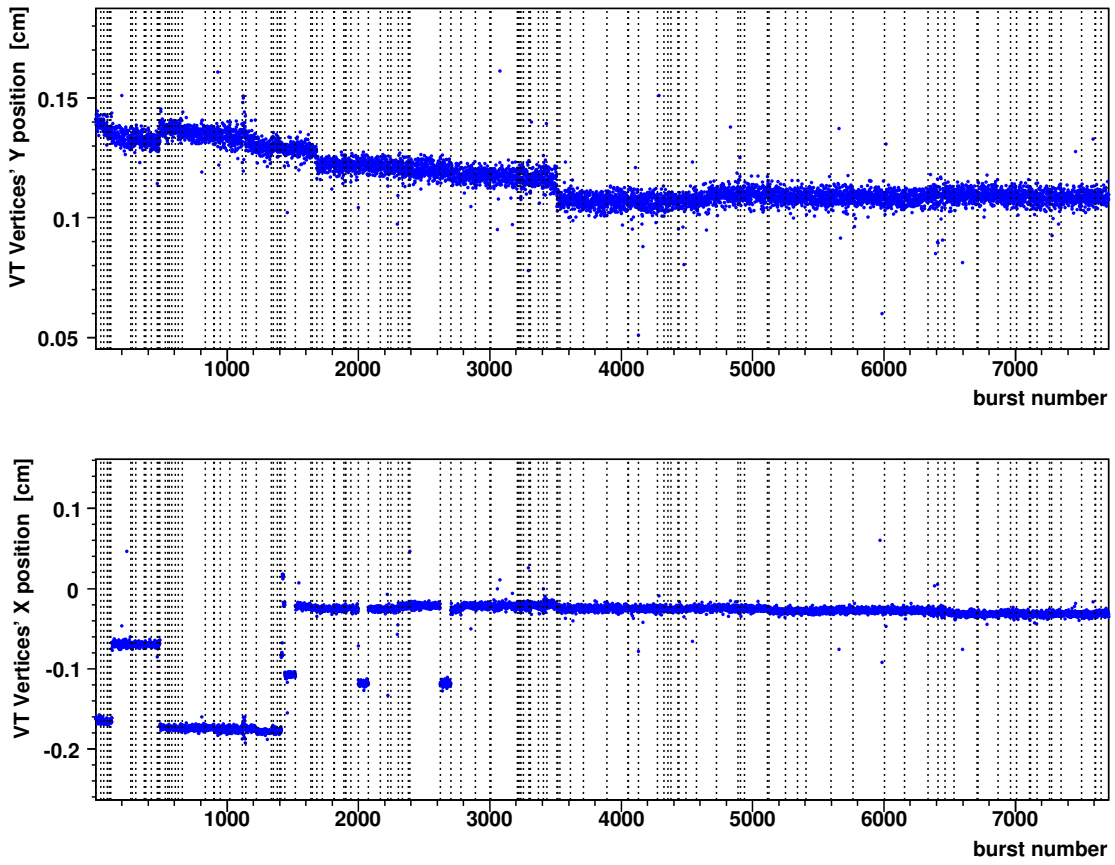

Figure 3.6: *Average transverse coordinates y (top) and x (bottom) of the reconstructed VT Vertices, as a function of the burst number.*

According to Figure 3.6, during the whole period the overall variation of the transverse beam position does not exceed 4 mm, thus being well-contained in the larger transverse size of all the targets.

Fraction of Dimuon Triggers

Figure 3.7 shows the fraction of dimuon triggers in each burst, the remaining fraction being mainly due to "P1–P2" triggers. On average, we collected $\sim 70\,\%$ dimuon triggers; a few runs in which only dimon triggers were collected (runs 11606, 11630–11637, 11732–11736) are also present.

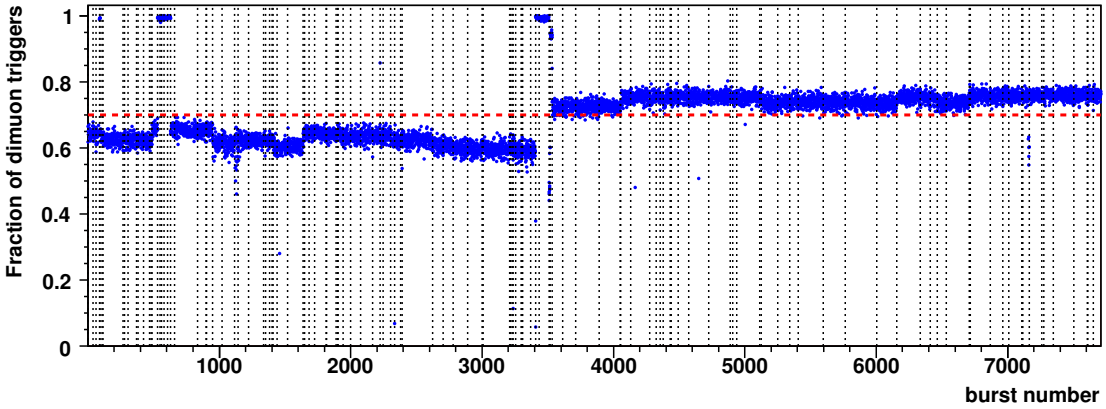

Figure 3.7: *Fraction of dimuon triggers as a function of the burst number.*

Number of Reconstructed Events per Burst

Another monitored variable is the number of reconstructed events per burst, having at least 2 muons in the PC telescope. The corresponding distribution is shown in Figure 3.8. The average number per burst depends slightly on the run period: in the first part (approximately corresponding to runs 11598–11674) the average number of events per burst is $\sim 1\,000$; in the second part (approximately corresponding to runs 11675–11804) the average amounts to ~ 800.
It can be noted that a few (groups of) runs show a number of events well above/under the average relative to the whole period. In particular, in run 11648 all bursts have roughly ~ 100 events, to be compared with the nearby runs having ~ 800 events per burst. Taking into account the distribution shown in Figure 3.5 (signal from the argonia counter 1), one can relate the observed smaller number of reconstructed events to the low intensity of the beam.

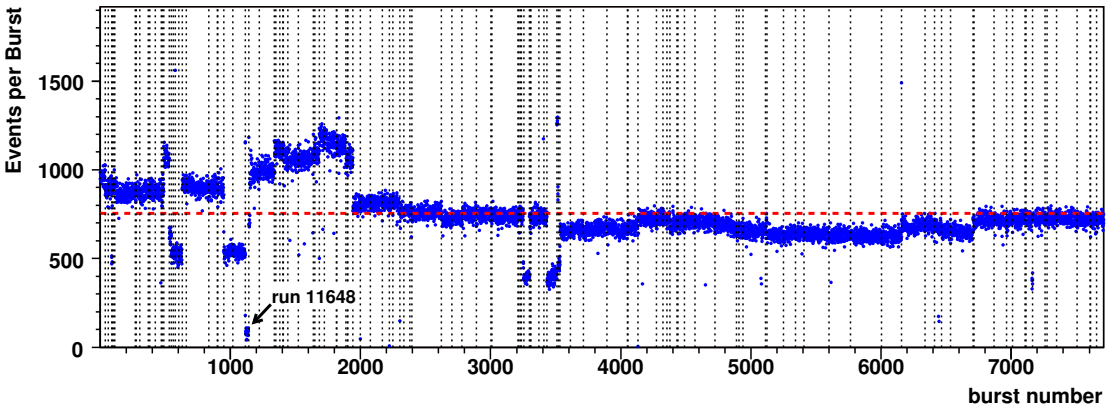

Figure 3.8: *Number of reconstructed events per burst, having at least 2 muons in the PC telescope.*

Fraction of Muons in each PC Telescope Sextant

Analysing the number of PC muons tracked in each of the sextants of the PC telescope allows to discover possible systematic effects in the geometrical acceptance of the apparatus, such as mulfunctioning of the MWPCs or trigger electronics. In Figure 3.9 the fraction of PC muons tracked in sextant 2 is shown, for each reconstructed burst (see Figure 2.3 for the sextants' nomenclature). As one can see, the plotted variable seems to be roughly constant over the whole data taking period. The observed fluctuations are related, besides the inescapable statistical effects, to the different field polarities of the PT7 magnet; the same conclusions hold if one considers the fraction of PC muons tracked in each of the other five sextants.

The fraction of muons in sextant 1–6, averaged over all the reconstructed bursts, are 21, 28, 41, 37, 33 and 43 %, respectively. These values can be explained, at least from a qualitative point of view, invoking the effect induced by the presence of the dipole field of the PT7 in the target region: the magnet deflects into the angular acceptance of the muon spectrometer the low p_{T} opposite-sign muon pairs, which would otherwise be lost in the dead area surrounding the beam line.

Taking into account the vertical orientation of the PT7 dipole field, it is then straightforward to note that the only sextants which do not take any advantage of the described effect are sextants 1 and 2. This then explains why the relative fraction of sextants 1 and 2 are smaller than the fractions relative to the other sextants; in turn, the difference between the sextant pairs 4/5 and 6/3 can be explained remembering that the geometrical acceptance of the muon spectrometer is characterized by the presence of a small inactive zone on the "Jura" side, as we have seen in Figure 2.3: the presence of the inactive zone affects only the sextants 4/5, reducing their occupancies which would otherwise be comparable to those of sextants 6/3.

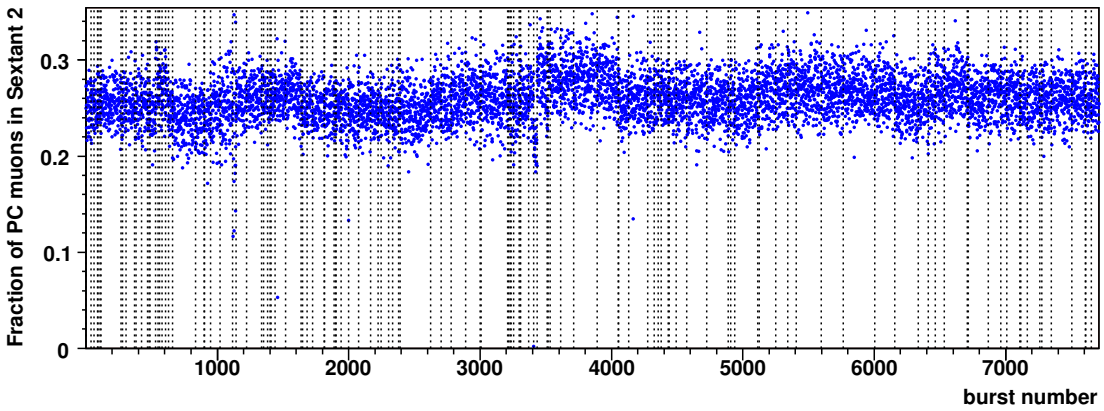

Figure 3.9: *Fraction of PC muons tracked in sextant 2 of the muon spectrometer.*

Number of Hits per Event in the Pixel Chips

For each chip of the pixel tracking stations of the vertex telescope, the average number of hits per event was extracted; in this way, the activity in the vertex region can be monitored. The number of hits per event measured in a given chip usually varies with the given run settings, being a function of the beam intensity and position, the performance of the chip, ...

The observed fluctuations can be as large as a factor of 2; for example, in Figure 3.10 the burst-average number of hits per event in pixel chip 0 of the first plane (a small ALICE pixel plane, see Figure 2.8) is seen to vary between ~ 30 and ~ 60.

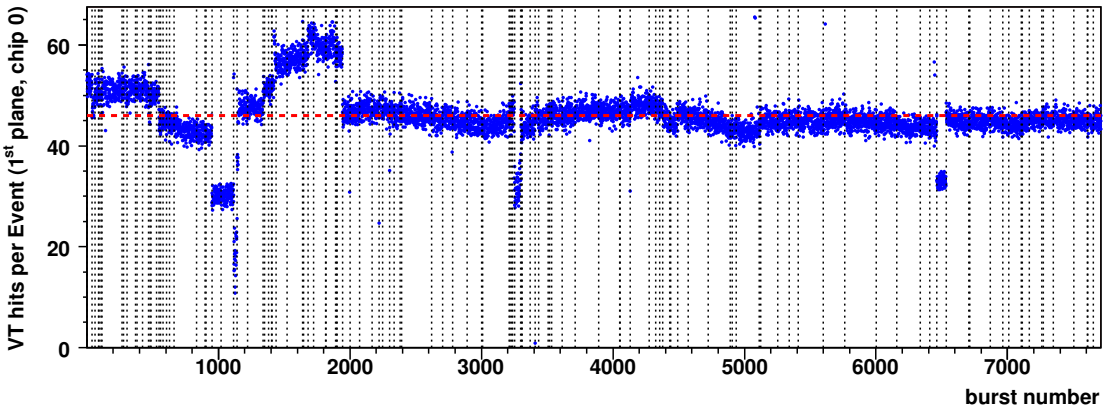

Figure 3.10: *Hits in chip 0 of the first VT plane as a function of the burst number.*

Scanning systematically the number of hits per event in each of the pixel chips composing the vertex telescope makes it possible to note pathological behaviours. This is the case of the 9^{th} tracking plane (composing the small ALICE station covering the central hole in the geometrical acceptance of the first large ALICE station, see Figure 2.8), in which none of the four chips gave any signal during the

whole data taking period we are analysing. Hence, the 9th tracking plane cannot be used for the reconstruction, but it has to be taken into account in the MC generations, as a source of multiple scattering for the particles going through it.

Further problems are observed in other pixel planes. From the end of run 11707 onwards, for instance, no signal was registered any more in any of the 4 chips of the small ALICE pixel plane composing the second tracking station. In Figure 3.11 we show the average number of hits for chip 1, but the vanishing of signal is also present for chips 0, 2 and 3 composing the same plane.

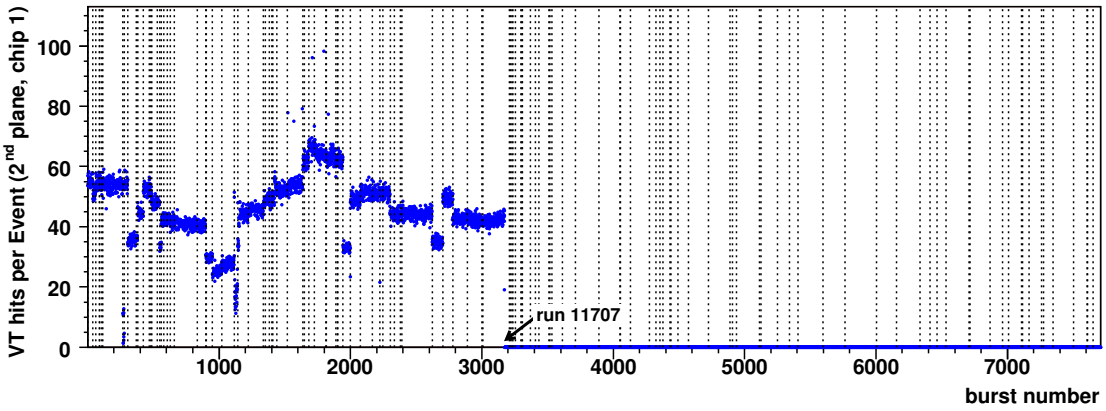

Figure 3.11: *Hits in chip 1 of the second VT plane as a function of the burst number. Chips 0, 2 and 3 also do not see any hits after run 11707.*

Further problems were also observed in the behaviour of some of the pixel planes composing the vertex telescope. Without entering the detailed analysis, we only mention here the results of the observations:

- 10th tracking plane (the first one of the first large ALICE pixel station), chips 4–7: no hits in runs 11656, 11657
- 11th tracking plane (the second one of the first large ALICE pixel station), chips 0–3: no hits in runs 11618, 11656, 11657
- 15th tracking plane (the second one of the last large ALICE pixel station): chip 4 recorded too many hits (perhaps having been touched by the beam).

Number of VT Tracks per Event

The number of VT tracks per event (i.e. the charged tracks reconstructed in the vertex telescope) has also been monitored. The corresponding distribution is shown in Figure 3.12.

As one can see, only run 11732 shows an abnormal (in this case, abnormally low) number of reconstructed VT tracks: a more detailed analysis has shown that in run

11732 many VT tracking planes had problems, resulting in a very low overall occupancy. It is worth noting that run 11732 had some problem also in the distribution of the number of PC muons per event (not shown here), although the tracking in the vertex and PC telescopes are performed indipendently from each other.

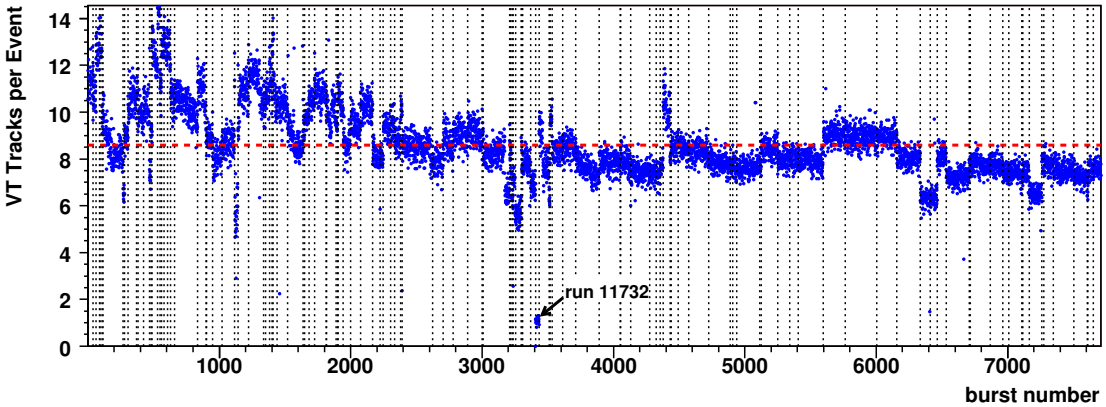

Figure 3.12: *Number of reconstructed VT tracks per event.*

3.3.2 Runs excluded from the Physics Data Analysis

Further investigations have clarified the nature of the anomalous behaviour shown by the bursts relative to the few "pathological" runs. Without entering details we list here the discarded runs, briefly quoting the reason of their exclusion:

- in runs 11618 and 11732 many VT tracking planes had problems (the overall occupancy was very low)
- runs 11661, 11676 and 11690 showed problems with the algorithm which does the automatic alignment of the tracking planes. Once the setup files will be corrected, these runs could be recovered in a second reconstruction phase
- in run 11648 the beam intensity was very low with respect to the run period average (as was, consequently, the number of reconstructed events); in order to have a data sample with the same data taking conditions, this run was excluded
- the runs showing a number of reconstructed events well above/below the average relative to the whole period (see Figure 3.8) were checked with more details. At the end, all of them were retained except for runs 11606 and 11633, which were not even mentioned in the paper logbook
- run 11610 was excluded because all its bursts have a number of VT dimuons well below the run period's average

In total, 9 runs were exluded, corresponding to 329 bursts. In the remaining 114 runs we have 7 396 bursts.

3.3.3 Bursts further excluded from the Analysis

In Figure 3.6 we can see that in a few isolated bursts the average x and y coordinates of the reconstructed VT vertices differ significantly from the corresponding values in the other bursts of the same run; this small sub-sample amounts to 51 bursts, which were excluded from the physics analysis.

After this further exclusion, we are left with a final sample composed by 114 runs, corresponding to 7 345 bursts which contain 3 814 474 dimuon triggers. The event selection, which defines the final sample to be used for the physics data analysis, will be described in the next Chapter.

4

Event Selection

This chapter is devoted to a detailed study of the events contained in the selected runs and bursts. As already pointed out in Chapter 3, our sample consists of 3 814 474 events with dimuon triggers; out of these, 284 263 events have a matched dimuon: 251 065 OS and 33 198 LS dimuons.

We start by discussing the observed average number of reconstructed VT vertices per event, on the basis of an estimate of the interaction pile-up rate. We then analyze some characteristics of the reconstructed VT vertices, namely their spatial distribution and the average number of VT tracks attached, without applying any quality cut. The last section is devoted to a study of the matched dimuons, which will enable us to define three selection cuts in order to enhance the quality of the resulting data sample, to be further used for the physics data analysis.

4.1 Pile-up Estimation

Ideally, the events we would like to study should have one matched dimuon (i.e. one pair of PC muons matched to a pair of VT tracks, see Chapter 3), coming from a well-defined VT vertex reconstructed within the volume of one of the sub-targets used in the experiment. Actually, if we look at the sample of reconstructed events having a matched dimuon, we observe that the average number of muon pairs tracked in the PC telescope within the time resolution of the R1-R4 trigger is ~ 1, see the left panel of Figure 4.1; on the contrary, the VT telescope integrates, within the 2×25 ns read-out interval given by the mandatory ATLAS tracking stations, an average number of interactions larger than one, see the right panel of Figure 4.1.

As explained in Chapter 3, three main mechanisms may be invoked to explain a number of reconstructed vertices per event larger than 1:

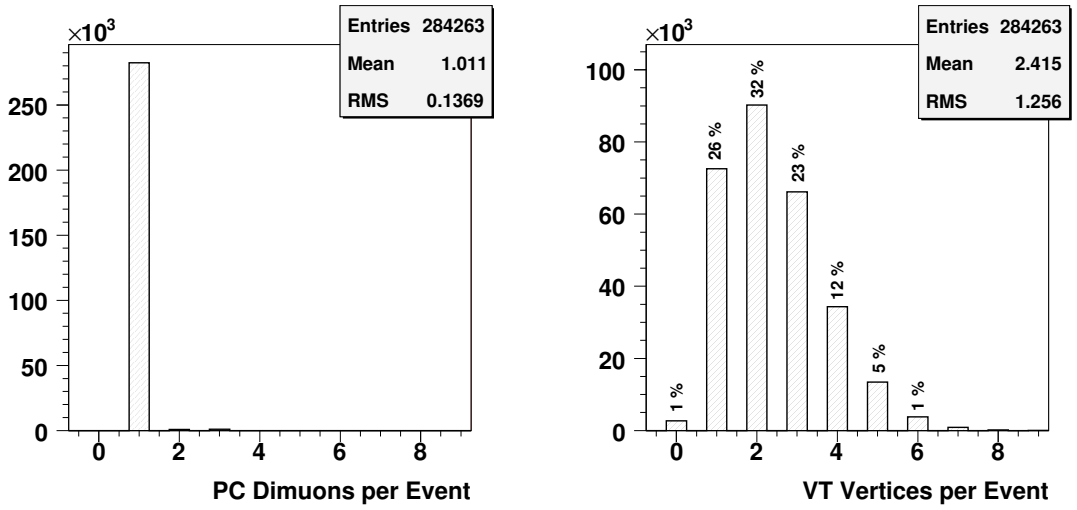

Figure 4.1: *Number of PC dimuons (left panel) and VT vertices (right panel) reconstructed per event, for the sample containing events with a matched dimuon.*

- pile-up interactions occurring during the read-out time of the vertex telescope, given by the 2×25 ns read-out time of the ATLAS pixel planes
- reinteractions of high-energetic secondary particles in downstream targets
- "fake" reconstructed vertices (possibly deriving from "fake" reconstructed VT tracks, but also due to having relaxed cuts on the vertexing algorithm in order not to loose any real vertex)

In the following we will estimate the expected average number of pile-up interactions occurring during the read-out gate of the vertex telescope; in order to extract the corresponding contribution to the observed number of reconstructed VT vertices, this estimate has to be further convoluted with the vertexing efficiency.

The calculations we are showing were done according to Ref. [Lou07]. There are three inputs needed to calculate the interaction pile-up rate:

1. the instantaneous beam intensity
2. the effective thickness of the material in which the beam protons are expected to interact
3. the time window within which the signals are integrated in the detectors collecting the data that we are considering: in our case it is given by the 2×25 ns read-out window of the mandatory ATLAS tracking stations

The average instantaneous beam intensity, I, in the 2004 run was approximately $2 \cdot 10^9$ protons per burst, with an effective spill length of 4.8 s: $I = 4.2 \cdot 10^8$ s^{-1}. As

outlined in Chapter 2, the targets had a sufficiently large transverse size, such that the whole beam was intercepting the targets, even when being sligthly displaced from the nominal position. In the following we assume that the instantaneous beam intensity within the spill was approximately constant; assuming a flat time profile of the beam within the burst, leads to the minimum pile-up estimation which is compatible with a given value of the burst-integrated intensity. Thus, the value we are going to calculate will be a lower limit for the average number of interactions we expect to observe within the read-out time window of the VT telescope.

The thickness of the material in which the beam is expected to interact is given, in our case, by the total thickness of the target system, i.e. $\lambda_{\rm tgt} = 7.51\,\%\ \lambda_I$ (see Table 2.3); here we are not considering the probability of the beam to interact with the other materials placed along the beam line (beamscope sensors, entrance and exit windows of the cryostat and target box) because the corresponding probability can be safely neglected. The following calculations can be divided into three steps:

1. we calculate the probability $P(n_{\rm ex})$ to have $n_{\rm ex} \geq 0$ *extra* protons (besides the one starting the acquisition time-window) arriving at the target system within the 2×25 ns read-out window of the vertex telescope

2. for each value of $n_{\rm ex}$ we calculate $N(n_{\rm ex})$, the average number of interactions induced by the $n_{\rm ex}$ extra protons

3. we sum the quantities $N(n_{\rm ex})$ over $n_{\rm ex} \geq 0$, weighting each value by the corresponding probability $P(n_{\rm ex})$: in this way we find the average number $\langle N_{\rm ex} \rangle$ of interactions induced by the extra protons arriving at the target system within the 2×25 ns VT read-out window started by the interaction which gave the trigger

At the end, we will find the number of extra VT vertices we expect to be reconstructed from the $\langle N_{\rm ex} \rangle$ extra interactions, taking into account the tracking and the vertexing efficiencies.

Number of Extra Protons Arriving at the Target System

Assuming that the time profile of the beam is approximately constant wihtin each burst, the average number of protons arriving to the target within the $\Delta t = 2 \times 25$ ns read-out window of the vertex telescope is given by

$$\lambda = I \times \Delta t = 4.2 \cdot 10^8 \times 50 \cdot 10^{-9} = 21.$$

The probability to have n incoming protons within the time interval Δt is then given by the Poissonian probability distribution with mean value λ:

$$\frac{\lambda^n e^{-\lambda}}{n!}\ . \tag{4.1}$$

In our case, the time interval Δt is started by a dimuon trigger, that is, by the interaction of a beam proton with a nucleus of any of the targets; it can be shown [Ram07], however, that even in this case the probability of having n incoming protons within the time interval Δt is still given by the expression (4.1). We can then safely conclude that the probability to have $n_{\rm ex}$ extra incoming protons within the time interval Δt, besides the one which gave the trigger, is given by

$$P(n_{\rm ex}) = \frac{\lambda^{n_{\rm ex}}\, e^{-\lambda}}{n_{\rm ex}!} \ . \tag{4.2}$$

Average Number of Interactions Induced by the Extra Protons Arriving at the Target System

Focussing now on a particular value of $n_{\rm ex}$, we would like to calculate the average number of interactions induced in the target system by the $n_{\rm ex}$ protons. The situation is such that each of the $n_{\rm ex}$ protons has the same probability to interact with the target system

$$p = 1 - e^{-\lambda_{\rm tgt}} \tag{4.3}$$

Furthermore, the probability of one proton to interact is independent of the other extra protons' fate. It then results that the probability to have k extra protons interacting ($k = 0, \ldots, n_{\rm ex}$) out of the $n_{\rm ex}$ arriving within the time window Δt, is given by the binomial probability distribution:

$$P(k; n_{\rm ex}) = C_k^{n_{\rm ex}} \cdot (1-p)^{n_{\rm ex}-k} \cdot p^k \ , \tag{4.4}$$

where

$$C_k^{n_{\rm ex}} = \binom{n_{\rm ex}}{k} = \frac{n_{\rm ex}!}{k!(n_{\rm ex}-k)!} \ .$$

We are now in the position to calculate $N(n_{\rm ex})$, which is the average number of interactions induced by the $n_{\rm ex}$ extra protons: it is simply the sum of all the values of k consistent with the given $n_{\rm ex}$, weighted by their individual occurring probability $P(k; n_{\rm ex})$:

$$N(n_{\rm ex}) = \sum_{k=0}^{n_{\rm ex}} k \cdot P(k; n_{\rm ex}) = \sum_{k=0}^{n_{\rm ex}} k \cdot C_k^{n_{\rm ex}} \cdot (1-p)^{n_{\rm ex}-k} \cdot p^k \ . \tag{4.5}$$

Total Average Number of Extra Interactions within the Target System

Starting with the expression (4.5), we now have to sum the quantities $N(n_{\rm ex})$ over all the $n_{\rm ex} \geq 0$ in order to get the total average number $\langle N_{\rm ex} \rangle$ of extra interactions. The summation has to be performed, rather obvioulsy, weigthing each value $N(n_{\rm ex})$, given by (4.5), with the corresponding probability $P(n_{\rm ex})$, given by (4.2):

$$\langle N_{\rm ex} \rangle = \sum_{n_{\rm ex}=0}^{\infty} N(n_{\rm ex}) \cdot P(n_{\rm ex}) \ . \tag{4.6}$$

In practice, the summation can be stopped when the last added term gives a contribution which is smaller than a negligible fraction of the partial sum.

Substituting the values $\lambda = 21$ and $p = 1 - e^{-0.0751} \approx 0.0723$, valid for the 2004 proton run, we find that the expected number of extra interactions *besides* the one which gave the trigger is

$$\langle N_{\text{ex}} \rangle = 1.51,$$

that is, we expect an average number of $1.5+1 = 2.5$ beam–target interactions to be integrated within the read-out window of the ATLAS pixel detectors for each dimuon trigger. In order to get the corresponding number of reconstructed VT vertices, we have to take into account the vertexing efficiencies; with an assumed overall vertexing efficiency of $\sim 85\,\%$ [Wöh04], we expect to see

$$2.5 \cdot 0.85 \approx 2.13$$

VT vertices per dimuon trigger, assuming that the beam arrives uniformly within the burst. As one can see, this value is in good agreement with the observed mean value 2.4, see Figure 4.1.

Hence, according to these calculations, the observed number of reconstructed VT vertices per event is consistent with the contribution given by the interaction pile-up, without invoking any significant further constribution coming from "fakely" reconstructed VT vertices.

4.2 Characteristics of VT Vertices

From the right panel of Figure 4.1, we see that $\sim 73\,\%$ of the events with a matched dimuon have more than one reconstructed VT vertex, and we showed how this multiplicity can be quantitatively explained taking into account the interaction pile-up occurring within the read-out time window of the vertex telescope. In such events, the reconstructed VT vertices are sorted according to the order by which the vertexing algorithm find them; in this way, the "best vertex" can be identified as the first vertex found by the vertexing algorithm, which then profites from the full sample of reconstructed VT tracks. As a result, the "best vertex" typically is the one with the largest number of attached tracks.

In addition, two "quality" parameters are defined characterising the VT vertices. These parameters are related to the overall compatibility of the VT tracks with the VT vertex to which they are attached.

It is worth noting that in the present analysis we do not apply any additional cut to the quality of the reconstructed VT vertices, besides the ones already given by the reconstruction algorithm (see Chapter 3). The quality of a VT vertex is not correlated with the vertex to be the origin of a matched dimuon; we must always look at all the reconstructed VT vertices, not only at the "best" one, and see which one of them is more likely to have produced the matched dimuon.

Number of Attached VT Tracks per VT Vertex

The quality of a VT vertex depends mainly on the number of tracks attached to it: in general, the more tracks contribute to identify the interaction vertex, the higher the pointing accuracy and, hence, the better the quality. Table 4.1 summarizes the mean number of VT tracks attached to the reconstructed vertices for the nine sub-targets, together with the RMS of the corresponding distributions. The mean number of attached tracks observed for each sub-target depends both on:

- the nuclear mass number A of the material composing the target, because the charged particle multiplicity increases with increasing A
- the z-position of the production target, because of the geometrical acceptance of the vertex tracker: forward produced tracks pass through the beam hole of the vertex stations and cannot be detected, this effect being more visible for the downstream targets

The numbers shown in Table 4.1 are affected by both these effects. In order to have a good confidence on the vertex-target association, Table 4.1 and Figure 4.2 refer to a restricted sample of "best vertices" which are reconstructed within one target width from the centre of the corresponding target.

Tgt	Average	R.M.S.
Al	5.10 ± 0.01	3.1
U	6.21 ± 0.01	3.5
W	6.54 ± 0.01	3.9
Cu	6.19 ± 0.01	3.8
In	5.74 ± 0.01	3.4
Be1	4.35 ± 0.01	2.5
Be2	4.04 ± 0.01	2.2
Be3	4.08 ± 0.01	2.2
Pb	4.99 ± 0.01	2.6

Table 4.1: *Average number of tracks attached to the reconstructed vertices.*

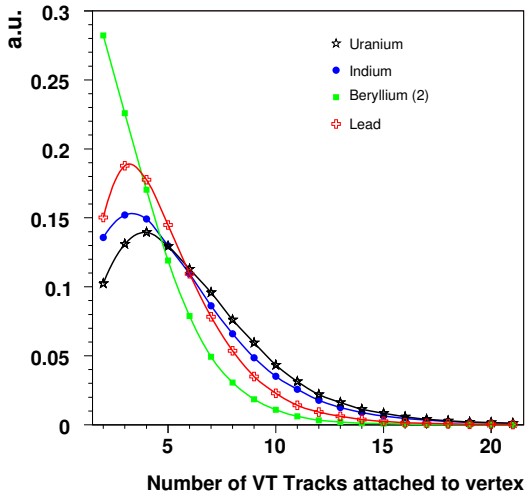

Figure 4.2: *Number of VT tracks attached to the interaction vertices.*

z-Distribution of the VT Vertices

We now consider the VT vertex distribution along the z-direction; this will allow us to extract the spatial resolution of the vertex tracker, along the z-direction, which plays a crucial role in the analysis, because a bad resolution could prevent us from correctly identify the interaction vertices. Here, we take into account only the "best vertex" for each event, without any further restriction.

As one can see, by looking at Figure 4.3, nine peaks corresponding to the nine sub-targets are clearly visible (expanding the z-range either upstream or downstream would not allow us to see further structures, because the vertexing algorithm was set to reconstruct only those VT vertices which originate in the target region). The distribution can be explained by a superposition of 9 pairs of Gaussians: for each pair, the two Gaussians account for "good" and "bad" vertices, respectively. The mean values of all the Gaussians were fixed by previous inspection, while all other free parameters (normalizations and widths) were optimized by the fit.

In order to find the z-vertexing resolution of the vertex tracker, the widths extracted from the fit (i.e. the widths of the "good quality" Gaussians) have to be deconvoluted from the target widths; the deconvolution was performed assuming, for each target, the following relation linking together $\sigma_{\rm tot}$ extracted from the fit, the resolution $\sigma_{\rm VT}$ of the vertex tracker and the width a of the target:

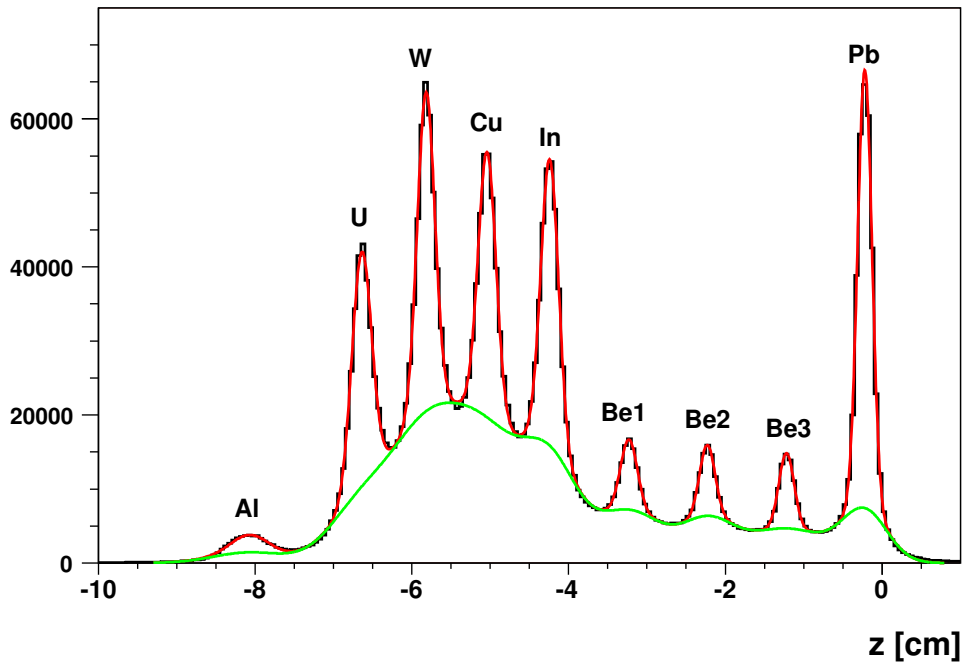

Figure 4.3: *z-coordinate of the "best" VT vertex. All dimuon triggered events are considered (including those without matched dimuon) The fit function (red line) is the superposition of nine pairs of Gaussians; the internal, green line represents the superposition of the Gaussians describing the "bad quality" vertices.*

$$(\sigma_{\mathrm{tot}})^2 = (\sigma_{\mathrm{VT}})^2 + \left(\frac{a}{\sqrt{12}}\right)^2 , \tag{4.7}$$

see Appendix B. The deconvoluted values can be found in Table 4.2, while Figure 4.4 shows the relation between the resolution and the z-position of the corresponding sub-target.

As one can see, the resolution improves as a function of z, mainly due to the fact that the reconstructed tracks are extrapolated over a smaller distance. Note that the tracks from more downstream targets also undergo less multiple scattering and, hence, have a better pointing accuracy.

Tgt	$\boldsymbol{z}$ [cm]	$\boldsymbol{\sigma_{\mathrm{VT}}}$ [mm]
Al	-8.15	2.050 ± 0.020
U	-6.65	1.230 ± 0.010
W	-5.85	1.090 ± 0.010
Cu	-5.05	1.060 ± 0.010
In	-4.25	0.970 ± 0.010
Be1	-3.25	0.897 ± 0.009
Be2	-2.25	0.808 ± 0.008
Be3	-1.25	0.778 ± 0.008
Pb	-0.25	0.714 ± 0.007

Table 4.2: *Resolution of the vertex tracker after deconvolution.*

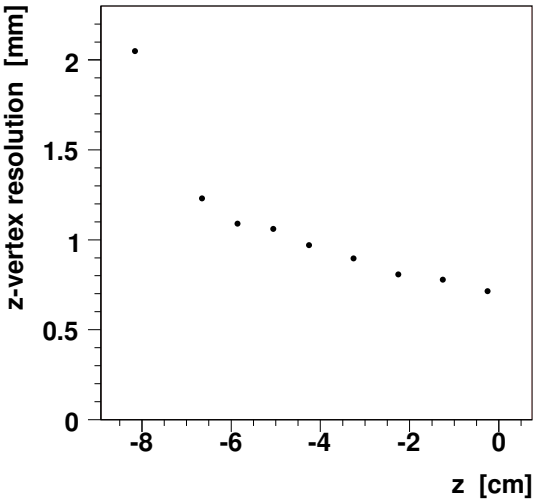

Figure 4.4: *VT spatial resolution along z of the "best" VT vertex, as a function of z.*

VT Vertex Transverse Coordinates

As we saw in the previous Chapter, the x and y-distributions of the reconstructed VT vertices allow us to estimate the transverse position of the beam; at the same time, the Root Mean Square (RMS) of each distribution allows us to estimate the corresponding RMS's of the beam, neglecting the vertexing resolution in x and y of the reconstructed VT vertices (the vertexing resolution in x and y is roughly more than one order of magnitude better than in z [Wöh04]).

Figure 4.5 shows the mean transverse position and the RMS of the incoming beam along both the x and y directions, as a function of the run number, as deduced by inspection of the transverse coordinates of the "best" reconstructed VT vertex.

As one can see, the y-position of the beam remains roughly constant over the whole period; the x-position, on the contrary, was moved several times. Different transverse beam positions lead to sligthly different geometrical acceptances, which, however, are automatically taken into account when performing a Monte-Carlo simulation overlayed on real data, as we shall see in Chapter 5.

The RMS of the beam has to be evaluated by deconvoluting the observed RMS values ~ 400 μm (Figure 4.5, bottom panel) from the transverse resolution of the vertex telescope; on the other hand, since we know that the vertex telescope has a transverse resolution roughly one order of magnitude better than the longitudinal one, i.e. $\lesssim 100$ μm, we can assume the observed values to be good estimates for the beam RMS's along the x and y directions. Thus, the beam is rather focused if compared with the observed variations of its position along the x-direction. This ensures that the full beam profile was intercepted by the targets (except possibly by the Al target, as we shall see in the following), which facilitates enormously all target dependent studies.

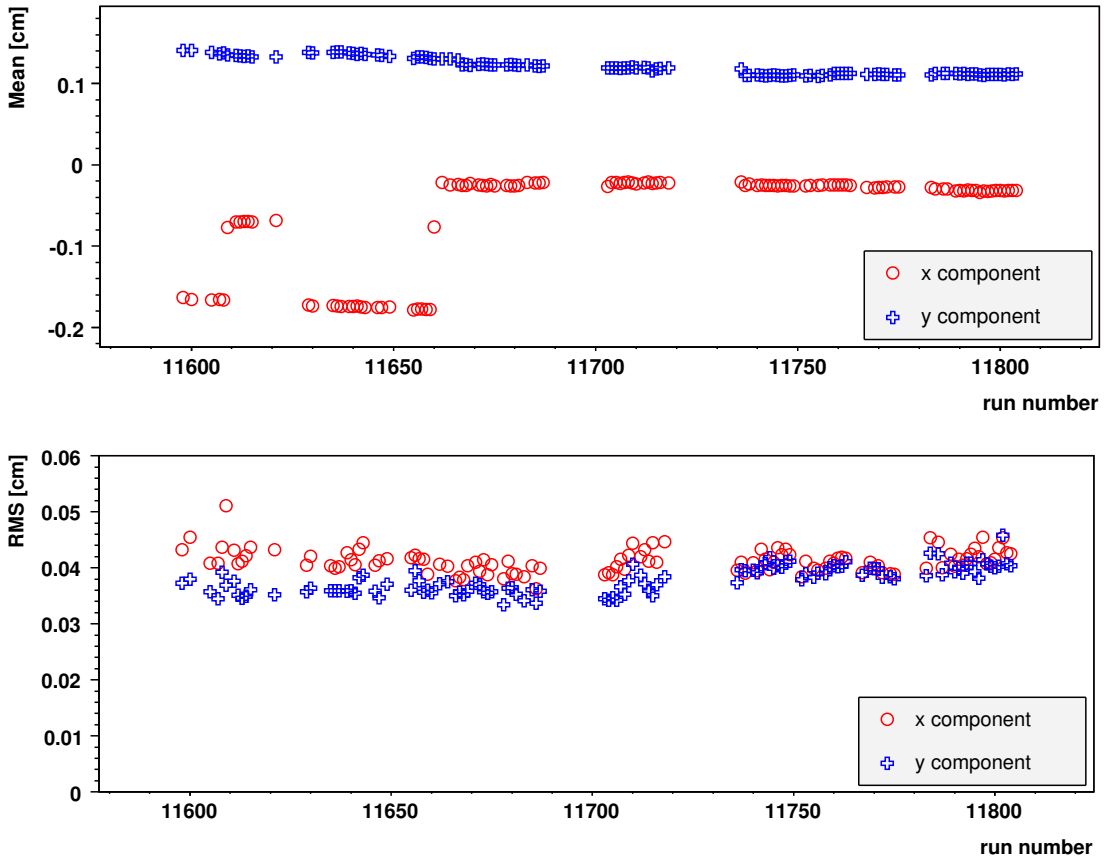

Figure 4.5: *Average transverse position (top) and RMS (bottom) of the incoming beam along the x and y directions, as a function of the run number, as deduced by inspection of the transverse coordinates of the "best" VT vertex. (Note that the limited resolution of the VT telescope is not deconvoluted.)*

4.3 The Problem with the Aluminium Target

As we have previously pointed out, the distribution of the z-coordinate of the reconstructed VT vertices is determined by the z-position of the nine sub-targets. However, a direct comparison between the integral of each peak and the thickness of the corresponding target (expressed in interaction lengths, see Table 2.3) is not straightforward, because only the "best vertex" of each event gives a contribution to Figure 4.3, and vertices having more attached tracks are more likely to be chosen as the "best vertex" by the vertexing algorithm; this introduces a (small) bias in the z-distribution of the "best vertices" favouring the targets which produce a higher number of charged tracks within the geometrical acceptance of the vertex telescope, see Table 4.1.

However, even taking this aspect into account, the events under the aluminium "peak" are still considerably smaller than one could expect, see Figure 4.3; the aluminium target, which not only has twice the interaction lengths of each beryllium target (see Table 2.3), but even profits from a wider geometrical acceptance, appears to see significantly less events.

This and similar observations, which only emerged several months after the end of the data taking period, led to an off-line inspection of the box which contained the target system during the run. It emerged that the Al target was not in its nominal position during the running period of interest to this thesis; it was maximally shifted in the horizontal dimension towards the Salève side, being only limited by the "inner ring" of the window separating the target box from the cryostat box of the beam tracker, see Figure 4.6.

Since the beam was not always centred with respect to the centre of the target system, see Figure 4.5, we are expecting to see only a few p-Al collisions, coming from the tail of the Gaussian distributed beam interacting with the edge of the Al target. Only when the beam arrived sligthly shifted to the Salève side, see Figure 4.5, we observe a significant fraction of p-Al collisions; plotting the z-vertex distribution for the three periods defined by the transverse position of the beam, separately, we indeed see significantly more events when the beam was shifted towards the Salève side (i.e. when it was in position $x < 0$, see Figure 4.5).

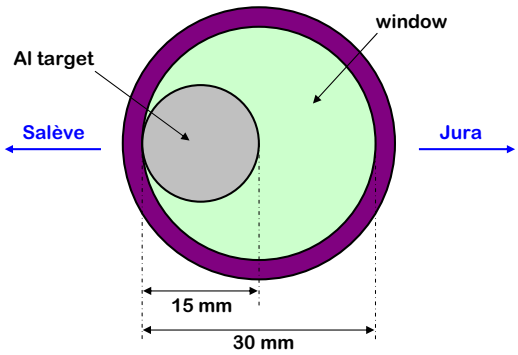

Figure 4.6: *Schematic representation of the Al target position during the runs analysed in this thesis. The target is shifted by ∼7.5 mm in the horizontal dimension towards the Salève side, $x < 0$. In this position it is hardly intercepting the proton beam, whose RMS value is ∼0.4 mm (see Fig. 4.5), if it arrives centred with respect to the target system.*

4.4 Dimuon Selection

In this section we consider all the events having a matched dimuon; an "initial sample" can hence be defined, retaining for each event the dimuon with the best matching χ^2 (defined as the sum of the matching χ^2's of the two single muons). Two independent selection cuts are then proposed, which consecutively applied to the "initial sample" define a "selected sample" to be used in the subsequent analysis (see next Chapters).

4.4.1 P2 Mean Time Difference

In the 2004 proton run a new feature was added to the tracking apparatus in the muon spectrometer: the measurement of the arrival time of each muon at the P2 hodoscope, with respect to the time of the dimuon trigger. In this measurement the trigger gave the start signal to 48 TDC channels, one for each P2 scintillator slab (8 per sextant, see Figure 2.3), which were then stopped by the arrival of a signal in a given slab. The stop signal results from the mean timing of the two photo-multipliers reading each slab, one at each end, and has an accuracy of the order of 1 ns. The dimuon trigger, on the contrary, has a jitter which can be up to 10 ns; however, this jitter is the same for all TDC channels, and cancels out in the *difference* between the crossing times of the two muons.

The difference $\Delta t_{(\mathrm{P2})}$ between the arrival times of the two muons can be used, offline, to identify and reject triggers resulting from two muons coming from two different collisions, closer than 20 ns in time to satisfy the trigger logic. This kind of background is not negligible when running at very high collision rates, as NA60 did in 2004.

The Observed Distributions

Figure 4.7 shows the measured distributions of the time difference between the two muons composing the matched dimuon, for three different samples. The first panel, the left one of the top pair, shows the time difference distribution for all OS dimuons; the second panel, the right one, shows the time difference distribution for all LS dimuons; finally, the bottom panel deals with the OS dimuon sample projected in a mass window $2.9 < M_{\mu\mu} < 3.3$ GeV/c^2 centred on the J/ψ peak.

As one can notice, in both the top panels of the figure, two structures appear: a narrow distribution of events where both muons were produced in the same collision, sitting on the top of a much broader background from pairing muons of different collisions. For the J/ψ sample the background is negligible. For each distribution, a Gaussian fit has been performed on the peaked, central region: apart from noticing that the three Gaussians have similar widths, we can point out that the J/ψ sample has the narrowest distribution, while the LS sample has the broadest one. This result was expected: the LS dimuons always result from uncorrelated muons, which

are likely to originate from interactions which are distant in time; on the other hand, at the energies of the SPS there is only a small probability to have an uncorrelated muon pair having an invariant mass comparable to that of the J/ψ.

Hence, Figure 4.7 shows that the time difference between correlated muons is a Gaussian with an average $\sigma \sim 1.6$ ns (with a minimum value of ~ 1.4 ns relative to the J/ψ sample, being the "cleanest" one we can use). For comparison purpose, we note that the expected fluctuations on the path followed by a muon within the whole apparatus, travelling from the interaction point to the P2 Hodoscope, is on the order of ~ 1 m; hence, being the muon relativistic in the laboratory frame (in fact, we know that muons that reach the P2 Hodoscope have a momentum $\gtrsim 7$ GeV/c) it covers this ~ 1 m distance in ~ 3 ns.

Added to the intrinsic time resolution of the scintillator slabs composing the P2

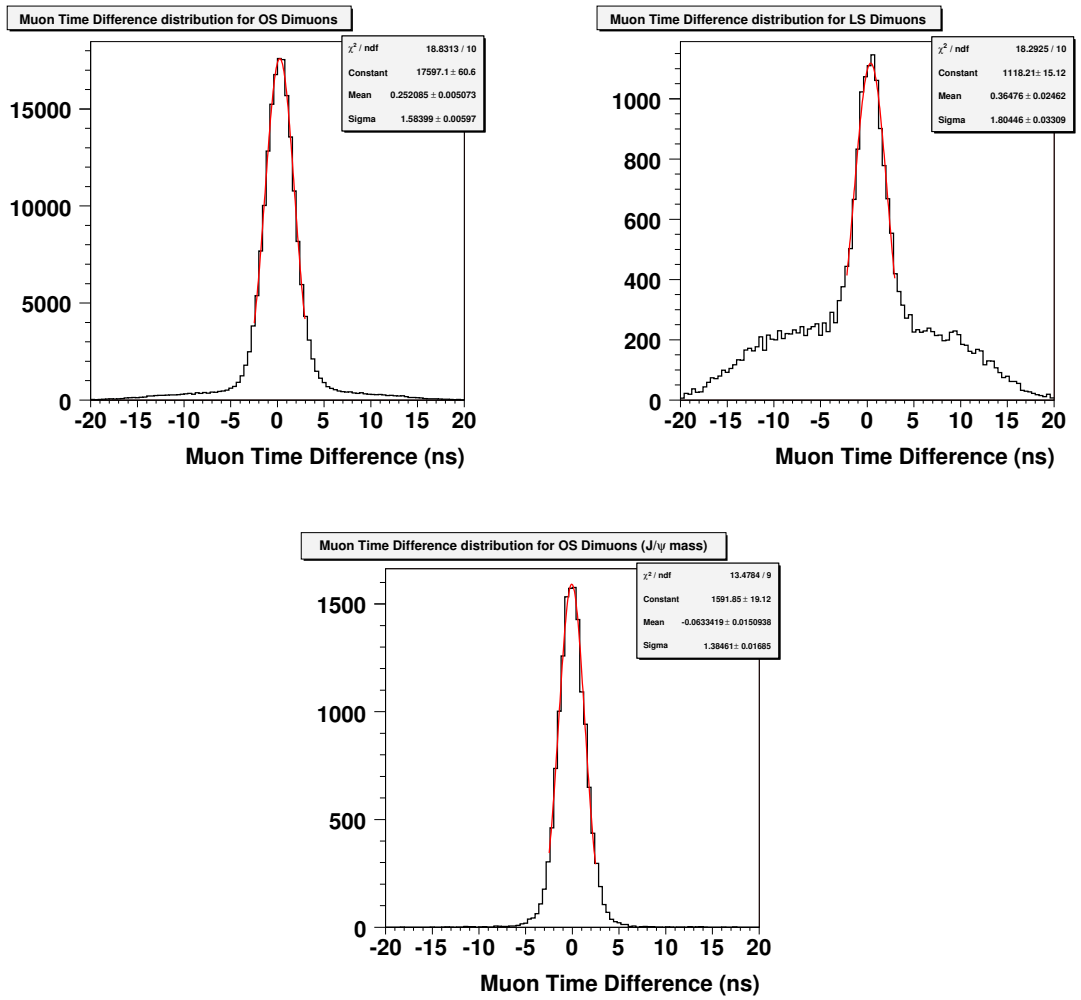

Figure 4.7: *Measured distributions of the time difference between the two muons for the OS and LS dimuon sample, and the OS dimuon sample in the J/ψ mass peak.*

hodoscope, this "fluctuating-trajectory" effects can justify the measured spread in the observed distributions.

In addition, it is worth noting that it is not always possible to evaluate the muon time difference, because one or both muons may not give a signal in the P2 hodoscope, due to its inefficiency. Within the total sample of dimuons we can evaluate the muon time difference in only 224 055 event (199 257 and 24 798 having an OS or LS dimuon, respectively), amounting to $\sim 79\,\%$ of the total sample of 284 263 events having a matched dimuon.

Selection cuts

As we have already pointed out, the difference between the arrival times of the single muons at the P2 hodoscope allows to reject triggers resulting from uncorrelated muon pairs, in which the muons are coming from two different collisions. The cut has the form:

$$|\Delta t_{(\mathrm{P2})}| < n\sigma_{J/\psi},$$

where $\sigma_{J/\psi} = 1.4$ ns is the width of the Gaussian fitting the J/ψ distribution. Table 4.3 shows the number of events corresponding to each of the three selections: (i) no P2-time selection; (ii) $|\Delta t_{(\mathrm{P2})}| < 3.0\,\sigma = 4.2$ ns selection; (iii) $|\Delta t_{(\mathrm{P2})}| < 2.0\,\sigma = 2.8$ ns selection. All variations, shown in percentage, refer only to events with P2-time information.

As we are looking for the best compromise between the loss of correlated dimuons and the improving of the ratio between OS and LS samples (the LS sample being directly linked to the OS "combinatorial background" due to uncorrelated muonic decays of π and K mesons of opposite sign, in which the muons are produced in such a way that they give raise to a dimuon trigger), the cut $|\Delta t_{(\mathrm{P2})}| < 3\sigma_{J/\psi}$ seems to be the best choice assuming that the "J/ψ sample" contains mainly correlated muon pairs. Although we can safely assume that the probability to have high-energetic uncorrelated muon pairs is negligible, nevertheless we may still suppose to have a small contribution from uncorrelated muon pairs even at mass values near to the J/ψ mass; as a consequence, we choose the cut $|\Delta t_{(\mathrm{P2})}| < 2\sigma_{J/\psi}$, corresponding to the range out of which the Gaussian fit on the Δt distribution of the "J/ψ sample" begins to fail (see Figure 4.7, bottom panel).

From now onwards, the $|\Delta t_{(\mathrm{P2})}| < 2\sigma_{J/\psi}$ will then be the "P2-MeanTime" cut applied everywhere, unless explicitely differently specified. Hence, in the following we only consider both: (i) events having a matched dimuon with P2-time information satisfying the cut $|\Delta t_{(\mathrm{P2})}| < 2.8$ ns; (ii) events having a matched dimuon, in which the P2-time information is missing. The sample of events which passed the P2-MeanTime selection cut amounts to 232 383 events (212 847 having an OS dimuon, 19 536 having a LS dimuon).

	OS sample		**LS sample**		**J/ψ sample**	
Total Sample	251 065		33 198		15 916	
Tot. Sample with P2-time inf.	199 257	100 %	24 798	100 %	14 338	100 %
$\lvert\Delta t_{(\mathrm{P2})}\rvert < 4.2$ ns	177 402	89 %	13 376	54 %	14 035	98 %
$\lvert\Delta t_{(\mathrm{P2})}\rvert < 3.5$ ns	171 634	86 %	12 346	50 %	13 823	96 %
$\lvert\Delta t_{(\mathrm{P2})}\rvert < 2.8$ ns	161 039	81 %	11 136	45 %	13 288	93 %

Table 4.3: *Number of events corresponding to various P2-time selections.*

4.4.2 Matching χ^2 for Single Muons

In Figure 4.8 we show the distribution of the matching χ^2 for the single muons composing the matched dimuons. The panel on the left shows the χ^2 distribution for the VT muons forming the OS and LS dimuon samples, integrated in mass; the panel on the right shows the same distributions for the OS dimuons in mass windows corresponding to the mesons ω, ϕ, J/ψ.

As one can see, the distribution of the matching χ^2 for the VT muons composing the LS dimuons is definetely worse than the one corresponding to the VT muons coming from OS dimuons: the LS muon pairs essentially consist of muons deriving from the uncorrelated muonic decays of π and K mesons, in which the *mesons* are tracked within the geometrical acceptance of the vertex telescope and the final *muons* are produced within the geometrical acceptance of the muon spectrometer. Since the kinematics of the muons created in such a decay differs from the kinematics of the mother particles, the matching stage results in a bad matching χ^2.

For OS dimuons, the contribution coming from correlated muon pairs largely dominates over the uncorrelated muon pairs. In this case the matching algorithm matches the two tracks (reconstructed in the vertex telescope and in the muon spectrometer, respectively) left by the *same* particle, hence, having similar kinematics: indeed, the resulting distribution is peaked at lower values than the LS one.

The distributions corresponding to the ω and ϕ mass windows are very similar, while the distribution corresponding to the J/ψ mass is broader; this probably happens because the PC tracks' need to be extrapolated back to the vertex region through the hadron absorber, and we know that the transport software implemented in the analysis framework describes better the energy loss of low-energetic particles than that of high-energetic ones.

Selection Cuts

The probability to have a correct match with $\chi^2 > 5.0$ is negligeble, see Chapter 3, and the cut $\chi^2 < 5.0$ has been applied automatically during the reconstruction

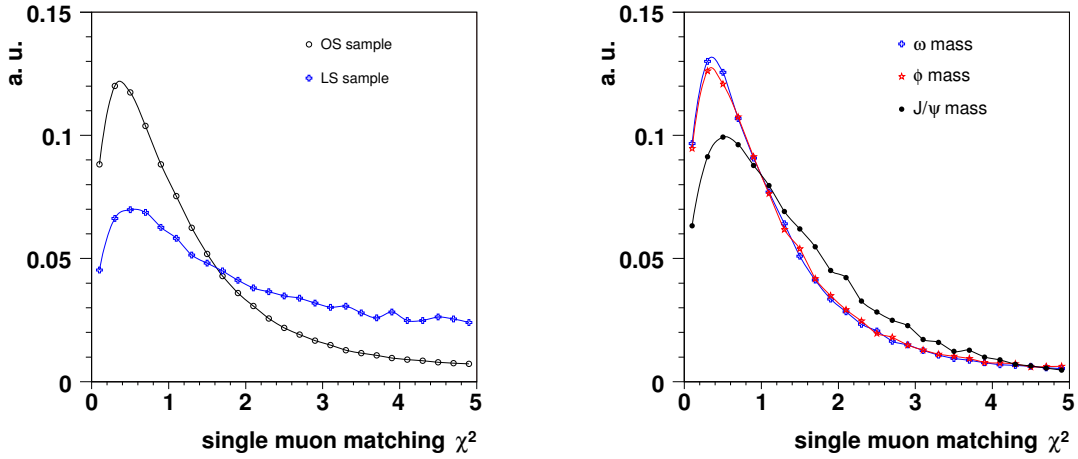

Figure 4.8: *Matching χ^2 for the VT muons forming the OS and LS sample (left panel) and in the mass windows corresponding to the mesons ω, ϕ and J/ψ (right panel) for OS sample only.*

step. However, in order to clean the OS dimuon sample, reducing the fraction of fake matches, a stricter cut can be imposed; Table 4.4 summarizes the available statistics corresponding to the cuts $\chi^2 < 4.0$, $\chi^2 < 3.5$, $\chi^2 < 3.0$, $\chi^2 < 2.5$. It is worth noting that the corresponding samples contain those events in which the dimuon has *both* muons matched within a given χ^2.

In order to roughly establish a cut for our sample, the distributions of the matching χ^2 for the VT muons composing the OS dimuons, projected in four different mass windows, were compared with the superposition of a χ^2 probability function (accounting for the "correct" behaviour of the martching χ^2) and a constant offset (representing, in first order, the contribution from "fake" matches). The χ^2 probability function has the functional form for $x \geq 0$:

$$f(nx; n) = \frac{1}{2^{n/2}\,\Gamma(n/2)}\, x^{n/2-1}\, e^{-x/2}\ , \tag{4.8}$$

where $\Gamma(z)$ is the Euler's Gamma function and the parameter $n = 1, 2, \ldots$ is the number of degrees of freedom of the distribution, which in the present case is set to $n = 3$, see Eqn. 3.1. The fits are shown in Figure 4.9. As one can see, for $\chi^2 \gtrsim 3$ the contribution coming from "properly" matched muons is overcome by the "fakely" matched muons; this latter contribution is particularly noticeable in the second mass bin (from 400 to 650 MeV/c^2), where the "combinatorial background" is highest. From inspection of the plots shown in Figure 4.9, the cut $\chi^2_{\rm match} < 3.0$ was chosen to be the $\chi^2_{\rm match}$ cut for our event sample. We note here that a rigorous procedure to estimate the χ^2 distribution of the "fakely" matched muons should be based on an event-mixing analysis technique; such a study was performed within the analysis of the In-In data of NA60, from which a $\chi^2_{\rm match} < 3.0$ cut was analogously derived.

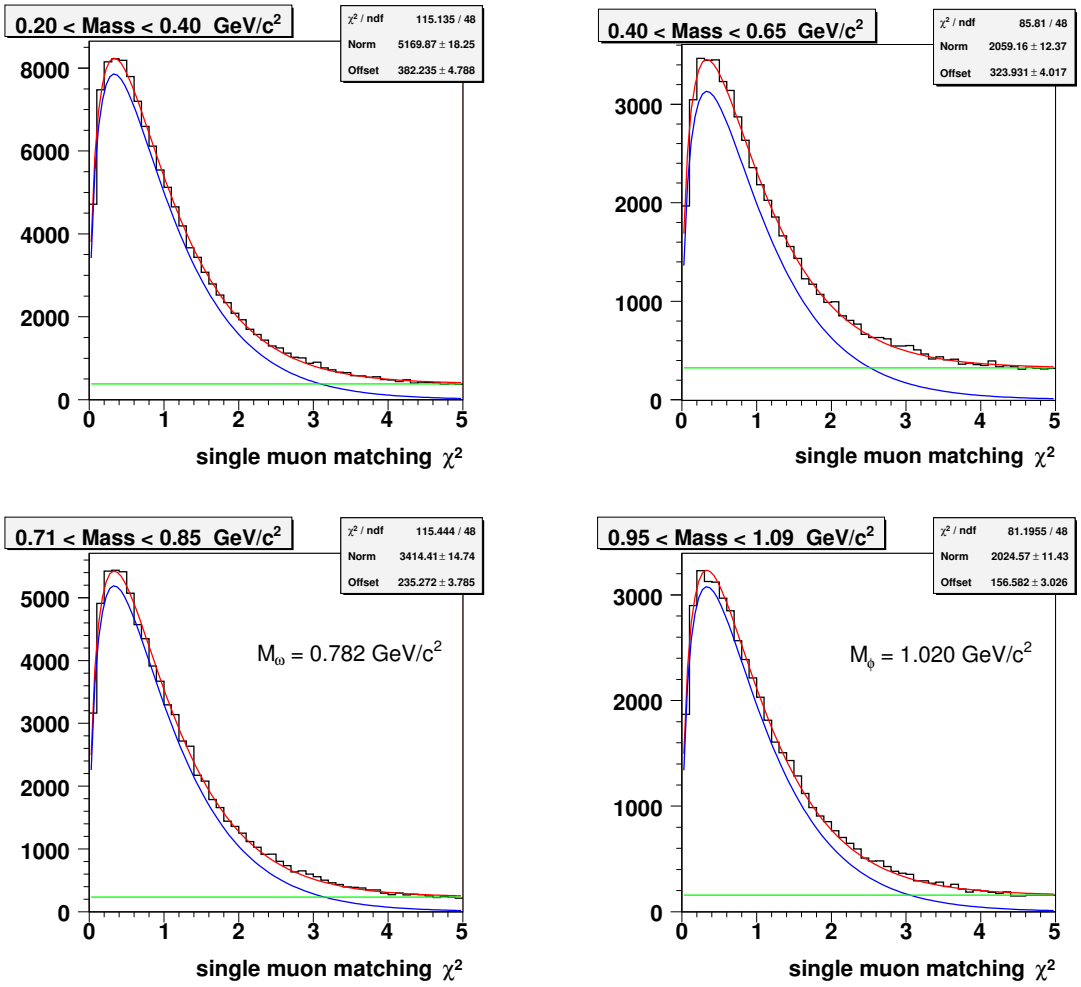

Figure 4.9: *Fit of the distributions of the matching χ^2 for the VT muons forming the OS, in four different mass windows. Each distribution is compared with the superposition of a χ^2 probability function and a constant offset.*

	OS sample		LS sample	
Total Sample	251 065		33 198	
Tot. Sample after P2-time cut	212 847	100 %	19 536	100 %
$\chi^2 < 4.0$	196 486	92 %	14 967	77 %
$\chi^2 < 3.5$	186 452	88 %	12 782	65 %
$\chi^2 < 3.0$	173 799	82 %	10 520	54 %
$\chi^2 < 2.5$	157 038	74 %	8 293	42 %

Table 4.4: *Available statistics corresponding to various single muon matching-χ^2 cuts, for dimuons having passed the selection based on the P2-MeanTime difference.*

4.5 Dimuon–Target Association

We have not yet identified the target from which the matched dimuon originates. In the following, we first discuss a few criteria we can use to find the dimuon's production target; then, we propose a simple procedure which allows us, profiting from the Overlay Monte Carlo simulations, to check our ability in associating a dimuon to its correct production target.

4.5.1 Possible Selection Criteria

All the dimuon-target association criteria we considered rely either on finding the target directly considering the origin of the dimuon (defined as the point of closest approach of its two muon tracks), or on finding the target considering the VT vertex from which we believe the dimuon is coming from.

Considering the origin of the dimuon has the advantage to profit from the direct information from the muon tracks. At the same time, the dimuon's origin is nothing but a two-tracks vertex, hence having a limited spatial resolution; in particular, the error associated to the z-position of the dimuon's origin becomes larger than the typical semi-distance between targets (~ 0.5 cm) for masses below 0.45 GeV/c^2, see Figure 4.10.

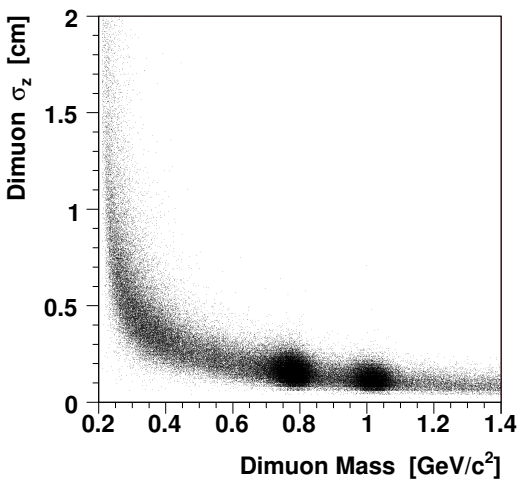

Figure 4.10: *Correlation between the dimuon's mass and the z-error associated to the dimuon's origin.*

In order to overcome these difficulties, we can consider the VT vertices of the event, looking for the VT vertex from which we "trust" the dimuon is coming from (obviously, it is not possible for those $\sim 1\,\%$ events having a matched dimuon but no VT vertices); in this way, we take advantage from the better spatial resolution of the VT vertex (typically consisting of several tracks, see Figure 4.2), but we are

at most indirectly using the information of the dimuon. The association of a given dimuon with one of the VT vertices can be done using two different criteria:

- simply minimising the weighted distance (weighted by the errors) between the VT vertex and the dimuon's origin, either in 3D or along the z-direction only
- considering the VT vertex to which the VT muons are attached to (if any)

Regarding the last point, the following situations are possible: (i) the muons are both attached to the same vertex; (ii) the muons are attached to different vertices; (iii) one of the muons is not attached to any vertex; (iv) none of the muons are attached to any vertex.

Hence, different criteria for the dimuon-target association can be devised, profiting from the various information we have at our disposal. However, nothing assures we are establishing the correct dimuon-target association; a cross-checking procedure can only be devised, based on the Overlay-MC simulations. More details on the MC simulations are given in Chapters 5 and 6; here, we just mention the main aspects:

- a *real* event is read, chosen among the reconstructed *data* collected by the experiment in a given run and burst containing at least a reconstructed PC dimuon
- the VT vertices of the selected event are examined, and one is randomly chosen, among those which are reconstructed within the volume of one of the sub-targets
- the MC vertex is defined, having the same transverse coordinate of the selected real vertex and a re-defined z-coordinate chosen randomly within the target width
- a MC muon pair is generated at the chosen vertex and tracked through the NA60 apparatus, using GEANT. The "hits" left by the MC particles in the various detectors are then put together with the hits stored in the real event from which the MC vertex was deduced (provided we have removed the hits corresponding to the VT muon tracks in the real event): in this way we are realistically simulating a full event without having to generate the full underlying hadronic event
- starting from the ensemble of the MC and real hits, the events in which a muon pair gave rise to a trigger are reconstructed using the same reconstruction settings used to reconstruct the real data, as described in Chapter 3. To make the MC simulation as realistic as possible, the MC tracks leave a signal in a given VT plane with a probability proportional to the plane efficiency estimated from the analysis of the real data

4.5.2 Dimuon–Target Association with Overlay-MC

The analysis of the Overlay-MC simulated events allows us to check the efficiency of a given dimuon-target association criterion, in a very simple way. We first consider a reconstructed MC event with a matched dimuon, and apply the dimuon-target association criterion we want to study; we then compare the identified target in the reconstructed MC event ("reconstructed target") with the target in which the event was actually generated ("generated target"). By studying the correlation between the reconstructed and the generated target, for various dimuon-target association criteria, we can select the most suitable algorithm.

Choice of the Dimuon-Target Association Criterion

We studied five dimuon-target association criteria:

1. we associate to the matched dimuon the target which has the smallest z-distance from the dimuon's origin

2. we associate to the matched dimuon the target which has the smallest z-distance from the dimuon's closest VT vertex. The dimuon's closest VT vertex is the one which minimizes the weigthed distance from the dimuon's origin, along the z-direction, even if it is not close enough to fall into the same target

3. we associate to the matched dimuon the target which has the smallest z-distance from the dimuon's origin (criterion 1), *provided that* this target is the same which minimize the weighted distance from the dimuon's closest VT vertex (criterion 2)

4. for those events in which both the muon tracks are associated to the same VT vertex, the matched dimuon is associated with the target which has the smallest z-distance from the associated VT vertex

5. we relax the previous criterion by looking for those events in which both muon tracks are associated to a VT vertex, although not necessarily to the same: we only require that the two VT vertices correspond to the same target

For each of these dimuon-target association criteria, Table 4.5 summarizes the "available statistics", that is, the sub-sample to which it can be applied (expressed in percent, with respect to the previously selected sample), and the fraction of cases in which the criterion gives the correct dimuon-target association, shortly called "efficiency".

The study is carried out in four different mass bins in the low mass region, as well as in the mass-integrated sample. As one can see, the first criterion has a bad efficiency for the low masses, more than 50 % associations being wrong. Criterion 2 gives higher efficiencies for the low masses, while having a sligthly worse performance

than criterion 1 for higher masses: dimuons with $M \gtrsim M_\omega$ have enough pointing accuracy to more or less correctly identify the target in which they are produced; as a results, criterion 2 gives more homogeneous efficiencies over the whole mass spectrum than criterion 1 does. The third criterion gives better results then the previous ones in all mass bins, though at the expense of a noticeably reduced statistics, with particular reference to the low mass bin.

Concerning the criteria 4 and 5, we note that the latter gives essentially the same efficiency than the former, though allowing to use a larger statistics. It is due to the

Criterion	**Mass Bin** [GeV/c^2]	**Av. Statistics**	**Efficiency**
1	All Masses	100.0 %	69.5 %
	$M < 0.45$	100.0 %	45.4 %
	$0.45 < M < 0.70$	100.0 %	76.0 %
	$0.70 < M < 0.90$	100.0 %	86.7 %
	$0.90 < M < 1.10$	100.0 %	92.8 %
2	All Masses	99.6 %	77.1 %
	$M < 0.45$	99.4 %	70.0 %
	$0.45 < M < 0.70$	99.5 %	78.1 %
	$0.70 < M < 0.90$	99.5 %	81.7 %
	$0.90 < M < 1.10$	99.6 %	85.3 %
3	All Masses	64.5 %	91.4 %
	$M < 0.45$	46.2 %	80.5 %
	$0.45 < M < 0.70$	68.5 %	92.7 %
	$0.70 < M < 0.90$	77.4 %	96.0 %
	$0.90 < M < 1.10$	83.4 %	97.8 %
4	All Masses	68.8 %	86.1 %
	$M < 0.45$	69.5 %	80.2 %
	$0.45 < M < 0.70$	67.5 %	85.9 %
	$0.70 < M < 0.90$	67.6 %	89.9 %
	$0.90 < M < 1.10$	69.9 %	93.7 %
5	All Masses	72.9 %	86.2 %
	$M < 0.45$	73.6 %	80.8 %
	$0.45 < M < 0.70$	71.7 %	86.0 %
	$0.70 < M < 0.90$	71.8 %	89.7 %
	$0.90 < M < 1.10$	74.1 %	93.1 %

Table 4.5: *Available statistics and efficiencies, corresponding to the five dimuon-target association criteria described in the text, for various bins in mass.*

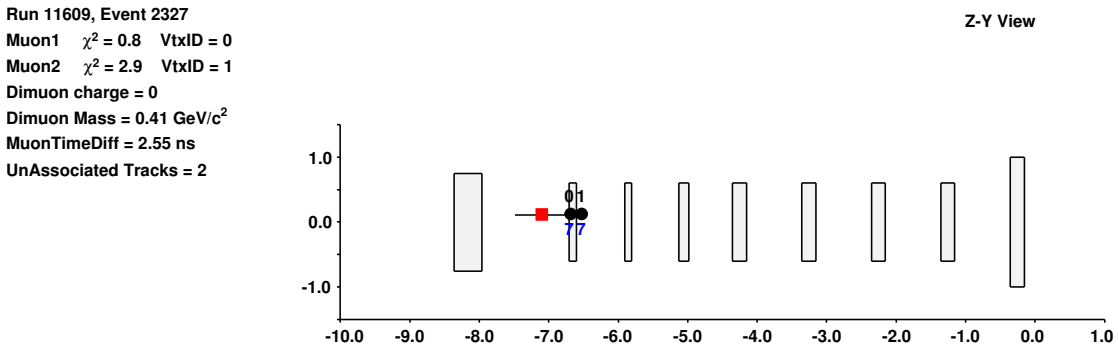

Figure 4.11: *Z-Y representation of the target region in a real event in which two VT vertices are reconstructed very close to each other; the two muon tracks are associated to different vertices, but to the same target.*

fact sometimes we have two VT vertices reconstructed very close to each other, as a result of an artificial splitting of the same original interaction vertex; Figure 4.11 shows an illustrative example, taken from real data: here, two VT vertices are reconstructed suspiciously close to each other and each has a muon track attached to it (each black circle represents a VT vertex, whose index and number of associated tracks are given by the numbers above and under it, respectively; the red square indicates point of closest approach of the matched dimuon); hence, this event would be rejected according to criterion 4, while the fifth criterion correctly assignes the matched dimuon to the second target.

In the first mass bins, criteria 3, 4 and 5 have the same efficiency, but the fifth criterion allows us to keep more events (more than 1.6 times the corresponding statistics available for the third criterion). In the second mass bin, the third criterion offers the best efficiences, without the available statistics being sensibly smaller than in the fourth and fifth criteria. Finally, in the last two mass bins the third criterion not only offers the best efficiency, but it also keep larger statistics than the fourth and fifth criteria.

Hence, since we want to apply the *same* criterion to all masses, maximizing the dimuon-target association efficiency, the third criterion seems definetely to be the best choice.

4.6 Summary of the Cuts Applied to the Dimuon Sample

Having chosen the criterion for the dimuon-target association, we apply it to the real data sample resulting after the P2-MeanTime cut $|\Delta t_{(\mathrm{P2})}| < 2\sigma_{J/\psi}$ and the matching-χ^2 cut $\chi^2_{\mathrm{match}} < 3.0$, obtaining the selected sample to be used for the physics data analysis.

Figure 4.12 shows the OS dimuon mass spectrum before (black line; top) and after consecutively applying the following cuts:

1. P2-MeanTime selection $|\Delta t_{(\mathrm{P2})}| < 2\sigma_{J/\psi}$ (blue line; the second starting from the top)

2. P2-MeanTime and $\chi^2_{\mathrm{match}} < 3.0$ (red line; the third starting from the top)

3. P2-MeanTime, $\chi^2_{\mathrm{match}} < 3.0$ and "dimuon-target association" selections (green line; bottom)

In order to better study the effect of the three selections we have applied to the initial sample, Figure 4.13 shows the three ratios corresponding to each of the three selection steps. As we can see, each selection cut identifies a "signal" which is significantly enhanced at the mass peaks of the ω and ϕ mesons.

The selected sample is composed of 120 579 events, corresponding to 114 360 OS dimuons and 6 219 LS dimuons.

We would like to remark that the selection cuts defining the selected sample exhibit features which are of quite different nature: the cut on the P2-MeanTime difference between the PC muons manages to reject spurious dimuon triggers resulting from uncorrelated muon pairs, on the basis of a temporal information provided

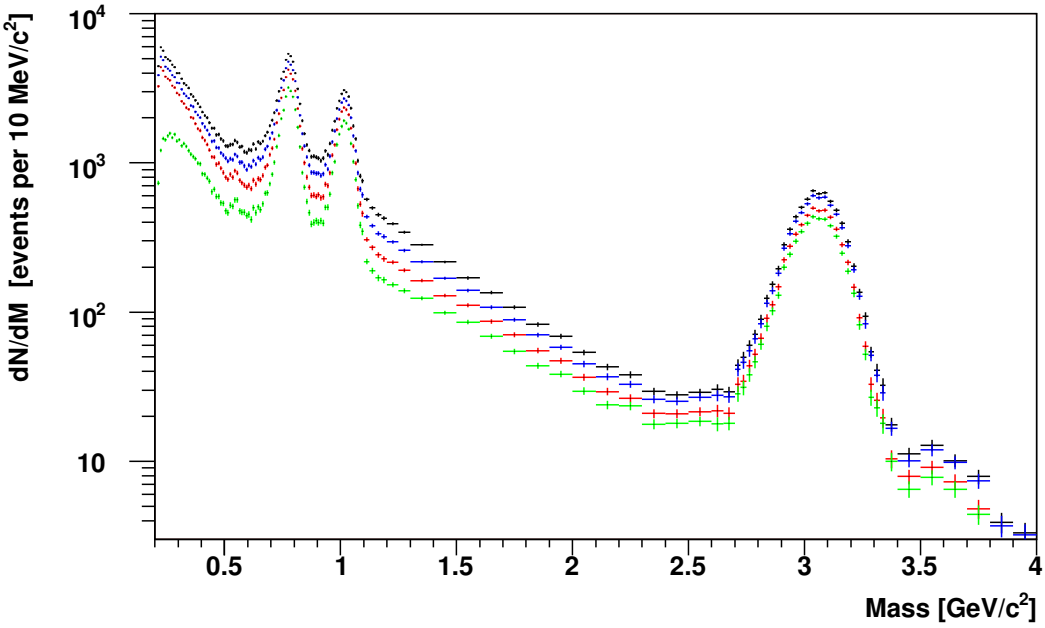

Figure 4.12: *OS dimuon mass spectra for the three samples resulting after: (i) no selection (black line; top); (ii) P2-MeanTime selection (blue line; the second from the top); (iii) single muon matching-χ^2 selection (red line; the third from the top); (iv) "dimuon-target association" selection (green line; bottom).*

by the tracks reconstructed in the muon spectrometer only; the cut on the matching-χ^2 of the single muons, on the other hand, uses the information coming from both the PC and VT reconstructed tracks, to reject those events in which the matched dimuon is composed by one or both "fakely" matched muons, hence, having a degraded kinematics. The selection which results by requesting the "dimuon-target association", finally, rejects those events in which the selected association criterion cannot be applied: this last selection, hence, rather relies on the event as a whole, than on a particular characteristic of the matched dimuon.

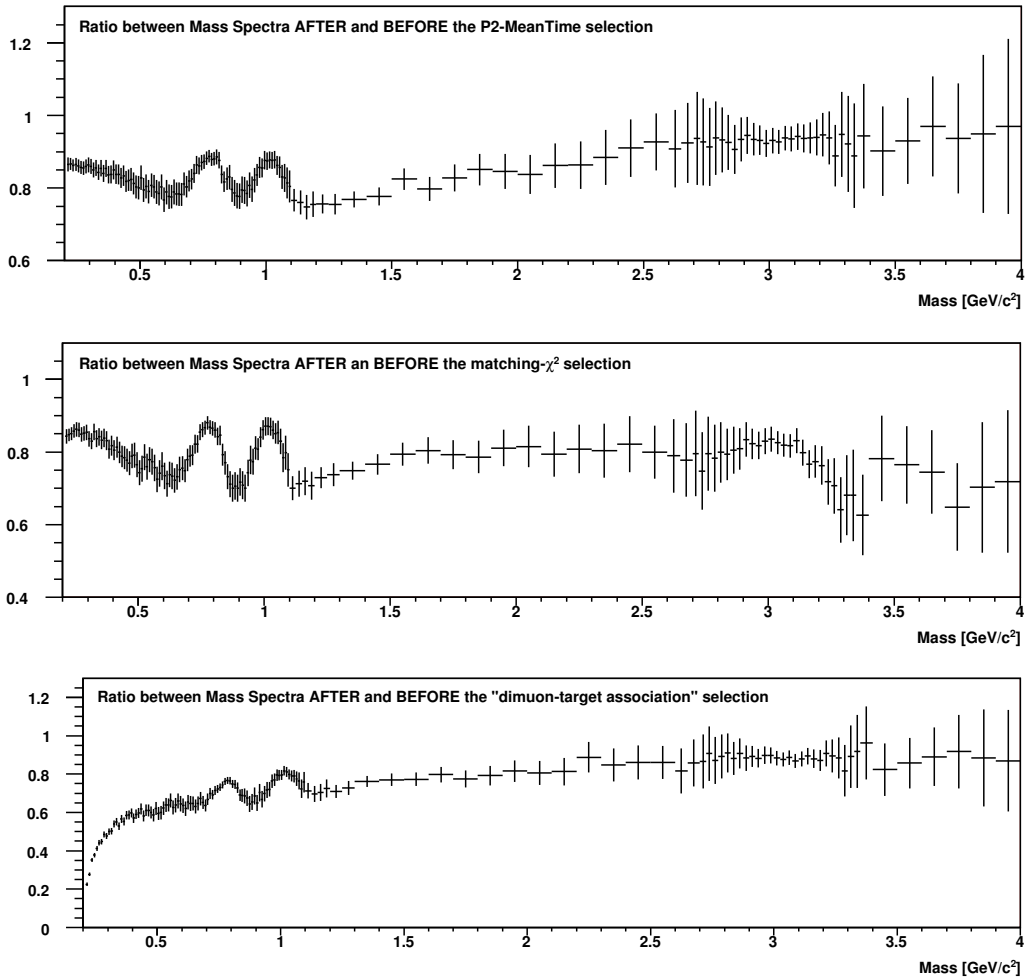

Figure 4.13: *Ratios between the mass spectra after and before the selection cuts described in the text.*

5

Expected Dimuon Sources and Monte Carlo Generation

The dimuon mass spectrum observed in p-A collisions is a rich superposition of various sources, resulting in a continuously falling spectrum, on top of which several distinct resonance structures are observed.

The continuous processes are the Drell–Yan dimuons, which dominate at large dimuon masses (i.e. above ~ 3.5 GeV/c^2) and the semi-muonic simultaneous decays from two D mesons. This latter dimuon source, whose contribution is strongest at around 0.8 GeV/c^2, is called open charm. The electromagnetic decays of the light pseudoscalar and vector mesons (η, η', ρ, ω and ϕ) are the dominating processes at the lower end of the dimuon mass spectrum, adding to the continuous spectrum via their Dalitz decays and/or giving rise to distinct peaks via their 2-body decays. We call their superposition the "hadronic decay cocktail". At higher masses we see the J/ψ, and the ψ'. The more massive bottomonium states cannot easily be produced at SPS energies, since their cross-sections are very small.

The hadronic decay cocktail was simulated with the NA60 Monte Carlo generator Genesis, the open charm process with Pythia. The present simulation follows the ones outlined in Ref. [Wöh04]; in particular, we have used the same distributions and values of the parameters with the only exception of having generated p_{T} distributions with a T-slope depending on the target's mass number A, see Sec. 5.1.5.

5.1 Light Meson Decays

Mesons consist of a quark and an antiquark. For spin $\frac{1}{2}$ quarks and antiquarks we can form spin triplet states ($\uparrow\uparrow$) with $J_S = 1$ and spin singlet states ($\uparrow\downarrow$) with

$J_S = 0$. Fermions and antifermions have intrinsic opposite parity so that the $f\bar{f}$ pair carries parity $P = -1$. If they have orbital angular momentum, L, their parity is given by $P_{f\bar{f}} = (-1)^{L+1}$. Thus, the $J_S = 0$ states in the ground state $L = 0$ have the quantum numbers $J^P = 0^-$ and are called pseudoscalar mesons, while the $J_S = 1$ states with $L = 0$ have $J^P = 1^-$ and are called vector mesons.

As long as the first three quark flavours (u, d, s) are concerned, we expect pseudoscalar and vector meson families containing $3^2 = 9$ states. The pseudoscalar states contain an iso-vector triplet, namely the three pions, $\pi^+ = u\bar{d}$, $\pi^0 = 1/\sqrt{2} = (u\bar{u} - d\bar{d})$), $\pi^- = \bar{u}d$, and two iso-doublets, the $K^+ = u\bar{s}$, $K^0 = d\bar{s}$, $K^- = \bar{u}s$ and the $\bar{K}^0(\bar{d}s)$. The last two members of the pseudoscalar meson family are the η, η' mesons, whose actual states appear to be the following linear combinations

$$\eta = \Big(\frac{\cos\theta_{\rm P}}{\sqrt{6}} - \frac{\sin\theta_{\rm P}}{\sqrt{3}}\Big)u\bar{u} + \Big(\frac{\cos\theta_{\rm P}}{\sqrt{6}} - \frac{\sin\theta_{\rm P}}{\sqrt{3}}\Big)d\bar{d} - \Big(\frac{\cos\theta_{\rm P}}{\sqrt{6}/2} + \frac{\sin\theta_{\rm P}}{\sqrt{3}}\Big)s\bar{s}\ , \qquad (5.1)$$

$$\eta' = \Big(\frac{\sin\theta_{\rm P}}{\sqrt{6}} + \frac{\cos\theta_{\rm P}}{\sqrt{3}}\Big)u\bar{u} + \Big(\frac{\sin\theta_{\rm P}}{\sqrt{6}} + \frac{\cos\theta_{\rm P}}{\sqrt{3}}\Big)d\bar{d} - \Big(\frac{\sin\theta_{\rm P}}{\sqrt{6}/2} - \frac{\cos\theta_{\rm P}}{\sqrt{3}}\Big)s\bar{s}\ . \qquad (5.2)$$

The pseudoscalar mixing angle, $\theta_{\rm P}$, is thought to be $\approx -10°$, with a large uncertainty; this is compatible with the mixing $\eta = 1/\sqrt{6}\,(u\bar{u} + d\bar{d} - 2s\bar{s})$ and $\eta' = 1/\sqrt{3}\,(u\bar{u} + d\bar{d} + s\bar{s})$, which would decompose the pseudoscalar nonet into an $SU(3)$ octet and an $SU(3)$ singlet.

The (quark) structure of the vector meson states is similar to the one of the pseudoscalars. The $J_S = 1$ analog of the pions are the ρ's with the same quark contents, while the vector K^*'s mesons correspond to the pseudoscalar K's. The vector counterpart of the η and η' are the ϕ and the ω, respectively; the observed ϕ and ω states are again mixtures of the pure states $u\bar{u}$, $d\bar{d}$ and $u\bar{u}$, but the measured angle $\theta_{\rm V} \approx 35°$ is much larger than $\theta_{\rm P}$ and is compatible with the ideal mixing angle for which the ϕ becomes a pure $s\bar{s}$ state:

$$\omega = \frac{1}{\sqrt{2}}(u\bar{u} + d\bar{d})\ , \qquad \phi = s\bar{s}\ . \qquad (5.3)$$

By contrast to the pseudoscalar case, hence, neither the ω nor the ϕ is an $SU(3)$ singlet.

The properties of the pseudoscalar and vector mesons which contribute significantly to the dimuon mass spectrum, either through a decay into two muons or via a Dalitz decay, are summarised in Table 5.1.

5.1.1 The Pseudoscalar Mesons, η and η'

Figure 5.1 shows the Dalitz and 2-body decays of the η and the η' pseudoscalar mesons. The (single) Dalitz decay (diagram on the left) is a 2γ decay, in which

Particle	Mass [MeV/c^2]	Γ [MeV/c^2]	J^{PC}	Quark Content
η	547.51 ± 0.18	$(1.30 \pm 0.07) \cdot 10^{-3}$	0^{-+}	$\frac{1}{\sqrt{6}}(u\bar{u} + d\bar{d} - 2s\bar{s})$
ρ	775.5 ± 0.4	149.4 ± 1.0	1^{--}	$\frac{1}{\sqrt{2}}(u\bar{u} - d\bar{d})$
ω	782.65 ± 0.12	8.49 ± 0.08	1^{--}	$\frac{1}{\sqrt{2}}(u\bar{u} + d\bar{d})$
η'	957.78 ± 0.14	0.203 ± 0.016	0^{-+}	$\frac{1}{\sqrt{3}}(u\bar{u} + d\bar{d} + s\bar{s})$
ϕ	1019.460 ± 0.019	4.26 ± 0.05	1^{--}	$s\bar{s}$

Table 5.1: *Properties of the light pseudoscalar and vector mesons contributing to the dimuon mass spectrum, values taken from Ref. [PDG06].*

one of the photons is virtual and converts into a lepton pair, $PS \to \gamma^*\gamma \to \mu^+\mu^-\gamma$. There is also a double Dalitz decay (central diagram) in which both γ's are virtual photons and convert into a lepton pair, but with a much smaller branching ratio. The decay of the η into two muons (diagram on the right) is a 4^{th} order electromagnetic process, where the μ^+ coming from one γ^* and the μ^- coming from the other γ^* are contracted.

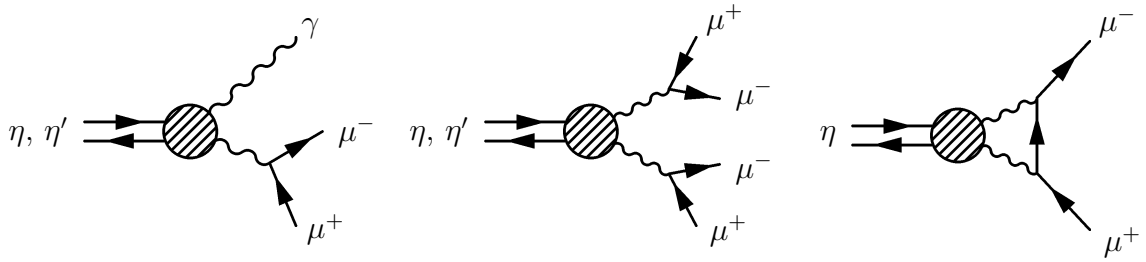

Figure 5.1: *Single Dalitz, Double Dalitz and two body decays of the pseudoscalar mesons η and η'.*

The branching ratio into two muons has a lower limit [Lan85] given by the radiative decay channel,

$$BR(\text{PS} \to l^+l^-) \geq BR(\text{PS} \to \gamma\gamma) \cdot 2\alpha^2 \Big(\frac{m_l}{m_{\text{PS}}}\Big)^2 \sqrt{1 - 4\Big(\frac{m_l}{m_{\text{PS}}}\Big)^2} \quad . \tag{5.4}$$

From this equation we can see that the electronic branching ratio is suppressed with respect to the muonic one, by the ratio $(m_e/m_\mu)^2$. For the η the following lower limits were deduced [Lan85]:

$$\begin{aligned} BR(\eta \to \mu^+\mu^-) &\geq 4.0 \cdot 10^{-6} \quad , \\ BR(\eta \to e^+e^-) &\geq 1.7 \cdot 10^{-9} \quad . \end{aligned}$$

Indeed, only the muonic branching ratio is measured at present. Its value, taken from Ref. [PDG06], is $BR(\eta \to \mu^+\mu^-) = (5.8 \pm 0.8) \cdot 10^{-6}$. For the η' 2-body leptonic decay channels there are also such theoretical lower limits. Experimentally, however, not even an upper limit is published in the PDG tables so that we can safely neglect its contribution to the dimuon mass spectrum (as one can see from Equation 5.4, the branching ratio for the 2-body decay of the η' is suppressed with respect to the one of the η, because of the factors m_ℓ/m_{PS}).

The (single) Dalitz decay channel of the η' is comparable to the one of the η, so that we must consider this process. Unfortunately, the production cross-section of the η' was never measured. In Ref. [Dia80] the η'/π^0 ratio is given for high p_{T}. Based on this measurement, in Ref. [Vee93] the η' cross-section was extracted by fitting the observed p_{T} spectra of the η' and of the π^0 with the Bourquin-Gaillard parameterisation [Bou76]. A similar analysis was performed for the η, from which the ratio $\eta'/\eta = 1/3$ was extracted (with rather large uncertainties). In Ref. [CERES] a value of $\eta'/\eta < 0.2$ was found at 95 % confidence level. Following the analysis performed in Ref. [Wöh04], we have assumed $\eta'/\eta = 0.15$.

5.1.2 The Light Vector Mesons: ρ, ω and ϕ

The vector mesons ρ, ω and ϕ mainly contribute to the dimuon mass spectrum via their $\mu^+\mu^-$ decay mode. The electromagnetic decay of the vector mesons ρ, ω and ϕ into two muons proceeds via a virtual photon, $V \to \gamma^* \to \mu^+\mu^-$ (they posseses the same J^{PC} quantum numbers as the photon). The ω posseses, furthermore, a Dalitz decay mode, in which the lepton pair is accompanied by a π^0, $\omega \to \gamma^*\pi^0 \to \mu^+\mu^-\pi^0$, see Figure 5.2.

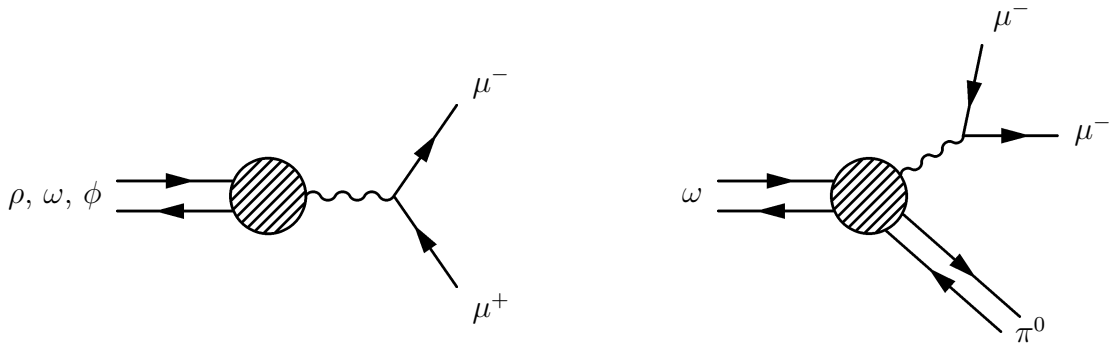

Figure 5.2: *Dimuonic decay of the vector mesons ρ, ω and ϕ (left) and the ω Dalitz decay (right).*

5.1.3 The Vector Dominance Model

The Vector Dominance Model (VDM) is a phenomenological model which describes the interactions between hadrons and photons. The main idea is that a virtual

photon can interact with a hadron only after a transition into a virtual vector meson state. This is possible since vector mesons (like the ρ, ω and the ϕ) have the same quantum numbers as the photon, $J^P = 1^-$. This mechanism works especially well when the transfered momentum squared, q^2, approaches the squared mass of an observed vector meson. The VDM model provides a framework to describe e.g. the ρ resonance and the form factors of the η, η' and ω Dalitz decays. This realisation of a virtual intermediate particle results in a strong enhancement of the form factor.

5.1.4 Branching Ratios

Table 5.2 summarises the processes contributing to the hadronic cocktail and gives their branching ratios, taken from the Particle Data Group tables [PDG06].

	Particle	Decay Mode	Branching Ratio
Dalitz	η	$\mu^+\mu^-\gamma$	$(3.1 \pm 0.4) \cdot 10^{-4}$
	ω	$\mu^+\mu^-\pi^0$	$(9.6 \pm 2.3) \cdot 10^{-5}$
	η'	$\mu^+\mu^-\gamma$	$(1.04 \pm 0.26) \cdot 10^{-4}$
2-body	η	$\mu^+\mu^-$	$(5.8 \pm 0.8) \cdot 10^{-6}$
	ρ	$\mu^+\mu^-$	$(4.55 \pm 0.28) \cdot 10^{-5}$
	ω	$\mu^+\mu^-$	$(7.18 \pm 0.12) \cdot 10^{-5}$
	ϕ	$\mu^+\mu^-$	$(2.86 \pm 0.19) \cdot 10^{-4}$

Table 5.2: *Processes included in the hadronic decay cocktail and the branching ratios considered in our study.*

Note that we used the electronic branching ratio for the ω 2-body decay, since it is known with much better accuracy than the muonic value. We have done this assuming lepton universality, which states that the electro-weak interaction couples to all leptons with the same strength. Indeed, the electronic and muonic branching ratios, listed in the PDG tables, agree within their error bars, $BR(\omega \to e^+e^-) = (7.18 \pm 0.12) \cdot 10^{-5}$, $BR(\omega \to \mu^+\mu^-) = (9.0 \pm 3.1) \cdot 10^{-5}$.

5.1.5 Transverse Momentum and Rapidity Distributions

The p_{T} distributions for the light mesons were generated according to the distribution

$$\frac{1}{p_{\mathrm{T}}}\frac{\mathrm{d}N}{\mathrm{d}p_{\mathrm{T}}} = \frac{1}{m_{\mathrm{T}}}\frac{\mathrm{d}N}{\mathrm{d}m_{\mathrm{T}}} = m_{\mathrm{T}} K_1\left(\frac{m_{\mathrm{T}}}{T}\right) \ , \tag{5.5}$$

where $K_1(x)$ is the modified Bessel function of the second kind of order 1. We used one T value for all particles, but increasing with the mass number A:

$$T(\mathrm{A}) = T_0 + k \cdot \mathrm{A} \ ;$$

the parameters k and T_0 were deduced from a linear fit of the values needed to describe the p_T distributions observed by NA60 in the 2002 p-A run [Wöh04] for the ω:

$$\begin{aligned} T &= 170 \text{ MeV} \quad (p\text{-Be}) \\ T &= 185 \text{ MeV} \quad (p\text{-In}) \\ T &= 200 \text{ MeV} \quad (p\text{-Pb}) \end{aligned}$$

We are, thereby, neglecting a possible dependence of the inverse slope parameter T on the particle's mass.

The rapidity distributions in the Center of Mass frame (CM frame) were generated according to the expression

$$\frac{\mathrm{d}N}{\mathrm{d}y} \propto \frac{1}{\cosh^2(ay)} \ , \tag{5.6}$$

similar to a Gaussian of $\sigma = 0.75/a$. This simple parameterisation has been used by several experiments, since it describes resasonably well existing measurements.

The width of the pion rapidity distribution was estimated using Landau's expression $\sqrt{\log \gamma_\mathrm{proj}}$. The width of the rapidity distribution for heavier mesons is decreased proportionally to the maximum rapidity with which such a meson can be produced in the CM frame for a given $\sqrt{s}$: $\sigma_\mathrm{part} = \sigma_\pi \cdot y^\mathrm{cm}_\mathrm{max}(m_\mathrm{part})/y^\mathrm{cm}_\mathrm{max}(m_\pi)$, with $y^\mathrm{cm}_\mathrm{max} = \log(\sqrt{s}/m_\mathrm{part})$. Table 5.3 summarises the width parameters of the rapidity distributions for the particles relevant for the Genesis event generator, including the π^0 and the J/ψ, at $E_\mathrm{lab} = 400$ GeV.

5.1.6 Mass Line Shapes

For the mass line shapes of the narrow resonances η, ω and ϕ, we have used a modified relativistic Breit-Wigner parametrisation, first proposed by G.J. Gounaris and J.J. Sakurai [Gou68], with widths and masses taken fom the PDG tables [PDG06].

The ρ predominantly decays in the two-pion channel, $BR(\rho \to \pi^+\pi^-) \approx 100\,\%$. Particles decaying via the strong interaction are characterised by lifetimes of the order of $\tau \sim 10^{-22} - 10^{-24}$ s, resulting in decay widths, $\Gamma \equiv 1/\tau$, of around 100 MeV. The ρ, hence, is a "broad" resonance with a decay width of ~ 150 MeV. Due to its broadness, the shape of the ρ is highly influenced by phase space effects and by the production mechanism. The corresponding constant decay width Γ_ρ in the

Particle	Mass [GeV/c^2]	σ_y	a_y
π^0	0.135	1.84	0.41
η	0.548	1.35	0.56
ρ	0.776	1.23	0.61
ω	0.783	1.23	0.61
η'	0.958	1.16	0.65
ϕ	1.019	1.14	0.66
J/ψ	3.097	0.75	1.00

Table 5.3: *Parameters of the rapidity distributions of particles with different masses, for collisions with a beam energy of $E_{\mathrm{lab}} = 400$ GeV.*

Breit-Wigner expression, which describes the resonance, has to be replaced by a mass dependent width, $\Gamma_\rho(M)$. The rate can be calculated within the framework of the Vector Dominance Model; a detailed calculation can be found in Ref. [Genesis].

The lepton pair mass distribution in Dalitz decays involving a photon, was derived by N. Kroll and W. Wada [Kro55]. The measured dimuon mass spectrum for the Dalitz conversion decays deviates from the theoretical prediction by the so-called electromagnetic transition form factors, which can be also calculated in the frame of the Vector Dominance Model. Ref. [Lan85] gives an introduction to this topic and shows a comprehensive compilation of the measurements on the transition form factors available; we have used a parametrisation of the results from the Lepton-G experiments, as was previously done in Ref. [Wöh04].

5.1.7 Distribution of the Decay Angles

The kinematics of each resonance is determined by its 4-momentum, which in turn can be expressed in terms of the particle's mass, its rapidity, p_{T} and azimuthal angle.

The kinematics of the muon pair needs further specifications. Regarding the 2-body decays, in principle, we need to know the 4-momentum of each muon, that is, 8 quantities; actually, we have 4 constraints coming from the conservation of 4-momentum (assuming that the parent particle's kinematic is fixed), and further two contraints since we know the mass of the particles produced in the decay. We are left with two degrees of freedom, given by the polar and azimuthal decay angles of the positive muon (the polar angle is measured with respect to the beam axis). Both the azimuthal angles of the parent particle and the positive muon have a flat distribution over 2π, and they are generated isotropically for all decay modes. The distribution of the polar decay angle in the CM frame was chosen to be flat, too.

The Dalitz decays differ from the 2-body ones, since the virtual photon from

which the muon pair originates does not share the kinematics of the parent particle. The kinematics of the virtual photon, hence, has to be calculated simulating the intermediate step corresponding to the $\gamma\gamma^*$ decay of the parent particle. Regarding the polar decay angle distribution for the positive muon, with respect to the beam axis, a $1+\cos^2\theta$ distribution was chosen in case of the pseudo-scalar η and η', where the third partner is a (real) photon; on the contrary, for the ω Dalitz − where the third partner is a π^0 − we have generated a uniform distribution for the polar angle.

The polar decay angles are *generated* in the rest frame of the decaying particle, i.e. in the meson's rest frame in case of the 2-body decays, or in the rest frame of the virtual photon in the general case including both 2-body and Dalitz decays. When re-calculating the polar decay angle from the two reconstruced muons, we have to specify a certain frame in which the polar angle should be given, since it is not Lorentz invariant (note that this is not the case of the *azimuthal* decay angle). One of the possible frames is the so-called Collins-Soper frame, such that the Collins-Soper (polar) angle θ_{CS} is defined in the elementary nucleon-nucleon collision's CM frame as the angle between the positive muon and the beam-axis. It is worth noting that, due to the fact that a given polar angle distribution is generated in the decaying particle's rest frame and the Collins-Soper angle is calculated in the CM frame, the two distributions usually look quite different.

5.2 Open Charm

The continuum of the dimuon mass spectrum between the ϕ and the J/ψ mesons consists of the Drell–Yan process (DY) and of the simultaneous semi-muonic decay of pairs of D mesons; this latter source also gives a not-negligible contribution in the mass region from the threshold to the ϕ. For the present analysis, which does not consider the mass spectrum above the ϕ, the Drell–Yan process can be safely neglected.

D mesons are formed via the creation of a $c\bar{c}$ pair and the subsequent hadronisation (fragmentation) of the charmed quarks, when each of them binds with a u, d or s quark (or antiquark), to form the D mesons. If both charmed hadrons then decay semi-muonicaly, they may contribute to the dimuon mass spectrum, if the two muons are accepted and reconstructed. Since the energy of the muons depends on the decay kinematics, the formed muon pair will have a continuum spectrum of invariant masses.

At leading order, charm production at SPS energies proceeds through gluon fusion in $\sim 80\,\%$ of the cases and through quark-antiquark annihilation in the other $\sim 20\,\%$. The corresponding first order diagrams can be seen in Fig. 5.3.

In Ref. [WöhLou04] an extensive review of measured D meson cross-sections was performed and compared to lowest order calculations performed with Pythia, having varied Pythia's input parameters, like the mass of the c quark, which is not directly accessible to experimental measurements, or the set of parton distribution

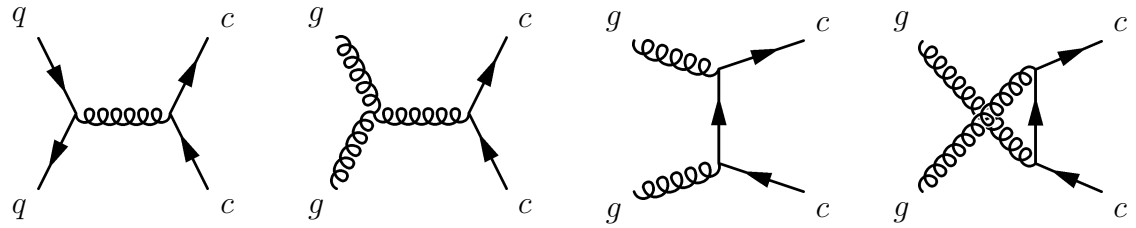

Figure 5.3: *Production mechanisms for $c\bar{c}$ production in first order perturbation theory.*

functions (PDFs). From the measurements of D meson production cross-section, the total $c\bar{c}$ cross-section was plotted as a function of the collision energy; the Pythia calculations were then scaled up in order to describe the existing data. From this procedure, the full phase space $p\,p$ cross-section was derived to be around 20 μb at $E_{\rm lab} = 400$ GeV.

In order to generate "open charm", we have used Pythia with its standard settings, i.e. the mass of charm quark was set to $m_c = 1.5$ GeV and the primordial momentum of the interacting partons was generated according to a Gaussian distribution of variance $k_{\rm T}^2 = 1.0$ (GeV/c)^2. We have generated all final state charmed hadrons with a semi-muonic decay, D^+, D^0, D_s^+, Λ_c^+, Ξ_c^0, Ξ_c^+, Ω_c^0 and their corresponding anti-particles with the relative particle abundances given by Pythia. In order to accelerate the generation process, we have set the corresponding branching ratios into muons to 100 %. In the final event analysis each event contributed then with a weight which is the product of the branching ratios of the two decaying charmed hadrons, thereby correctly accounting for the individual branching ratios, which were taken from the Particle Data Group tables [PDG06].

6

p_{T} Spectra of the ϕ Meson as a Function of Mass Number

In this Chapter we will study the p_{T} spectrum of the ϕ meson, for each of the seven p-A collisional systems for which we have collected data. The procedure we used can be described as follows:

- the dimuon mass spectra of the p-A data samples selected for the final data analysis (see Chapter 4) are used to select events under the ϕ peak, defining a "central mass window"

- the underlying continuum present in the central ϕ mass window is estimated and subtracted using the "side windows" method (see below)

- the raw p_{T} spectra of the resulting samples are corrected by a function taking into account "acceptance $\times$ efficiency", i.e. the overall effect coming from the geometrical acceptance and the reconstruction efficiency for each of the 9 targets

- the statistics corresponding to the 3 individual Be targets is added, and a fit is performed on the corrected p_{T} spectra for each mass number

In the following we will first describe the MC technique used to calculate the diferential acceptances and efficiences for the ϕ. We then discuss the individual steps listed above.

6.1 The Overlay Monte Carlo Simulation Technique

The MC simulation used in the present analysis was performed using a technique called "Overlay-MC"; it consists of superimposing a MC generated muon pair onto real events, in order to realistically simulate the underlying hadronic event together with the detector specific behaviours. The Overlay-MC simulation performed in this work proceeds as follow:

- a *real* event is read, chosen among the reconstructed *data* collected by the experiment in a given run and burst, and one VT vertices is randomly chosen, among those which are reconstructed within the volume of one of the targets[1]

- the vertex where to generate the dimuon is defined, having the same transverse coordinate of the selected real vertex and a re-defined z-coordinate chosen randomly within the target width: the so-defined vertex is then imposed as the origin of the particle to be generated when simulating the relevant processes; note that when simulating the "open charm" contribution, the origin of the muon tracks are given "randomly" by Pythia, based on the decay lengths of the charmed hadrons and their kinematics

- the muon pair produced in each simulation is tracked through the NA60 apparatus, using GEANT. The "hits" left by the MC particles in the various detectors are then put together with the hits stored in the real event from which the MC vertex was deduced: in this way we are simulating a full event without having to generate the full underlying hadronic event

- starting from the ensemble of the MC and real hits, the events in which a muon pair gave rise to a trigger were reconstructed using the same reconstruction settings described in Chapter 3. To make the MC simulation as realistic as possible, the MC tracks leave a signal in a given VT plane with a probability proportional to the plane efficiency estimated from the analysis of the real data. Apart from the planes which were completely switched off (see Chapter 3), in the current simulation we have used a global pixel efficiency of 95 %

It is worth noting that − when putting together the MC and the real hits − we are not considering the real hits in the muon spectrometer, in order to not alter the charged multiplicity observed in the apparatus beyond the hadron absorber. We also exclude the real hits of the VT muons, in order to not alter the average number of tracks attached to the reconstructed VT vertices.

[1] It is worth noting that we do not choose the "best" vertex, i.e. the vertex with most tracks attached and having the smallest χ^2, in order not to bias the procedure to choose reconstructed vertices in large-A targets that have the best acceptance.

For the tracks other than the ones generated with GENESIS, the Overlay-MC technique *automatically* reproduces the effects imposed by the detector, such as the finite acceptance window, the energy loss, and the smearing of the kinematics through multiple scattering or due to the finite resolution of the apparatus.

6.2 Selecting Events from the ϕ Meson

The central mass window on the ϕ peak was defined as $M_\phi - 2\sigma_\phi < M < M_\phi + 2\sigma_\phi$, where both the ϕ pole mass and the width were extracted from a Gaussian fit on the ϕ peak in the target-integrated mass spectrum:

$$M_\phi = (1\,015 \pm 1)\ \mathrm{MeV}/c^2 \qquad \sigma_\phi = (38 \pm 3)\ \mathrm{MeV}/c^2$$

Note that the width decreases for events reconstructed closer to the vertex tracker, hence the quoted value of 38 MeV/c^2 is a weigthed average of the events distributed over all 9 targets. To define a mass window that minimizes the underlying continuum, in particular for events produced in forward targets, we used a window of $\pm 2 \cdot 35$ MeV/c^2 for the central ϕ region. The lateral windows were defined starting just at the right and left sides of the central one, each of them being $2 \cdot 35$ MeV/c^2 wide.

Figure 6.1 shows the reconstructed mass spectrum for each of the nine targets. For each spectrum, the boundaries of the central and side windows are shown; a Gaussian fit was performed in the central mass window, having fixed the mean value to $M_\phi = 1\,015$ MeV/c^2. The resulting widths are reported in Table 6.1, together

Target	$\boldsymbol{\sigma_\phi}$ [MeV/c^2]	Total OS	ϕ Window	Side Windows
Al	46 ± 3	6080	745	219
U	44 ± 3	20930	3357	958
W	40 ± 3	22352	3669	1007
Cu	40 ± 3	17949	2813	758
In	38 ± 3	17800	2757	732
Be1	39 ± 3	5151	715	201
Be2	34 ± 3	4175	574	175
Be3	41 ± 3	3476	453	133
Pb	36 ± 3	16447	1906	490

Table 6.1: *Width of the ϕ peak as resulting by a Gaussian fit on the reconstructed mass spectrum, and number of events present in the whole OS mass spectrum, in the central ϕ window and in the side windows defined in the text.*

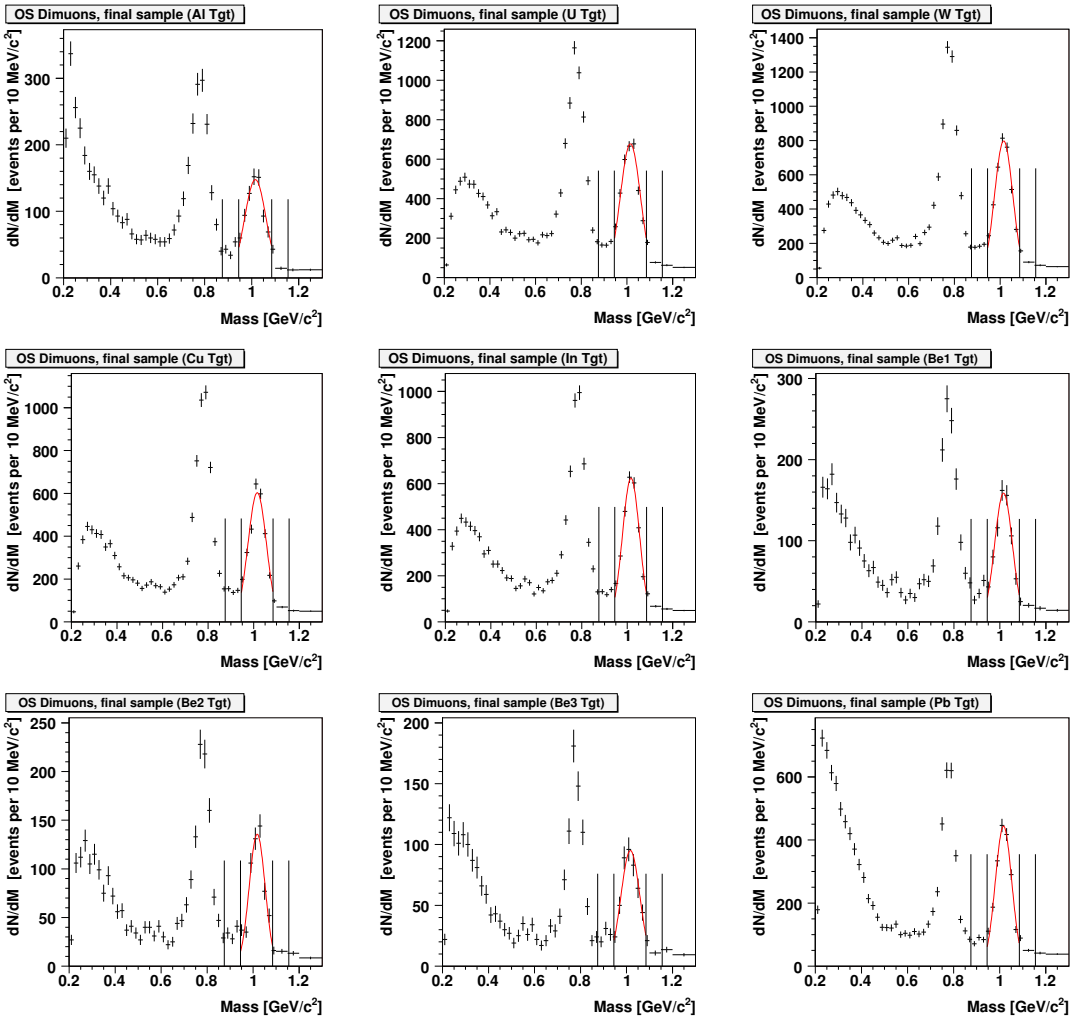

Figure 6.1: *Reconstructed dimuon mass spectra for each of the 9 targets. The boundaries of the central and side windows for the ϕ meson analysis are shown as vertical lines.*

with the number of events present in the whole OS mass spectrum, in the central ϕ window and in the side windows.

The underlying continuum which is present in the central mass window on the ϕ peak is mainly due to two contributions: (i) the so-called "combinatorial background", due to uncorrelated muonic decays of π and K mesons of opposite sign, in which the muons are produced in such a way that they give rise to a dimuon trigger; (ii) the continuum coming from the "open charm" process. It can be shown that, within the mass range covered by the central and side windows, the background shows a linear profile: it ensures that the number of events in the side windows approximately equals the number of events of the continuum in the central window; it can also be assumed that within this mass range the kinematical variables have not significant mass-dependent behaviour: relying on these assumptions, it results that the kinematical distributions of the underlying continuum present in the

central mass window can be estimated considering the corresponding kinematical distributions of the side mass windows.

According to this, we project the p_{T} distribution in the central and side mass windows defined for the ϕ meson, for each of the 9 targets. Then, we subract the individual p_{T} spectra of the sum of the left and right side window from the p_{T} spectrum of the central mass window; in this way, we obtain the ϕ p_{T} spectra.

6.3 Acceptance × Efficiency Correction

6.3.1 Phase Space Window for the ϕ Meson

The p_{T} spectrum resulting from the side window subtraction has to be corrected by the acceptance × efficiency. In order to define the phase space window in which we perform this correction, we evaluate it as a function of rapidity and $\cos\theta_{\mathrm{CS}}$; this study was performed for each target, in the central mass window on the ϕ peak.

Table 6.2 reports the kinematical range, for each target, within which the correction does not vary by more than a factor ~ 10; Figure 6.2 shows the corresponding "acceptance × efficiency" profiles for three targets situated in the upstream, middle and downstream section of the target system (see Chapter 2).

The $\cos\theta_{\mathrm{CS}}$ range can be chosen as $|\cos\theta_{\mathrm{CS}}| < 0.5$ for each target; the position of the rapidity range, however, is target-dependent: in order to have a unique rapidity range for all the targets, at the same time limiting the loss of statistics (see Figure 6.2), we choose to consider the kinematical domain $3.2 < y_{\mathrm{lab}} < 4.2$. In the following, the analysis will be done in the phase space defined by:

$$|M - 1\,015| < 70\ \mathrm{MeV}/c^2 \qquad |\cos\theta_{\mathrm{CS}}| < 0.5 \qquad 3.2 < y_{\mathrm{lab}} < 4.2$$

Target	**Rapidity Range**	**$\cos\theta_{\mathrm{CS}}$ Range**
Al	$3.4 < y_{\mathrm{lab}} < 4.3$	$-0.5 < \cos\theta_{\mathrm{CS}} < 0.5$
U	$3.3 < y_{\mathrm{lab}} < 4.2$	$-0.5 < \cos\theta_{\mathrm{CS}} < 0.5$
W	$3.3 < y_{\mathrm{lab}} < 4.2$	$-0.5 < \cos\theta_{\mathrm{CS}} < 0.5$
Cu	$3.3 < y_{\mathrm{lab}} < 4.2$	$-0.5 < \cos\theta_{\mathrm{CS}} < 0.5$
In	$3.3 < y_{\mathrm{lab}} < 4.1$	$-0.5 < \cos\theta_{\mathrm{CS}} < 0.5$
Be1	$3.3 < y_{\mathrm{lab}} < 4.1$	$-0.5 < \cos\theta_{\mathrm{CS}} < 0.5$
Be2	$3.2 < y_{\mathrm{lab}} < 4.1$	$-0.5 < \cos\theta_{\mathrm{CS}} < 0.5$
Be3	$3.2 < y_{\mathrm{lab}} < 4.0$	$-0.5 < \cos\theta_{\mathrm{CS}} < 0.5$
Pb	$3.1 < y_{\mathrm{lab}} < 4.0$	$-0.5 < \cos\theta_{\mathrm{CS}} < 0.5$

Table 6.2: *Kinematical range ensuring the "acceptance × efficiency" correction does not vary by more than a factor ~ 10.*

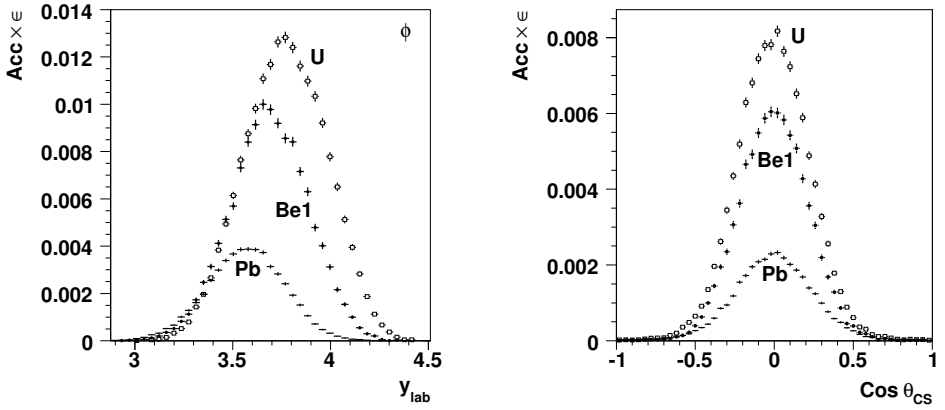

Figure 6.2: *"Acceptance × efficiency" as a function of rapidity and* $\cos\theta_{\mathrm{CS}}$ *for three targets standing in the upstream, middle and downstream section of the target system.*

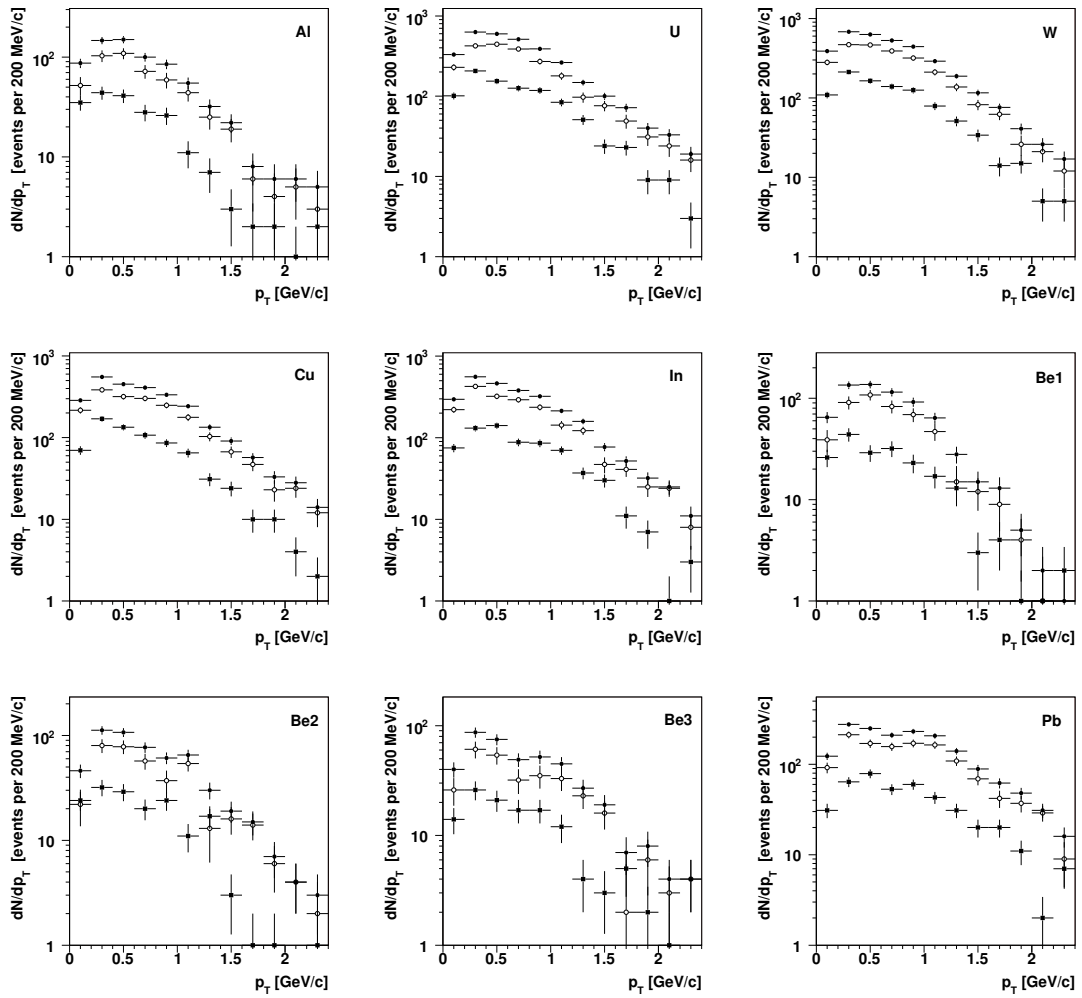

Figure 6.3: *Raw* p_{T} *spectra for the* ϕ *before (filled circles) and after (open circles) the side window subtraction, and for the events in the side windows (black squares) for each of the 9 targets, projected within the phase space window.*

Figure 6.3 shows the p_{T} spectra of the ϕ (after the side window sutraction) and of the side window events, projected in the phase space window defined above. Applying the rapidity and $\cos\theta_{\mathrm{CS}}$ acceptance cuts we are loosing $\sim 5\,\%$ of the statistics in the ϕ mass window, while significantly loosing events at low masses (integrated in mass we loose $\sim 20\,\%$). This was expected, since the definition of the phase space window was tuned to the ϕ's kinematics.

6.3.2 p_{T} Correction

In order to correct the raw p_{T} spectra obtained after the side window subtraction, we evaluated the acceptance × efficiency as a function of p_{T}, within the phase space just defined. The corresponding correction profiles are shown in Figure 6.4; for $p_{\mathrm{T}} \gtrsim 2$ GeV/c we do not yet have enough MC statistics to perform a reliable

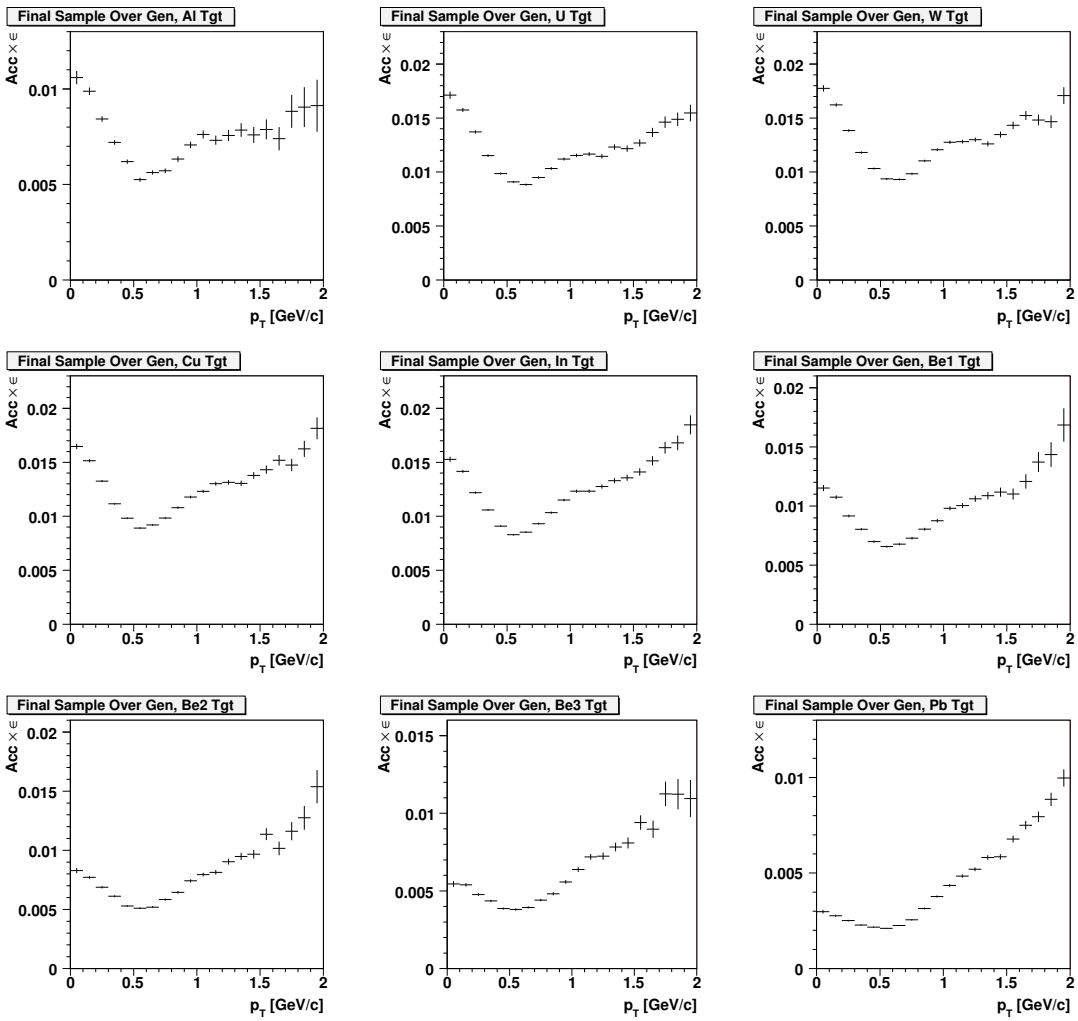

Figure 6.4: *"Acceptance × efficiency" for each target as a function of p_{T}, within the phase space defined in the text.*

correction for all targets.

6.3.3 Fitting the Corrected p_{T} Spectra

Applying the "acceptance × efficiency" correction to the p_{T} spectrum of the ϕ, target by target, we obtain a "corrected" p_{T} spectrum for each target. The p_{T} spectra corresponding to the three beryllium targets can then be put together, in order to increase the corresponding statistics. In this way, we are left with seven p_{T} spectra, corresponding to p-Be, p-Al, p-Cu, p-In, p-W, p-Pb and p-U collision systems, respectively.

These spectra can be fitted using various expressions; following common practice, we started performing the fit using two different functions:

$$\frac{\mathrm{d}N}{\mathrm{d}p_{\mathrm{T}}} \propto p_{\mathrm{T}}\, m_{\mathrm{T}}\, K_1\left(\frac{m_{\mathrm{T}}}{T_{\mathrm{Bessel}}}\right) \qquad \text{and} \qquad \frac{\mathrm{d}N}{\mathrm{d}p_{\mathrm{T}}} \propto p_{\mathrm{T}}\, \exp\left(-\frac{m_{\mathrm{T}}}{T_{\mathrm{exp}}}\right)$$

where $K_1(x)$ is the modified Bessel function of the second kind of order 1, and T is a parameter which only in the case of the exponential function represents the temperature of the system we are probing. Using either the exponential or the Bessel function, the quality of the fit did not change significantly. In Table 6.3 the results of the fit are summarised: for each p-A system two T-values are reported, corresponding to the Bessel and exponential fit functions, respectively. The obtained values are represented in Figure 6.5: the two sets of values follow approximately the same trend, the T_{Bessel} set being $11 - 14$ MeV below the T_{exp} one.

Due to the noticeable statistical errors and fluctuations, a rising trend of T as a function of A is only hardly observable. Extending the fit range beyond 1.5 GeV/c,

p-A	T_{Bessel} [MeV]	T_{exp} [MeV]
p-Be	183 ± 7	195 ± 7
p-Al	192 ± 11	205 ± 13
p-Cu	192 ± 5	205 ± 6
p-In	177 ± 5	188 ± 6
p-W	193 ± 5	207 ± 5
p-Pb	193 ± 6	207 ± 7
p-U	192 ± 5	206 ± 6

Table 6.3: *T-slope parameter resulting from the fit of the corrected p_{T} spectra for each p-A system.*

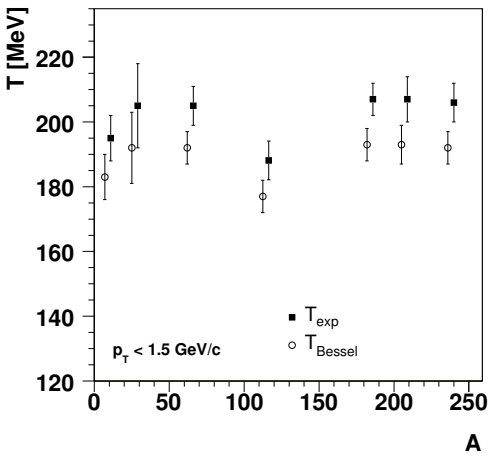

Figure 6.5: *T-slope param. as a function of the mass number A. The two sets of values are sligthly horizontally shifted one from each other for clearness.*

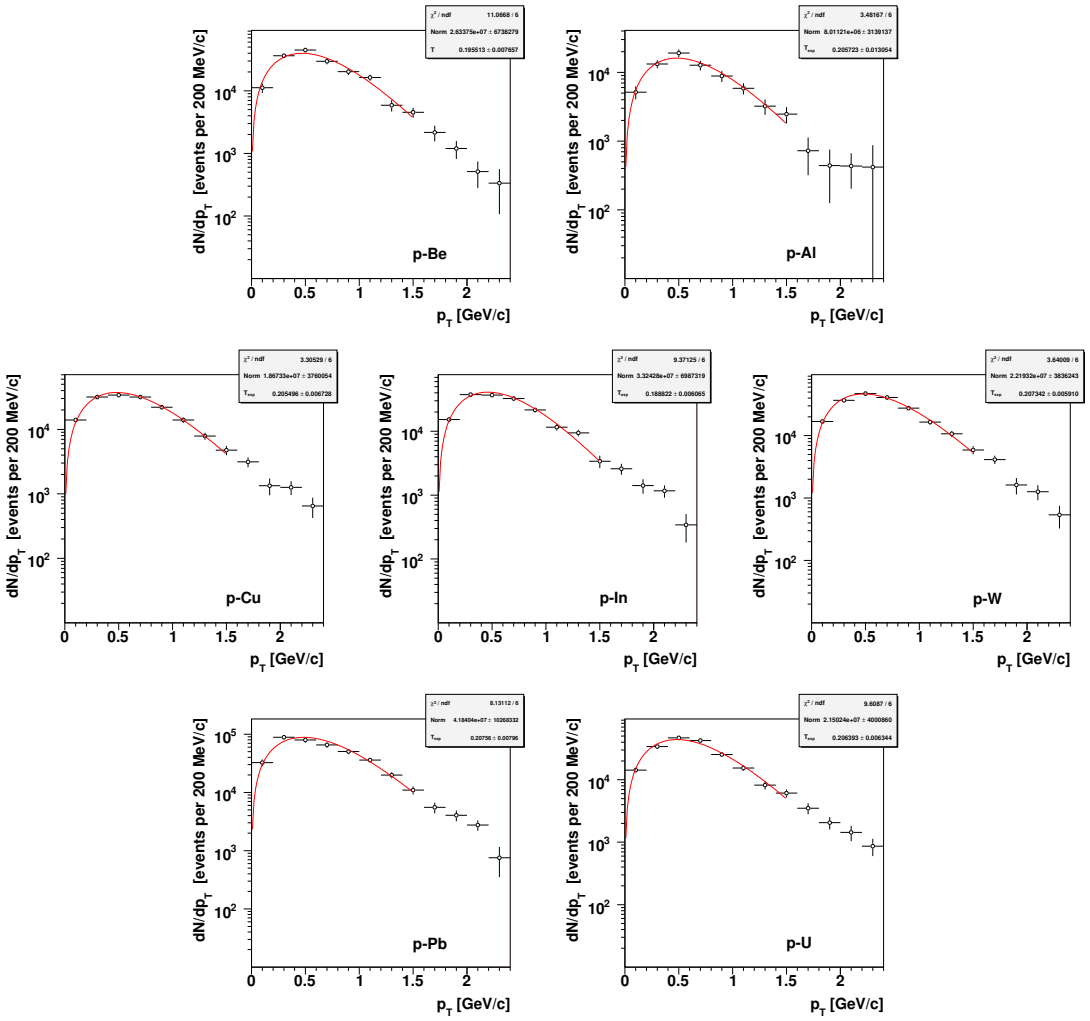

Figure 6.6: p_{T} *spectra for the* ϕ *meson, corrected by the "acceptance* $\times$ *efficiency" effects, fitted with an exponential parametrisation.*

we noted that both the exponential and Bessel parametrisations do not properly describe the data anymore. Hence, in order to profit from the whole $p_{\mathrm{T}} \lesssim 2$ GeV/c range where we have data and the MC correction is reasonably accurate, we considered the following power-law parametrisation:

$$\frac{\mathrm{d}N}{\mathrm{d}p_{\mathrm{T}}^2} = C\, p_{\mathrm{T}} \left(1 + \frac{p_{\mathrm{T}}^2}{p_0^2}\right)^{-\beta} . \tag{6.1}$$

Furthermore, in order to directly compare our results with those of other experiments, we performed the analysis of the p_{T} spectra of the ϕ as a function of p_{T}^2,

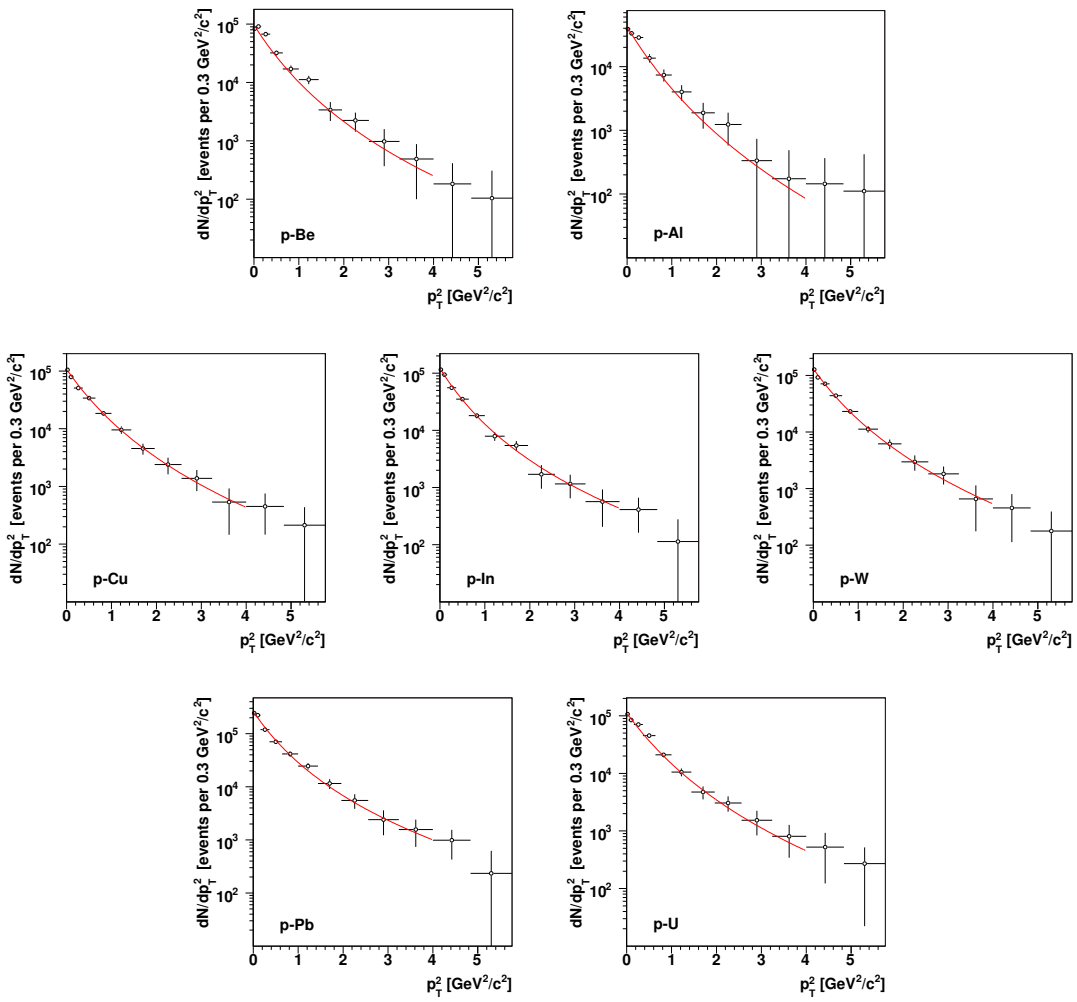

Figure 6.7: p_{T}^2 *spectra for the* ϕ *meson, corrected by the "acceptance* $\times$ *efficiency" effects, fitted with the power-law parametrisation (6.2).*

instead of p_{T}. The power-law parametrisation (6.1) translates to:

$$\frac{\mathrm{d}N}{\mathrm{d}p_{\mathrm{T}}^2} = C\left(1+\frac{p_{\mathrm{T}}^2}{p_0^2}\right)^{-\beta}, \tag{6.2}$$

where C, p_0 and β are free parameters. The p_{T}^2 spectra, properly corrected for the acceptance $\times$ efficiency, are shown in Figure 6.7. As can be seen, the power-law parametrisation is in good agreement with the data within the whole fit range $p_{\mathrm{T}}^2 < 4$ GeV$^2/c^2$. The values of the parameters β and p_0^2 are reported in Table 6.4.

We also calculated the average p_{T}^2 as a function of the mass number A: the values are reported in Table 6.5 and plotted in Figure 6.8. The $\langle p_{\mathrm{T}}^2 \rangle$ shows a rising trend as a function of A, although also here we will learn more once we add the statistics

p-A	β	p_0^2 [GeV$^2/c^2$]
p-Be	5.0 ± 0.8	1.8 ± 0.4
p-Al	6.1 ± 1.9	2.3 ± 1.0
p-Cu	4.7 ± 0.6	1.8 ± 0.3
p-In	4.2 ± 0.5	1.4 ± 0.2
p-W	4.7 ± 0.5	1.8 ± 0.3
p-Pb	4.2 ± 0.5	1.4 ± 0.3
p-U	5.0 ± 0.6	2.0 ± 0.4

Table 6.4: *β and p_0^2 parameters from the fit of the corrected p_{T}^2 spectra for each p-A system.*

from the remaining period od data taking.

As a final remark, we would like to underline that the errors reported in the p_{T} analysis shown here only account for the statistical errors given by the fits. A systematical study of these preliminary results are currently in progress, also profiting from a larger Monte Carlo statistics allowing for a better evaluated acceptance × efficiency correction.

p-A	$\langle p_{\mathrm{T}}^2 \rangle$ [GeV$^2/c^2$]
p-Be	0.593 ± 0.018
p-Al	0.614 ± 0.029
p-Cu	0.663 ± 0.016
p-In	0.624 ± 0.015
p-W	0.673 ± 0.014
p-Pb	0.645 ± 0.020
p-U	0.680 ± 0.015

Table 6.5: *Mean p_{T}^2 resulting from the corrected p_{T}^2 spectra for each p-A system.*

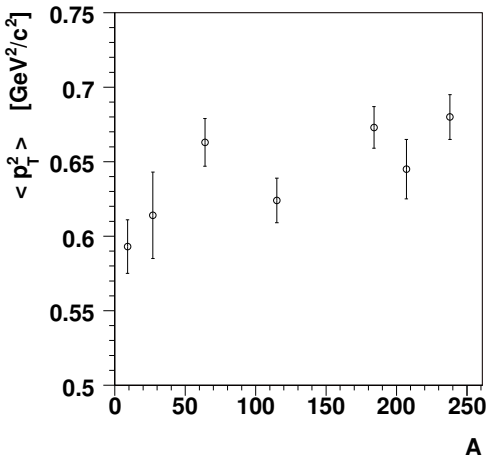

Figure 6.8: *$\langle p_{\mathrm{T}}^2 \rangle$ as a function of the mass number A.*

7

Summary and Conclusions

In this thesis we have studied the p_{T} spectra of the ϕ meson, in interactions of 400 GeV protons with Be, Al, Cu, In, W, Pb and U targets. The analysis is based on a sample of $\sim 12\,000$ ϕ (for all targets) selected among the $\sim 3.8 \times 10^6$ dimuon triggers collected with the NA60 apparatus in three days during the 2004 proton run.

The preliminary results of the study were presented in the previous Chapter. The p_{T} spectra, corrected for the acceptance $\times$ efficiency, calculated with an Overlay-MC simulation, were fitted using various parametrisations. We started fitting the p_{T} spectra both with the exponential and the Bessel parametrisations

$$\frac{\mathrm{d}N}{\mathrm{d}p_{\mathrm{T}}} \propto p_{\mathrm{T}}\, m_{\mathrm{T}}\, K_1\left(\frac{m_{\mathrm{T}}}{T_{\mathrm{Bessel}}}\right) \qquad \text{and} \qquad \frac{\mathrm{d}N}{\mathrm{d}p_{\mathrm{T}}} \propto p_{\mathrm{T}}\, \exp\left(-\frac{m_{\mathrm{T}}}{T_{\mathrm{exp}}}\right) .$$

We observed that the T-values given by the two parametrisations follow approximately the same trend, as expected; the T_{Bessel} set was systematically 11–14 MeV lower than the T_{exp} one. According to Figure 6.5, we did not observe a defined trend of the T-slope parameter, due to the relevant fluctuations and the statistical errors given by the fit.

The exponential parametrisation was also used by NA49 to describe the p_{T} spectra of the ϕ in $p\,p$ and Pb-Pb collisions at 158 GeV, [Afa00]. For proton-proton collisions, for which the data extended up to $p_{\mathrm{T}} \sim 1$ GeV/c, they obtained $T = (169 \pm 17)$ MeV. In order to establish if this value is compatible with our preliminary results, we performed a fit on the p_{T} spectra, being restricted to the same p_{T} range. The results are reported in Table 7.1 and shown in Figure 7.1, together with the T-value found by NA49 in $p\,p$ collisions. As we can see, combining the NA49

T-value with those found in this analysis, a rising trend is suggested as a function of the mass number A, possibly saturating for high A-values.

***p*-A**	$\boldsymbol{T_{\mathrm{exp}}}$ [MeV]
p-Be	181 ± 12
p-Al	192 ± 22
p-Cu	197 ± 13
p-In	178 ± 10
p-W	204 ± 11
p-Pb	181 ± 13
p-U	214 ± 12

Table 7.1: *T-slope paramaters obtained fitting the p_{T} spectra of the ϕ with an exponential parametrisation in the range $p_{\mathrm{T}} < 1$ GeV/c.*

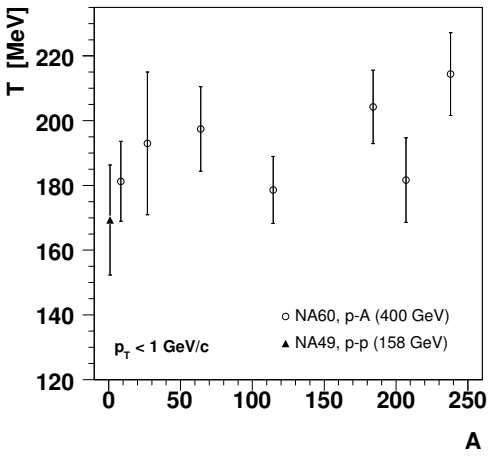

Figure 7.1: *T-slope paramaters obtained fitting the p_{T} spectra of the ϕ with an exponential parametrisation.*

The exponential and Bessel parametrisation do not properly describe the p_{T} spectra for $p_{\mathrm{T}} \gtrsim 1.5$ GeV/c. As suggested in Ref. [Abt07], we then moved to a more accurate description of the data given by the power-law parametisation

$$\frac{\mathrm{d}N}{\mathrm{d}p_{\mathrm{T}}^2} = C \left(1 + \frac{p_{\mathrm{T}}^2}{p_0^2}\right)^{-\beta} . \tag{7.1}$$

The values obtained for the parameters β and p_0 are reported in Table 6.4. As could be seen by looking at the fit shown in Figure 6.7, this function properly describes the p_{T} range up to $p_{\mathrm{T}}^2 = 4$ GeV$^2/c^2$. The HERA-B collaboration used this parametrisation to study the p_{T}^2 spectra of the ϕ in p-C, p-Ti and p-W collisions at 920 GeV [Abt07] measured in the K^+K^- decay channel. Their data were covering an even larger p_{T}^2 range, up to 12 GeV$^2/c^2$, thanks to the larger cross-section available at the higher beam energies. The function (7.1) successfully described the full p_{T}^2 range, as can be seen in Figure 7.2.

Finally, we observed an increase of $\langle p_{\mathrm{T}}^2 \rangle$ as a function of the mass number (see Figure 6.8), that is, the ϕ produced within larger nuclear systems have a larger transverse momentum. Similar observations were made by many other experiments at the SPS and RHIC accelerators. The observed mechanism has become known as the "Cronin Effect" [Klu77], initially observed in 1976 at Fermilab in p-A collisions

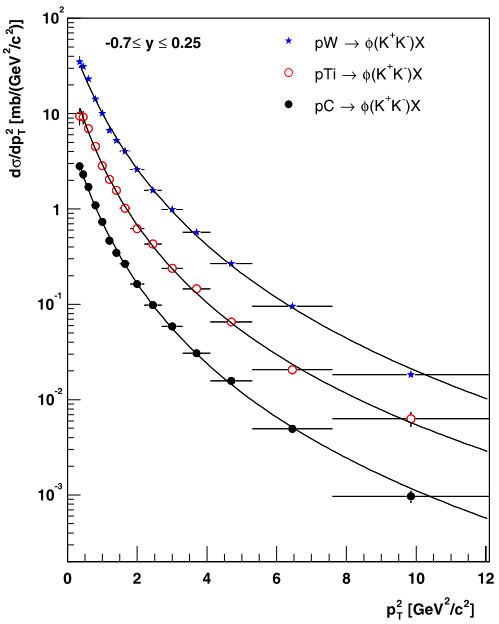

Figure 7.2: p_{T}^2 *spectra for the* ϕ *measured by HERA-B in various p-A collision systems at 920 GeV. Figure taken from [Abt07].*

at energies ranging from 200 up to 400 GeV, for $\pi^{\pm}$, $K^{\pm}$, p and $\bar{p}$ particles. The Cronin Effect is believed to be an initial-state effect in which the partons undergo several elastic collisions while traversing the nuclear matter, *before* they undergo the hard collision in which the final particles are produced. In this picture, it directly follows that the larger the nuclear system, the more visible the effect.

Appendices

A

List of Reconstructed Runs

In this appendix we list the runs which were reconstructed in the data taking period of interest to the present work. As outlined in Chapter 3, 123 runs were pre-selected and reconstructed, out of the 225 collected runs 11580–11804.

The following Table gives the number of reconstructed bursts and events available for each reconstructed run, together with the fraction of events having a dimuon trigger. The ACM/PT7 polarities are reported, corresponding to 4000 A and 900 A currents, respectively. The single bursts and the whole runs excluded from the final analysis are also reported as additional informations.

Run	**Bursts**	**Events**	**% Dimuon**	**ACM/PT7**	**Excluded Bursts**
11598	39	37652	64	+/+	burst 11 discarded
11600	21	18490	64	+/+	burst 16 discarded
11605	27	24406	64	+/+	
11606	5	2451	99	+/+	whole run discarded
11607	14	14268	63	+/+	
11608	7	6539	63	+/+	
11609	155	134763	62	+/+	bursts 20, 126 discarded
11610	10	8686	61	+/+	whole run discarded
11611	27	23896	62	+/+	
11612	66	58678	62	+/+	
11613	10	8983	61	+/+	
11614	44	38766	62	+/+	
11615	44	38396	62	+/+	
11618	11	9467	61	+/+	whole run discarded
11621	10	9069	62	+/+	

Run	Bursts	Events	% Dimuon	ACM/PT7	Excluded Bursts
11629	42	44967	65	+/−	
11630	16	10019	99	+/−	
11633	14	7330	99	+/−	whole run discarded
11635	19	10518	99	+/−	
11636	25	13043	99	+/−	
11637	25	13062	99	+/−	
11639	32	29337	65	+/−	
11640	174	156739	65	+/−	burst 147 discarded
11641	63	56585	65	+/−	
11642	6	5380	65	+/−	
11643	46	40974	65	+/−	
11646	69	37056	61	−/−	
11647	97	51798	61	−/−	burst 13 discarded
11648	26	5369	61	−/−	whole run discarded
11649	80	76055	61	−/−	
11655	117	128312	62	−/−	burst 85 discarded
11656	13	14411	62	−/−	
11657	31	34400	62	−/−	
11658	21	23047	62	−/−	
11659	5	5612	63	−/−	
11660	32	34046	60	−/−	bursts 6–22 discarded
11661	81	85194	59	−/−	whole run discarded
11662	118	124012	60	−/−	burst 83 discarded
11664	10	10840	64	−/+	
11666	34	36610	64	−/+	burst 23 discarded
11667	41	48132	64	−/+	
11668	90	103007	64	−/+	
11669	4	4587	64	−/+	
11671	71	80461	63	−/+	burst 44 discarded
11672	12	14198	64	−/+	
11673	4	4164	65	−/+	
11674	39	41469	64	−/+	
11675	57	44647	63	−/+	
11676	75	60753	63	−/+	whole run discarded
11678	93	75664	63	−/+	
11679	55	44050	63	−/+	
11680	25	20208	63	−/+	
11681	54	43147	63	−/+	
11683	33	29521	53	+/−	
11685	46	35277	62	+/−	
11686	12	9079	62	+/+	bursts 1, 12 discarded
11687	229	174250	62	+/−	bursts 143, 179 discarded
11690	81	58469	60	+/+	whole run discarded
11703	78	69330	61	+/+	
11704	111	83236	59	−/−	burst 92 discarded

Run	Bursts	Events	% Dimuon	ACM/PT7	Excluded Bursts
11705	111	83869	59	−/−	burst 83 discarded
11706	8	5995	61	−/−	
11707	200	147531	59	−/−	
11708	10	7489	60	−/−	
11709	9	6711	59	−/−	
11710	10	10976	41	−/−	burst 10 discarded
11712	16	10665	60	−/−	
11713	45	17821	58	−/−	
11714	7	6106	59	−/−	
11715	3	2132	58	−/−	
11716	62	46721	59	−/−	
11718	39	36310	46	−/−	burst 39 discarded
11732	26	18983	99	−/−	whole run discarded
11736	75	29746	99	−/−	burst 43 discarded
11737	10	11538	49	−/−	
11738	14	6545	94	−/−	
11740	81	52478	72	−/−	
11741	98	65112	72	−/−	
11742	181	120387	72	−/−	
11743	159	105739	72	−/−	
11744	4	2676	72	−/−	
11745	75	50285	74	+/−	burst 75 discarded
11746	144	103716	75	+/−	
11747	49	35644	75	+/−	
11748	31	22371	75	+/−	
11749	23	16669	75	+/−	
11752	52	36079	74	+/−	
11753	9	7177	75	+/−	
11755	53	37062	75	+/−	
11756	80	57248	75	+/−	burst 37 discarded
11758	153	107929	75	+/−	burst 11 discarded
11759	166	114146	75	+/−	burst 80 discarded
11760	18	11878	75	+/−	
11761	29	19115	75	+/−	
11762	176	114627	75	+/−	
11763	13	10022	75	+/−	
11767	126	79821	73	+/+	burst 37 discarded
11769	91	57940	73	+/+	
11770	66	42170	74	+/+	
11771	190	120860	73	+/+	
11772	166	104804	73	+/+	bursts 47, 139 discarded
11774	239	150104	73	+/+	bursts 133, 206, 224 discarded
11775	156	98100	73	+/+	
11783	178	121317	75	+/−	burst 149 discarded
11784	74	50832	75	+/+	burst 74 discarded

Run	Bursts	Events	% Dimuon	ACM/PT7	Excluded Bursts
11786	54	35657	74	+/−	burst 51 discarded
11787	69	45220	73	+/+	
11789	174	113177	73	+/+	
11790	7	4948	76	−/+	
11791	155	111283	75	−/+	
11792	96	68458	75	−/+	
11793	45	34508	76	−/+	
11794	99	72329	75	−/+	
11795	7	5148	76	−/+	
11796	51	34689	74	−/+	
11797	96	69565	75	−/+	
11798	13	9415	75	−/+	
11799	75	54805	75	−/+	burst 35 discarded
11800	156	113548	76	−/+	burst 7 discarded
11801	102	73455	76	−/+	
11802	4	2783	74	−/+	
11803	43	30715	75	−/+	
11804	58	41693	75	−/+	

B

Convolution of a Gaussian with a Step Function

In this appendix we consider the simple case of a beam of particles arriving at a homogeneous material target; we will find how the reconstructed interaction vertices are distributed along the z-direction, assuming to have a tracking device with a Gaussian vertexing resolution of given width.

We are showing that this distribution is expected to be the convolution of the Gaussian representing the vertexing resolution of the tracking device, with a step function representing the z-profile of the material target in which the interactions occur.

We will furthermore show that − under certain conditions − the convolution of a Gaussian with a step function is very close to a simple Gaussian function, as we observed to be the case in the 2004 proton run of NA60, see Figure 4.3.

B.1 The Statement of the Question

We consider to have a beam of particles, directed along z, arriving at a material target placed at a certain z-position; we suppose the target to be composed of a homogeneously distributed material, with a thickness $\Delta z = a$. The particles produced in the interactions, which can only occur within the volume of the target, are tracked by a tracking device, which reconstructs the spatial z-coordinate of the interaction point with a Gaussian resolution of width σ_{VT}.

The target profile along the z direction is represented by a step function $f_{\mathrm{tgt}}(z)$,

which we assume to be centred at $z = \mu$, defined as follow:

$$f_{\text{tgt}}(z) = \begin{cases} 1 & \mu - \frac{a}{2} < z < \mu + \frac{a}{2} \\ 0 & \text{otherwise} \end{cases} \tag{B.1}$$

We now focus our attention on a particular point $z = \xi$; hence, we can say that:

1. the probability that an interaction occurs at $z = \xi$ is given by

$$f(\xi) = \begin{cases} 1/a & \mu - \frac{a}{2} < \xi < \mu + \frac{a}{2} \\ 0 & \text{otherwise} \end{cases} \tag{B.2}$$

   that is, the interaction is allowed to occur only within the volume of the target, with a uniform probability $1/a$

2. the interaction vertex that took place at $z = \xi$ (if any) will be reconstructed at a point along z, according to the following probability distribution:

$$g(z; \xi, \sigma_{\text{VT}}) = \frac{1}{\sigma_{\text{VT}}\sqrt{2\pi}} \exp\left(\frac{(z-\xi)^2}{2\sigma_{\text{VT}}}\right) \tag{B.3}$$

Hence, given a particular point ξ along z, arbitrarily choosen such as $-\infty < \xi < +\infty$, we get the probability $f(\xi) \cdot g(z; \xi, \sigma_{\text{VT}})$ to have a vertex reconstructed in z. To obtain the *total* probability distribution to have a vertex reconstructed in z, we have to integrate over all the values $-\infty < \xi < +\infty$:

$$P(z) = \int_{-\infty}^{\infty} \mathrm{d}\xi \, f(\xi)\, g(z; \xi, \sigma_{\text{VT}}) = \int_{-\infty}^{\infty} \mathrm{d}\xi \, f(\xi)\, g(z - \xi; 0, \sigma_{\text{VT}}) \ , \tag{B.4}$$

that is, the total probability is the convolution of the step function $f(z)$ with the Gaussian function $g(z; 0, \sigma)$.

B.2 Functional Form of $P(z)$ Involving the Error Function

We will now derive an explicit functional form of the distribution $P(z)$; through this section, σ will stand for σ_{VT}. We start substituting (B.2) into (B.4), obtaining:

$$\begin{aligned} P(z) &= \frac{1}{a} \int_{\mu - a/2}^{\mu + a/2} \mathrm{d}\xi \, g(z - \xi; 0, \sigma) = \\ &= \frac{1}{a} \int_{-a/2}^{a/2} \mathrm{d}\xi \, g(z - \xi - \mu; 0, \sigma) = \\ &= \frac{1}{a} \int_{-a/2}^{a/2} \mathrm{d}\xi \, g(\xi + \mu - z; 0, \sigma) = \\ &= \frac{1}{a} \int_{-\infty}^{a/2} \mathrm{d}\xi \, g(\xi + \mu - z; 0, \sigma) - \frac{1}{a} \int_{-\infty}^{-a/2} \mathrm{d}\xi \, g(\xi + \mu - z; 0, \sigma) \ , \end{aligned} \tag{B.5}$$

where the last but one expression makes use of the fact that the Gaussian function is an even function. Performing a change of variables

$$\xi - z = \xi', \qquad \mathrm{d}\xi = \mathrm{d}\xi',$$

we obtain

$$\begin{aligned} P(z) &= \int_{-\infty}^{a/2-z} \mathrm{d}\xi'\, g(\xi'+\mu;0,\sigma) - \int_{-\infty}^{-a/2-z} \mathrm{d}\xi'\, g(\xi'+\mu;0,\sigma) = \\ &= \frac{1}{\sigma\sqrt{2\pi}} \left\{ \int_{-\infty}^{a/2-z} \mathrm{d}\xi' \left[\exp\left(\frac{(\xi'-(-\mu))^2}{2\sigma} \right) \right] - \right. \\ &\qquad \left. \int_{-\infty}^{-a/2-z} \mathrm{d}\xi' \left[\exp\left(\frac{(\xi'-(-\mu))^2}{2\sigma} \right) \right] \right\} . \end{aligned} \tag{B.6}$$

As one can see, in both integrals the integrand function is a Gaussian with mean value $-\mu$; now we use the known result:

$$\frac{1}{\sigma\sqrt{2\pi}} \int_{-\infty}^{x} \mathrm{d}x' \left[\exp\left(\frac{(x'-\bar{x})^2}{2\sigma} \right) \right] = \frac{1}{2} \left[1 + \mathrm{erf}\left(\frac{x-\bar{x}}{\sigma\sqrt{2}} \right) \right], \tag{B.7}$$

where $\mathrm{erf}(x)$ is the so-called error function, defined by:

$$\mathrm{erf}(x) \equiv \frac{2}{\sqrt{\pi}} \int_0^x e^{-t^2} \mathrm{d}t. \tag{B.8}$$

Hence, we obtain:

$$P(z) = \frac{1}{2} \left\{ \left[1 + \mathrm{erf}\left(\frac{\frac{a}{2} - z - (-\mu)}{\sigma\sqrt{2}} \right) \right] - \left[1 + \mathrm{erf}\left(\frac{-\frac{a}{2} - z - (-\mu)}{\sigma\sqrt{2}} \right) \right] \right\},$$

from which, noting that $\mathrm{erf}(x)$ is an odd function, we conclude that:

$$P(z) = \frac{1}{2} \left\{ \mathrm{erf}\left(\frac{z + \frac{a}{2} - \mu}{\sigma\sqrt{2}} \right) - \mathrm{erf}\left(\frac{z - \frac{a}{2} - \mu}{\sigma\sqrt{2}} \right) \right\}. \tag{B.9}$$

This functional form depends on three paramaters, which completely define the problem:

1. the position μ of the target centre
2. the thickness a of the target
3. the resolution σ_{VT} of the tracking device

B.3 Confronting $P(z)$ with a Gaussian

Having now at our disposal an explicit form of the function $P(z)$, representing the expected z-distribution of the vertices reconstructed by the tracking device, we can consider some scenarios using different sets of the paramaters $(\mu, a, \sigma_{\rm VT})$.

We are especially interested in studying the roles of the parameters a and σ, rather than the role of μ which is quite obvious and not so interesting. We may consider, for instance, the cases represented in Figure B.1; in the left panel we use $a = 2.0$ and $\sigma_{\rm VT} = 1.0$, while in the right panel we use $a = 2.0$ and $\sigma_{\rm VT} = 0.2$. As one can see, in the left panel the functon $P(z)$ is very close to a Gaussian (shown by the circles), because the overall profile of the convoluted function is dominated by the Gaussian form describing the vertexing resolution; on the contrary, in the right panel we see that the function $P(z)$ follows the profile of a "smoothed step", the vertexing resolution $\sigma_{\rm VT}$ being now able to resolve the "step" structure of the target.

It can be shown that in order for $P(z)$ to be well approximated by a Gaussian, we must have $\sigma^2_{\rm VT} \gtrsim a^2/12$, rather than $\sigma_{\rm VT} \gtrsim a$; that is, we have to compare *the variances* of the two function we are convoluting. In this regard, a significant confirmation comes from the left panel of Figure B.1, where the variance of the Gaussian approximating the function $P(z)$ is given by

$$\sigma^2_{\rm tot} = \sigma^2_{\rm VT} + \frac{a^2}{12} \,, \tag{B.10}$$

that is, the sum of the variances of the convoluted functions $g(z)$ and $f(z)$.

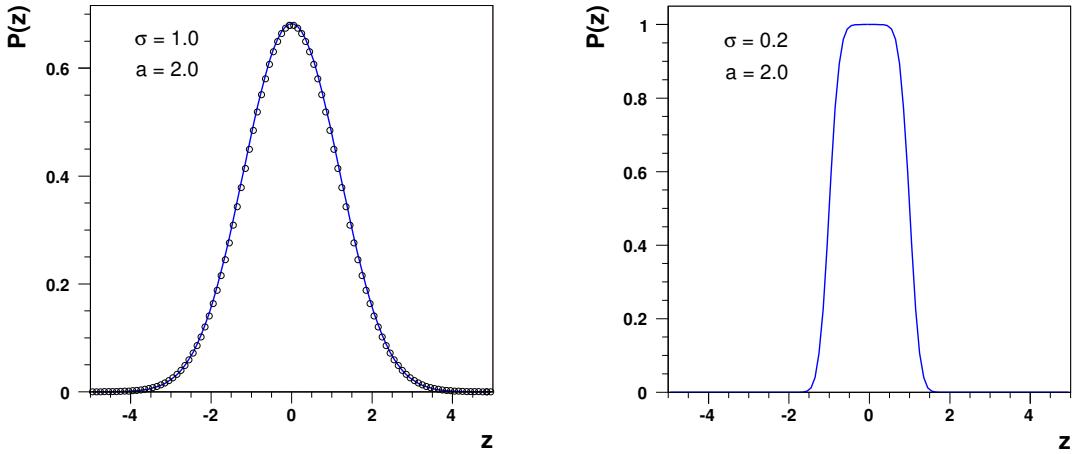

Figure B.1: *Convolution of a step function of width $a = 2.0$ with Gaussian function having $\sigma_{\rm VT} = 1.0$ (left panel) and $\sigma_{\rm VT} = 0.2$ (right panel), respectively. Circles in the left panel show the profile of a Gaussian with $\sigma_{\rm tot}$ given by (B.10).*

It is worth noting that in Figure 4.3 we fitted the observed z-distribution of the reconstructed VT vertices with a superposition of simple Gaussians, instead of using Gaussians convoluted with step functions, still obtaining a good agreement between the data and the resulting fit function. It then implies, according to what we have just seen, that for each target the corresponding vertexing resolution is larger than $a/\sqrt{12}$; the values presented in Table 4.2 are consistent with these lower limits.

B.4 Use of $P(z)$ as a Fit Function

As already pointed out, the functional form of $P(z)$, as given by (B.9), depends on three parameters: the centre-position (μ) and the thickness (a) of the target and the resolution σ_{VT} of the tracking device.

Hence, using the function $P(z)$ to fit the observed z-distribution of the reconstructed vertices, would allow us to extract simultaneously the target's width and centre, as well as the vertexing resolution of the tracking device.

However, while it is always possible to extract the position μ of the target centre, the simultaneous measurement of a and σ_{VT} is not. As previously discussed, in fact, if the tracking system has a vertexing resolution $\sigma \gtrsim a/\sqrt{12}$ the resulting function $P(z)$ is very close to a simple Gaussian with σ_{tot} given by (B.10); in such cases, the same function $P(z)$ can be obtained from all the infinite pairs of values (a, σ_{VT}) satisfying both Equation (B.10) and the condition $\sigma \gtrsim a/\sqrt{12}$.

Hence, if the convoluted function $P(z)$ is close to a Gaussian it is impossible to get simultaneously σ_{VT} *and* a. In this case, one of the two values has to be estimated independently of the fit or fixed to some eucated guess, as was done in our case, outlined in Chapter 4 (see Table 4.2), where we obtained the vertexing resolution σ_{VT} for each target by fixing the targets' widths to the values given by direct measurements.

Bibliography

[Abt07] I. Abt *et al.* (HERA-B Coll.), *K^{*0} and ϕ meson production in oroton-nucleus interactions at $\sqrt{s} = 41.6$ GeV*, Eur. Phys. J. **C50** (2007) 315.

[Afa00] S. V. Afanasiev *et al.* (NA49 Coll.), *Production of ϕ mesons in $p + p$, p+Pb and central Pb-Pb collisions at $E_{\mathrm{beam}} = 158$ A GeV*, Phys. Lett. **B491** (2000) 59.

[Ala01] M. S. Alam *et al.*, *The ATLAS Silicon Pixel Sensors*, Nucl. Instrum. Meth. **A456** (2001) 217.

[And84] L. Anderson *et al.* (NA10 Coll.), *A High-resolution Spectrometer for the Study of High-Mass Muon Pairs Produced by intense Hadron Beams*, Nucl. Instrum. Meth. **A223** (1984) 26.

[Ban04] K. Banicz *et al.*, *Operation and Performance of the NA60 Silicon Pixel Telescope*, Nucl. Instrum. Meth. **A539** (2005) 137.

[BHK04] K. Banicz, J. M. Heuser, M. Keil, *Measurement of radiation dose and particle fluence in the NA60 vertex telescope during the Indium run, October and November 2003*, NA60 Note 2004-2, May 2004.

[Bou76] M. Bourquin and J. M. Gaillard, *A Simple Phenomenological Description of Hadron Production*, Nucl. Phys. **B114** (1976) 334.

[Bro91] G. E. Brown and M. Rho, *Scaling effective Lagrangians in a dense medium*, Phys. Rev. Lett. **66** (1991) 2720.

[CERES] G. Agakichiev *et al.* (CERES Coll.), *Neutral Meson Production in p-Be and p-Au Collisions at 450 GeV Beam Energy*, Eur. Phys. J. **C4** (1998) 249;
G. Agakichiev *et al.* (CERES Coll.), *Low Mass e^+e^- Pair Production in 158 A GeV Pb-Au Collisions at the CERN SPS, Its Dependence on Multiplicity and Transverse Momentum*, Phys. Lett. **B422** (1998) 405;
J. P. Wessels *et al.* (CERES Coll.), *Latest Results from CERES/NA45*, Nucl. Phys. **A715** (2003) 262c.

[Klu77] L. Kluberg *et al.*, *Atomic-Number Dependence of Large-Transverse-Momentum Hadrons Production by Protons*, Phys. Rev. Lett. **38** (1977) 670.

[Dia80] M. Diakonou *et al.*, *Inclusive High-p_T ω and η' Production at the ISR*, Phys. Lett. **B89** (1980) 432.

[Flo04] M. Floris, *Charged Particle Multiplicity in Nucleus-Nucleus Collisions at the CERN-SPS*, PhD Thesis, Università degli Studi di Cagliari, 2004.

[Genesis] S. Damjanovic, A. De Falco and H. K. Wöhri, *The GENESIS $\mu^+\mu^-$ Generator in NA60*, NA60 Internal Note in preparation.

[Gou68] G. J. Gounaris and J. J. Sakurai, *Finite-width Corrections to the Vector-Meson-Dominance Prediction for $\rho \to e^+e^-$*, Phys. Rev. Lett. **21** (1968) 244.

[Kei05] M. Keil, *Update on the Pixel Efficiencies in the Indium Run 2003*, NA60 Collaboration meeting, May 2005.

[Kro55] N. M. Kroll and W. Wada, *Internal Pair Production Associated with the Emission of High-Energy Gamma Rays*, Phys. Rev. **98** (1955) 1935.

[Lan85] L. G. Landsberg, *Electromagnetic Decays of Light Mesons*, Phys. Rep. **128** (1985) 301.

[Lou95] C. Lourenço, *J/ψ, ψ' and dimuon production in p-A and S-U collisions at 200 GeV per nucleon*, PhD Thesis, Instituto Superior Técnico, Lisbon, 1995.

[Lou07] C. Lourenço, *Measuring absolute production cross sections from the proton-nucleus data collected by NA60*, NA60 Note 2007-1, April 2007.

[Mem03] NA60 Collaboration, Memorandum — NA60 Status Report, CERN-SPSC-2003-028, August 2003.

[Mem05] NA60 Collaboration, Memorandum — Report on the 2004 proton run, CERN-SPSC-2005-015, April 2005.

[NA50] M. C. Abreu *et al.* (NA38 and NA50 Coll.), *Dimuon and Charm Production in Nucleus-Nucleus Collisions at the CERN SPS*, Eur. Phys. J. **C14** (2000) 443;
M. C. Abreu *et al.* (NA50 Coll.), *Evidence for Deconfinement of Quarks and Gluons from the J/ψ Suppression Pattern Measured in Pb-Pb Collisions at the CERN SPS*, Phys. Lett. **B477** (2000) 28;
L. Ramello *et al.* (NA50 Coll.), *Results on Leptonic Probes from NA50*, Nucl. Phys. **A715** (2003) 243c;
B. Alessandro *et al.* (NA50 Coll.), *A new measurement of J/psi suppression in Pb-Pb collisions at 158 GeV per nucleon*, Eur. Phys. J. **C39** (2005) 335.

[NA60] R. Arnaldi *et al.* (NA60 Coll.), *First Measurment of the ρ Spectral Function in High-Energy Nuclear Collisions*, Phys. Rev. Lett. **96** (2006);
R. Arnaldi *et al.* (NA60 Coll.), *J/ψ production in Indium-Indium Collisions at 158 GeV/Nucleon*, Phys. Rev. Lett. **99** (2007);
R. Arnaldi *et al.* (NA60 Coll.), *Evidence for radial flow of thermal dileptons in high-energy nuclear collisions*, `arXiv:0711.1816v1` 12 Nov. 2007.

[Oza01] K. Ozawa *et al.*, *Observation of ρ/ω Meson Modification in Nuclear Matter*, Phys. Rev. Lett. **86** (2001) 5019.

[PDG06] W. M. Yao *et al.* (PDG), *Review of Particle Physics*, J. Phys. **G33** (2006) 1.

[Ram07] P. Ramalhete, *Pile-up Estimates for NA60 Detectors*, NA60 Note 2007-2, April 2007.

[Rap00] R. Rapp and J. Wambach, *Chiral Symmetry Restoration and Dileptons in Relativistic Heavy-Ion Collisions*, Adv. Nucl. Phys. **25** (2000) 1.

[Sha04] R. Shahoyan, *Combinatorial Background in the NA60 Muon Spectrometer*, NA60 Note 2004-3, June 2004.

[Sha06] R. Shahoyan (for the NA60 Collaboration), *NA60 Results on charm and intermediate mass dimuons' production in In-In 158 GeV A^{-1} collisions*, J. Phys. **G34** (2007) s1029.

[Vee93] R. J. Veenhof, *Low Mass Muon Pair Production in 450 GeV p-Be Collisions*, PhD Thesis, Universiteit van Amsterdam, 1993.

[Wöh04] H. K. Wöhri, *Low Mass Dimuon Production in Proton-Nucleus Collisions at 400 GeV at the CERN-SPS*, PhD Thesis, Technische Universität Wien, 2004.

[WöhLou04] H. K. Wöhri and C. Lourenço, *Heavy Flavour Production Cross-Sections from Fixed Target to Collider Energies*, J. Phys. G: Nucl. Part. Phys. **30** (2004) S315.

[Wyl99] K. Wyllie *et al.*, *A Pixel Readout Chip for tracking at ALICE and Particle Identification at LHCb*, Proceedings of the Fifth Workshop on Electronics for LHC Experiments. Snowmass, Colorado, 1999.